The Influence of Substrate's Elasticity and Thermal Properties on Drop Evaporation

PhD Thesis

M.Sc. Marcus Camarinha Lopes | Matrikelnummer: 1211704
Maschinenbau, Technische Universität Darmstadt

TECHNISCHE UNIVERSITÄT DARMSTADT

The Influence of Substrate's Elasticity and Thermal Properties on Drop Evaporation

"Der Einfluss der Elastizität und der thermischen Eigenschaften des Substrates auf die Tropfenverdunstung"

Vom Fachbereich Maschinenbau
an der Technische Universität Darmstadt
zur
Erlangung des akademischen Grades eines
Doktor-Ingenieurs (Dr.-Ing)
genehmigte
Dissertation
vorgelegt von
M.Sc. Marcus Camarinha Lopes
aus Campinas, Brasilien.

Berichterstatter: Prof. Dr.-Ing. Cameron Tropea
Mitberichterstatter: PD Dr. rer. nat. Elmar Bonaccurso

Center of Smart Interfaces | Experimental Interface Physics
Tag der Einreichung 15. August 2013
Tag der mündlichen Prüfung 19. November 2013, Darmstadt

D17

Erklärung

Hiermit erkläre ich, dass ich die vorliegende Arbeit, abgesehen von den in ihr ausdrücklich genannten Hilfen, selbständig verfasst habe.

Darmstadt, den 15. August 2013

Abstract

This work contributes to expand the scientific knowledge on sessile drop evaporation by presenting experimental investigations on the influence of substrate's elasticity, thermal conductivity, thermal diffusivity and wettability on the evaporation of a sessile drop.

Performed experimental investigations show that soft substrates (Young's modulus below 10 MPa) are able to directly influence the dynamics of the triple-phase-contact-line (TPCL) of a sessile drop by influencing its receding contact angle. A model to predict the change of the receding contact angle in dependence of the Young's modulus and maximal deformation height of the substrate was developed and reproduced experimental values very well. The influence on the receding contact angle has consequences for the evaporation mode of the drop. Softer substrates delay the transition from constant contact radius (CCR) to constant contact angle (CCA) evaporation mode. Because evaporation rate of a drop during the CCR mode is higher than during CCA mode, evaporation is faster on softer substrates. By fine-tuning the Young's modulus of a polydimethylsiloxane elastomer (PDMS), the control of evaporation mode and, consequently, evaporation time was demonstrated.

In this work, investigation on particle deposition during the evaporation of water-silica suspension drops showed that the TPCL velocity increases with decreasing Young's modulus of the substrate. A model for the contact line velocity considering capillary forces, viscoelastic dissipation, and contact line friction was developed and reinforced experimental findings. With increasing TPCL velocity, the thickness of the liquid film (Landau-Levich film) trailing behind the drop rim increases. Particles smaller than this film were more likely to be deposited. Particles larger than the thickness of the film moved together with the contact line and were accumulated until the contact line was pinned. Particle accumulation at the TPCL is thus a result not only of the evaporation driven flow, like described in previous work, but also of the movement of the TPCL. Fine-tuning of Young's modulus of PDMS substrates allowed the control of particle deposition without having to necessarily modify the used suspension.

Thermal conductivity controlled the evaporation rate by affecting the temperature underneath the drop. Substrates with higher thermal conductivity have higher temperatures underneath the drop because enough heat could be transported to the cooling drop. For substrates with low thermal diffusivity the temperature decreases steadily during the course of evaporation. Consequently, differently than mostly assumed, thermal properties need to be considered for a precise prediction of evaporation rate and time.

Table of Contents

List of Symbols

Roman Symbols

a	Contact radius [m]
a'	Normalized contact radius (with respect to initial contact radius) [1]
c	Vapor concentration [kg/m^3]
C_x	Capacitance factor[1]
Ca	Capillary number [1]
d_p	Particle diameter [m]
D	Diffusion coefficient [m^2/s]
D_p	Particle diffusivity in liquid [m^2/s]
e	Thermal effusivity [W·s$^{0.5}$/m^2·K]
E	Young's modulus [Pa]
F	Stress at the contact line [N/m]
f_i	External volume force [N/m^3]
g	Gravitational acceleration [m/s^2]
G	Shear modulus [Pa]
h	Drop height [m]
h_{lv}	Evaporation enthalpy [J/kg]
h_{rim}	Deformation height at rim [m]
h_∞	Landau-Levich film thickness [m]
j_m	Evaporation flux [kg/(s·m^2)]
k	Thermal conductivity [W/m·K]
K	Curvature of interface [1/m]
L	Distance between particles [m]
M	Molar mass [kg/mol]
$\dot{m}$	Change of mass - Evaporation rate [kg/s]

Ma	Marangoni-number [1]
$\mathbf{n}$	Normal vector to liquid-gas phase [1]
P^V	Vapor pressure [Pa]
r	Radial coordinate [m]
R	Gas constant [J/(K·mol)]
RH	Relative vapor pressure [1]
s_i	Displacement field [m]
T	Temperature [K]
t	Time [s]
t_{evap}	Evaporation time [s]
t_l	Length of surface tension action [m]
u	Velocity [m/s]
U	Contact line velocity [m/s]
u_c	Transition velocity [m/s]
V	Volume [m^3]
$\dot{V}$	Volume evaporation rate [m^3/s]
$\dot{W}_{\mathrm{cap}}$	Capillary work rate [W]
$\dot{W}_{\mathrm{CL}}$	Contact line friction dissipation [W]
$\dot{W}_{\mathrm{def}}$	Deformation work rate [W]
z	Vertical coordinate [m]
z_d	Substrate displacement [m]

Greek Symbols

α	Thermal diffusivity [m^2/s]
γ	Surface tension [N/m]
γ_l	Surface tension of the liquid-gas interface [N/m]

γ_s	Surface energy of the solid-gas interface [N/m]
γ_{sl}	Surface energy of the solid-liquid interface [N/m]
γ^p	Polar contribution of the surface energy [N/m]
γ^d	Dispersive contribution of the surface energy [N/m]
δ_{ij}	Kronecker delta [1]
Δ	Work rate dissipation constant [1]
ΔT_{Drop}	Temperature difference between top and edge of a drop [K]
$\Delta\theta$	Contact angle hysteresis [°]
ΔP_{L}	Laplace pressure [Pa]
ΔP	Pressure difference [Pa]
$\varepsilon_{\mathrm{defor}}$	Deformation energy [J/m]
ε_{ij}	Deformation field [1]
η	Dynamic viscosity [Pa·s]
θ	Contact angle [°]
θ_{a}	Advancing contact angle [°]
θ_{r}	Receding contact angle [°]
λ	Capillary length [1]
μ_{f}	Friction parameter [Pa·s]
ν	Poisson's ratio [1]
ξ	Distance within the largest amount of deformation energy is stored [m]
ρ	Density [kg/m^3]
σ_{ij}	Stress field [N/m^2]

List of Abbreviations

AFM	Atomic force microscope

CCA	Constant contact angle
CCR	Constant contact radius
CCD	Charge-coupled device
DNA	Deoxyribonucleic acid
FEM	Finite element method
HPLC	High-performance liquid chromatography
PDE	Partial differential equation
PDMS	Polydimethylsiloxane
PIV	Particle image velocimetry
PMMA	Poly(methyl methacrylate)
RMS	Root mean square
THF	Tetrahydrofuran
TPCL	Triple-phase-contact-line
TU	Technische Universität

1 Introduction and Motivation

Drop evaporation is a fundamental process in nature and of great interest for many technical applications. Modern science on drop evaporation can be dated back to the beginning of the 20th century, when scientists like Morse and Langmuir started investigations on evaporation.[1, 2] Since then, the research topic drop evaporation has developed and different technical applications are now based on (or depend directly from) the drop evaporation process, like crop spraying[3], spray cooling[4], combustion[5], measurement of diffusion coefficients in polymer films[6], or inkjet-printing.[7] In other words, drop evaporation is related to the food people eat, the energy people use, and the information people read in newspapers and on product packages.

The evaporation of pure liquid drops on rigid and inert surfaces has been deeply investigated and, since the work of Picknett and Bexon[8], well understood. The interest in scientific investigations of drop evaporation and particle deposition during evaporation has increased much in the last years following a trending topic set by the publication of Deegan et al. on the so called “coffee-stain” effect, which explains the higher concentration of particles at the rim compared to the middle of a stain left on a surface after evaporation of a drop of coffee. From this everyday observation the effect got its name (the coffee-stain effect is discussed in detail in section 2.3.2).[9] Recent scientific works on drop evaporation investigated the non-equilibrium effects[10], evaporation of solvents on soluble substrates[11], the reversal of the Marangoni flow[12], evaporation flux on an evaporating drop[13, 14], evaporation of mixtures[15, 16], and other phenomena (analytical solution for the evaporation rate, drop evaporation on superhydrophobic surfaces, heated surfaces, and evaporative cooling).[17-21] But, although knowledge advanced considerably in the last century, fundamental understanding of the influence of soft deformable substrates (substrates with low elasticity, i.e. Young’s modulus below 10 MPa) as well as substrates with controllable thermal properties and wettability on the drop evaporation is still lacking. The presented work aims to contribute to fill this gap in this research field.

The investigation of drop evaporation on soft substrates, substrates with controllable thermal properties or wettability, which is presented in this thesis, is not only of interest for the fundamental-science, but has also major relevance for several technical applications such as microfluidics, printed electronics, and ink-jet-printing.[22]

An example of an emerging technology, which shows the importance to understand the evaporation on soft substrates, is the so called “lab-on-a-chip”. The concept of the lab-on-a-chip technology is based on the idea of miniaturizing a laboratory down to the size of an electronic chip (microfluidics), so that such devices become portable and disease diagnostics can be performed faster and independently of a regular laboratory.[23] Such devices need a single sample drop to perform the analysis, and evaporation for such small initial volumes cannot be neglected. Because soft polymers (due to their casting properties) are widely employed for the production of microfluidic devices, it is necessary to better understand the role of such soft substrates on the evaporation. The recent findings in literature about the deformation of the substrate in the order of a few micrometers by a sessile drop are a good starting point for further research on the evaporation of drops on soft substrates.[24, 25]

Exemplary applications where particle deposition occurs during drop evaporation and may be influenced by the substrate are: inkjet-printing[7], 3D inkjet-printing[26-28], DNA analysis using microarrays[29, 30], evaporation induced self-assembly[31], industrial mass production (printed electronics[32] and Rapid Prototyping[33]). Here, deposited suspension drops (containing ink, pigment, or marked DNA) will evaporate on substrates leaving the non-volatile particles on the substrate. The formation of controllable and reproducible patterns during drop evaporation is very important for such applications as printing quality depends strongly on the homogeneity and size of the patterns deposited. Understanding how substrate elasticity can influence the deposition process during drop evaporation may allow the control of deposit formation.

Interesting aspects related to this work can be found even in simple daily tasks at home. Many people have already wondered: “Why not all the dishes come out dry at the end of a washing cycle?” Frequently, plastic dishes remain wet while ceramic or metal dishes are completely dry. In most of the cases, the plastic surfaces are not wetted by a uniform water film, but by sparse drops. Because thermal properties control the heat transport between drop and substrate, and wettability could be related to the liquid load on dishes, the investigation of drop evaporation on substrates with different thermal properties or wettability could even answer this question asked in a household.[34-38]

The open questions in fundamental research:

- How does substrate’s elasticity (Young’s modulus) influence drop evaporation?
- How can pattern formation during evaporation be influenced by substrate’s elasticity?

- What is the role of substrate's thermal properties on drop evaporation? Does substrate wettability influence the liquid load on a surface?

as well as the technical applications related to drop evaporation were the motivation to carry out this research on drop evaporation on substrates with different elasticity and thermal properties.

1.1 Goals of the Presented Work

The further development of several technical applications, which are either already established or emerging, depends on the fundamental understanding of the drop evaporation process on substrates with different elasticity and thermal properties. The goals of this work are:

- Design and perform evaporation experiments using pure liquid drops on substrates with different elasticity but similar wettability. Investigate the influence of substrate elasticity (Young's modulus) on drop evaporation in order to answer the question: How does substrate's elasticity influences drop evaporation?
- Investigate experimentally the deposition process of suspended particles during the evaporation of a sessile drop. Design and perform experiments to understand how the substrate's elasticity influences this process.
- Design and perform an experimental investigation on the influence of the substrate's thermal properties on the drop evaporation process.

1.2 Outline

Chapter 2 presents the fundamentals of wetting and drop evaporation. It introduces the different evaporation modes and contact angles, which are used to describe liquid-solid wetting and dynamic processes at the triple-phase-contact-line (TPCL), where liquid, solid and vapor phase meet. Moreover, chapter 2 introduces the reader to different phenomena that take place simultaneously during sessile drop evaporation.

The applied experimental and numerical methods are introduced in chapter 3. Set-ups used to measure the evaporation process, contact angle dynamics, and liquid load are explained in detail. In this chapter substrate sample preparation methods are described in detail as well.

Chapter 4 presents the investigation about the influence of soft substrates on the process of drop evaporation. This study is divided into: the development of an analytical description of the evaporation time in dependency of the receding contact angle of a substrate (section 4.1) and the experimental results and analysis in sections 4.2 and 4.3.

Chapter 5 is about the control of deposition pattern using soft substrates. The first section of this chapter demonstrates how contact line velocity can be predicted on soft substrates

(section 5.1). The following sections describe the experimental findings and discuss the influence of soft substrates on the deposition pattern from evaporating water-silica suspension drops.

Chapter 6 describes the experimental investigation of the influence of thermal properties (thermal conductivity and diffusivity) and surface wettability of a substrate on an evaporating sessile drop. Experiments are presented in section 6.1. Experiments are compared with numerical simulations performed by collaborators (section 6.2). The influence of substrate's wettability on the liquid load of a sprayed surface is commented in section 6.3. For sake of reader's comprehension the numerical model developed by collaborators is shortly described in the numerical methods section 3.8.2.

A summary of this thesis is presented with conclusions and outlook in chapter 7.

2 Fundamentals and State-of-the-Art

In this chapter, the general principles of wetting will be introduced, especially with regard to the definition of the different contact angles used in literature. It will be explained how wettability is influenced by surface properties. Then, the basic knowledge and the state-of-the-art of drop evaporation as well as the processes occurring during evaporation (internal flow, coffee-stain effect, and deformation of the substrate) will be recapitulated.

2.1 Wetting

Whenever a liquid contacts a solid, new interface is created and wetting occurs. Generally, this contact occurs in the presence of a third medium (usually a gas). Upon contact, intermolecular forces inside every phase and between the phases will drive the created interface to equilibrium by decreasing its free energy, also called Gibbs energy.

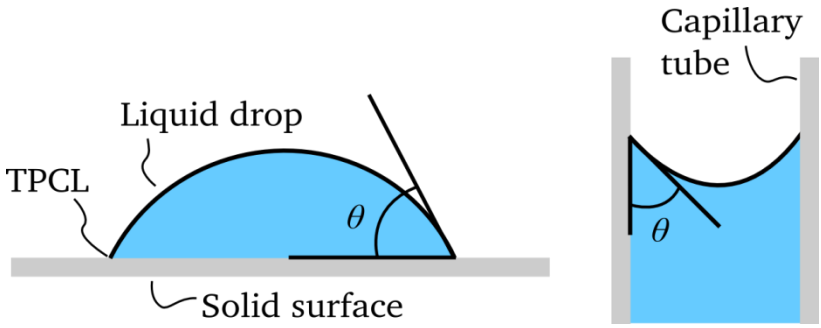

Figure 2-1: Liquid wetting a solid surface and graphical representation of the contact angle for a sessile drop and liquid inside a capillary tube.

One of the most used properties to characterize wetting is the contact angle (θ), which is defined as the angle between liquid-solid and liquid-gas interfaces at the triple-phase-contact-line (TPCL) shown in Figure 2-1.[39] The study of the contact angle can be traced back to Thomas Young, who stated one of the best known equations in wetting science[40]:

$$\cos(\theta) = \frac{\gamma_s - \gamma_{sl}}{\gamma_l} \tag{2.1}$$

Here, γ_s and γ_l are respectively the surface tensions of the solid and liquid, and γ_{sl} is the interfacial tension of the liquid-solid interface. Equation (2.1) is now known as Young's equation and is used extensively due to the simplicity of measuring the contact angle of a

sessile drop on a solid surface. In order to determine the surface tension of the solid γ_s, it is necessary to know the other three parameters (θ, γ_l and γ_{sl}). Surface tension of the liquid γ_l and contact angle θ can be measured accurately using a tensiometer and a goniometer. In contrast to this, the interfacial tension γ_{sl} is not directly accessible and poses a problem for the calculation of the surface tension of the solid. This can be solved by formulating another equation for γ_{sl} in dependency of the individual surface tensions (γ_s and γ_l), and assuming the surface tension is the addition of dispersive (van der Waals) and of polar contributuions ($\gamma = \gamma^d + \gamma^p$) :

$$\gamma_{sl} = \gamma_s + \gamma_l - 2\phi\sqrt{\gamma_l\gamma_s} \tag{2.2}$$

$$\phi = \frac{\sqrt{\gamma_l^d\gamma_s^d} + \sqrt{\gamma_l^p\gamma_s^p}}{\sqrt{\gamma_l\gamma_s}} \tag{2.3}$$

Estimates show that ϕ is between 0.5 and 0.2. This formulation leads to a soluble system of equations to calculate γ_{sl}.[39]

In the case of an ideal surface, Young's equation yields the so called Young's or "equilibrium" contact angle when the Gibbs energy reaches its minimum. Thermodynamically, equilibrium is achieved at constant pressure and temperature at this minimum of Gibbs energy. For real surfaces however, it is nearly impossible to measure directly the "equilibrium" contact angle, as the contact angle can be influenced by geometrical and chemical heterogeneities.

Contact angles acquired by goniometric measurements, including all measured contact angles in this work, are "apparent" contact angles. The "apparent" contact angle is defined as the angle between the projection of the solid surface (as observed macroscopically) to the liquid-gas interface (left part of Figure 2-2).[39] The "microscopic" contact angle is the actual contact angle with the surface, as shown in the right part of Figure 2-2. The contact angle of a specific liquid-solid-gas system can be influenced by surfactants or electric charges, as this will create an unbalance of the forces acting on the TPCL.

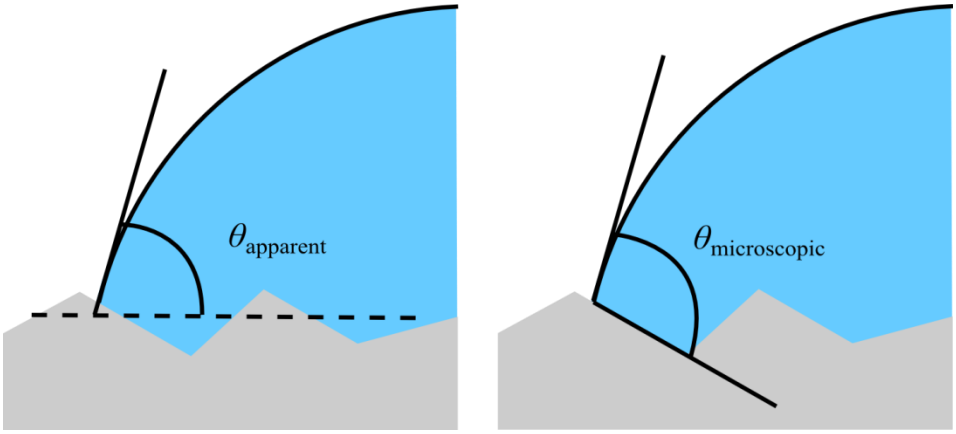

Figure 2-2: Graphical representation of “apparent” and “microscopic” contact angles.

Actual focus of the wetting research, among other topics, are the dynamic wetting[41], experimental mesoscopic (length-scale between micro and macroscopic) contact angle[42], and the simulation of the microscopic contact angle by means of molecular dynamics.[43]

2.1.1 High-energy and Low-energy surfaces

Surfaces can be classified with respect to their surface energy. Materials which have covalent, ionic or metallic bonds have high-energy surfaces (γ_s ranges from 0.5 N/m up to 5 N/m). Materials which are held together by van der Waals forces or hydrogen bonds are called and have low-energy surfaces (γ_s around 0.05 N/m).[44] Most liquids wet high-energy surfaces completely, i.e. the contact angle equals zero ($\theta = 0°$). Low-energy surfaces, on the other hand, give rise to partial $0° < \theta < 180°$ or complete wetting, in dependency of the surface tension of the liquid.

When a small quantity of liquid completely wets a surface, the liquid will spread until a thin film has covered the entire surface or the liquid has evaporated. For the case of partial wetting, the liquid will form a finite contact angle and the liquid will take the shape of a spherical cap or of a pancake. The shape of the liquid lens will depend on its radius a and the capillary length λ. The capillary length is defined as $\lambda = \sqrt{\gamma_l/\rho g}$ with γ_l the surface tension of the liquid, ρ the density of the liquid, and g the gravitational acceleration. If the radius of the drop is smaller than the capillary length, gravity can be neglected and the drop will be a spherical cap. Water, for example, has a capillary length of around 2 mm at ambient temperature and pressure.

2.1.2 Contact Angle Hysteresis

It has been already mentioned in the beginning of section 2.1 that the contact angle of a surface can be influenced by heterogeneities. Due to surface heterogeneities a sessile liquid drop can assume a broad range of contact angles, for which the interfacial tensions are in balance. The drop attains a stable geometry and its contact line does not move – it is "pinned". The range of stable contact angles is called "contact angle hysteresis" and may be a few degrees (< 5°) even for very flat and homogenous surfaces. The highest possible contact angle observed, while the contact line is pinned, is called the "advancing contact angle" θ_a. The lowest is called "receding contact angle" θ_r.[39]

The measurement of advancing and receding contact angles relies on the measurement of the contact angle as the TPCL is on the verge of moving. Figure 2-3 shows in a simple scheme, how the measured contact angle changes with contact line velocity (left part of figure) and how the contact radius depends on the contact angle (right part of the figure). For the measurements of such curves it is possible either to move the TPCL in a spontaneous matter, like for example during evaporation or condensation of the drop, or by forcing the movement of the TPCL, e.g. by adding more liquid to the drop or by applying external forces to the drop.

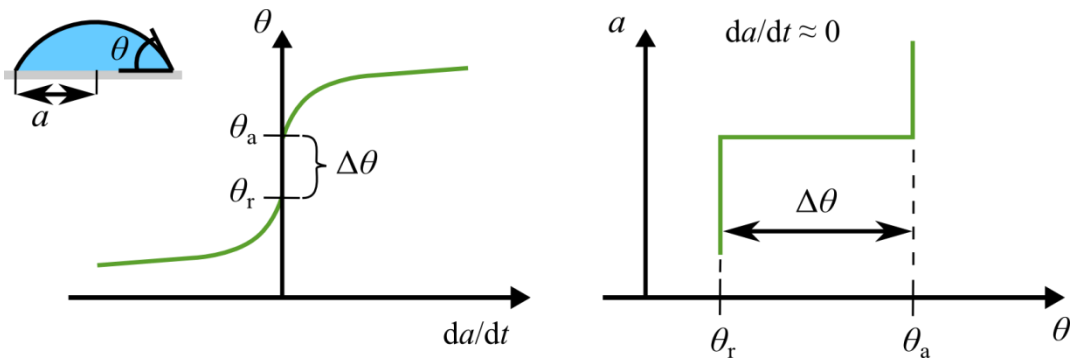

Figure 2-3: Left: Contact angle of surfaces in dependence of the contact line velocity. Right: Mapping of drop geometry for a slow moving contact line. Advancing, receding contact angles and the contact angle hysteresis are indicated respectively by θ_a, θ_r and $\Delta\theta$.

In general, the contact angle hysteresis is proportional to the number of heterogeneities.[45] However, geometrical roughness may lead to decrease of the contact angle hysteresis if air can be entrapped between solid and liquid.[45]

Advancing and receding contact angles are helpful to characterize a surface. In contrast to the "equilibrium" contact angle, advancing and receding contact angles give information about

specific interfacial force balances for which the contact line moves, making the advancing and receding contact angles also more relevant to technical applications like coating, water-repellent clothing and microfluidics, to which the movement of the drops is crucial.

2.2 Drop Evaporation

Evaporation occurs when a material changes from the liquid phase to the gas phase. The driving potential of evaporation is the vapor pressure difference between liquid and gas phase. This potential depends on parameters like temperature, surface tension and curvature of the interface. In this work the evaporating drops are below boiling temperature (unheated substrate) and are always in the presence of air, i.e. in a so called two-component (vapor of the liquid and air) system.

For the evaporation in a one-component system, where the gas phase is the vapor of the evaporating liquid, the total pressure homogenization in the gas phase is fast and molecule concentrations are given by the gas law. When drops evaporate in the presence of the gas phase made of a second medium, e.g. air, the gas phase is a mixture. Here, the mechanical balance, i.e. balance of total pressure, is achieved rapidly, but the balance of the liquid vapor concentration in the gas is driven by a limiting process: the vapor diffusion in the gas.[46] In general, this limiting process is one of the main assumptions for drop evaporation models. Other relevant assumptions are the quasi-stationary diffusion process and the homogenous temperature distribution in the substrate.

The quantitative investigation of drop evaporation started already one century ago. Morse experimentally investigated the evaporation of solid iodine spheres.[1] It was the first experimental report which showed that the evaporation rate of a sphere is proportional to its radius and not to its surface. By using an analogy between mass flux and electrostatic potential, Maxwell obtained an equation, later named after him, to describe the evaporation (change of mass in time, $\dot{m}$) of a sphere in an infinite medium, which was later extended to describe the evaporation rate of a body of any shape by Picknett and Bexon:[8]

$$\dot{m} = -4\pi \cdot D \cdot C_x(c_0 - c_i) \tag{2.4}$$

where D is the diffusion coefficient of vapor in air, c_0 and c_i are, respectively, the concentrations of vapor close to the sphere and far from the sphere, and C_x is the electrostatic capacitance factor of the isolated body.[8] By using this model to describe the evaporation of sessile drops, Picknett and Bexon were able to determine the evaporation rate of a sessile drop

by calculating the respective capacitance factor of the equiconvex lens formed by mirroring the sessile drop on the surface. In dependence of the experimental boundary conditions, the equation for the evaporation rate of a sessile drop can assume different forms based on the equation:[47]

$$\dot{m} = -4\pi \cdot a^2 \cdot D \frac{dc}{dr} \tag{2.5}$$

Where c is the vapor concentration and r is the radial coordinate. Assuming that the vapor can be described by the ideal gas law:

$$c = \frac{M \cdot P^V}{R \cdot T} \tag{2.6}$$

where M is the molecular weight, P^V is the vapor pressure of the evaporating liquid, R is the gas constant and T is the temperature in Kelvin,[47] then equation (2.5) can also be elaborated to:

$$\dot{m} = -4\pi \cdot a \cdot D \left(\frac{M \cdot P^V}{R \cdot T}\right) \cdot (1 - RH) \tag{2.7}$$

here RH is the relative vapor pressure in the environment. This equation can describe the momentary evaporation rate of a sessile drop. Although slight different equations can be found in literature, e.g. Sefiane et al.[48] and Eggers et al. [14], their results are similar.

2.2.1 Evaporation Modes – CCR and CCA

Picknett and Bexon described two ideal sessile drop evaporation modes: the constant contact radius (CCR) and the constant contact angle (CCA) mode.[8] In the CCR mode the contact radius a remains constant with time, while in the CCA mode the contact angle θ remains constant (Figure 2-4).

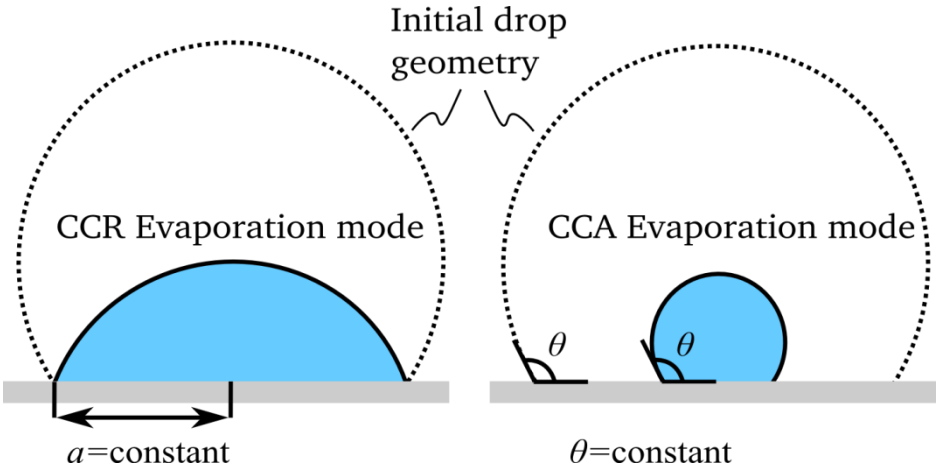

Figure 2-4: Scheme of a sessile drop evaporating in two ideal evaporation modes: Left – constant contact radius (CCR) mode. Right – constant contact angle (CCA) mode.

After the deposition on a solid surface, drops usually start evaporating in the CCR mode. They later switch to the CCA mode, when the receding contact angle (θ_r) is reached. At this point the contact radius starts to decrease and the TPCL moves towards the center of the drop.[49] A mixed mode between CCR and CCA can also observed, especially towards the end of evaporation as TPCL dynamics start to play a role, and is attributed to physical and chemical surface heterogeneities, which have then a similar length scale as the drop.[47]

2.2.2 Evaporation Rate

The mass reduction, or evaporation rate, of a sessile drop with time is a main parameter in evaporation studies. Over the past decades, many models were developed to describe the evaporation rate of a sessile drop.[13, 14, 50, 51] All models work more or less well in specific experimental conditions, but a generic model still missing. The work by Erbil gives an overview on this topic.[47] For clarity, some selected models will be presented here.

Constant Contact Radius (CCR) Evaporation Mode

The CCR evaporation mode occurs when the contact line remains pinned. This is, e.g., the case when a drop evaporates on a high-energy surface. Previous experimental and theoretical works[1, 8, 51] have already shown that the volume of a drop decreases linearly with time:

$$V^{CCR}(t) = V_0\left(1 - \frac{t}{t_{evap}^{CCR}}\right) \tag{2.8}$$

V_0 is the initial volume, t is the time and t_{evap}^{CCR} is the evaporation time for a drop evaporating in CCR mode. Assuming diffusion limited and isothermal evaporation (constant temperature in the substrate), the volume of a drop evaporating in the CCR mode can be written as:[51]

$$V^{CCR}(t) = V_0 - 2\pi D\Delta P\,\frac{a \cdot M}{\rho \cdot R \cdot T} \cdot \frac{f(\theta_0/1.6)}{\sin(\theta_0/1.6)} \cdot t \tag{2.9}$$

Here, θ_0 is the initial contact angle and ΔP the vapor pressure difference between the saturated vapor pressure and the ambient vapor pressure far away from the drop. In this case the evaporation time takes the form:

$$t_{evap}^{CCR} = V_0\,\frac{\rho \cdot R \cdot T}{2\pi \cdot a \cdot DM(\Delta P)} \cdot \frac{\sin(\theta_0/1.6)}{f(\theta_0/1.6)} \tag{2.10}$$

The relative error between this model and acquired experimental data was found to be less than 1.5 % for initial contact angles up to 90°.[51]

Constant Contact Angle (CCA) Evaporation Mode

The CCA evaporation mode is typical for low-energy surfaces. When the receding contact angle is reached the TPCL starts to move towards the center of the drop. The volume of a drop evaporating in the CCA mode decreases according to a power law with exponent 3/2:[10, 17]

$$V^{CCA}(t) = V_0\left(1 - \frac{t}{t_{evap}^{CCA}}\right)^{\frac{3}{2}} \tag{2.11}$$

V_0 is the initial volume, t is the time and t_{evap}^{CCR} is the evaporation time for a drop evaporating in CCA mode. Picknett and Bexon derived an equation to describe the volume with time:

$$V^{CCA}(t)^{2/3} = {V_0}^{2/3} - \frac{4}{3}\pi D\frac{M\Delta P}{\rho RT}\left(\frac{3}{\pi}\right)^{1/3} \cdot \frac{f(\theta)}{\beta^{1/3}} \cdot t \tag{2.12}$$

With $\beta = (1 - \cos\theta)^2(2 + \cos\theta)$ and $f(\theta) = 0.00008957 + 0.633\theta + 0.116\theta^2 - 0.08878\theta^3 + 0.01033\theta^4$. The respective evaporation time can be written as:

$$t_{evap}^{CCA} = \frac{3(V_0^2\beta)^{1/3}}{4f}\,\frac{\rho RT}{M\Delta P\pi}\left(\frac{\pi}{3}\right)^{1/3} \tag{2.13}$$

2.2.3 Evaporation Flux

Under the assumption that diffusion is driving the evaporation, the geometry of an evaporating drop influences the evaporation flux j_m, which is the mass flow per surface area from the liquid to the vapor. The lower the contact angle of a drop is, the stronger will be the evaporation flux at the contact line, similar to the heat flux observed during the cooling of a flat hot plate immersed in a cold liquid. Evaporation flux models have been formulated in different works[14, 34, 46] and all these formulations can reproduce the dependency of the evaporation flux on the contact angle of a drop.

From the theoretical point of view, one singularity is associated with the evaporation flux at the TPCL:[52] when using the diffusion equation to describe the evaporation flux of a sessile drop the concentration gradient at the TPCL becomes very high causing a singularity to the evaporation flux. A method to overcome this singularity is by considering more complex surface-liquid interactions like the disjoining pressure.[52]

In general, models for the evaporation flux are empirical and rely on fitting parameters, like in the model of Ristenpart et al. where the evaporation flux in dependence of the radius $j_m(r)$ for contact angles smaller than 90° is given by:[34]

$$j_m(r) = j_0(\theta)\left[1 - \left(\frac{r}{a}\right)^2\right]^{-\frac{1}{2}+\frac{\theta}{\pi}} \tag{2.14}$$

with

$$j_0(\theta) = j_0(\pi/2)(0.27\theta^2 + 1.3)(1 - \Lambda) \tag{2.15}$$

r is the radial coordinate from the center of the drop, $j_0(\pi/2) = \frac{D}{R}(1 - RH)c_{sat}$, and $\Lambda = 0.2239(\theta - \pi/4)^2 - 0.3619$. c_{sat} is the saturated vapor concentration. A relative error of less than 5 % for the valid spectrum of contact angle was found by comparing numerical calculations (based on finite element methods assuming diffusion driven evaporation) to the analytical solution provided by equation (2.14), such small deviation makes equation (2.14) a fast and reliable method to predict the evaporation flux of a drop.

Depending if the drop evaporates in CCR or CCA mode, the evaporation flux can induce a convective flow internal to the drop in order to sustain mass conservation. This and other phenomena occurring during drop evaporation are explained in the following section 2.3.

2.3 Phenomena Occurring During Drop Evaporation

Processes that can arise during the evaporation of drops are: induction of internal flow, deposition of solid particles from suspensions, or deformation of the substrate. This section gives a short introduction about these processes and a general overview on the state-of-the-art of evaporation-driven processes.

2.3.1 Flow Inside the Drop

The flow inside a drop can be driven either by evaporation, as the evaporation flux drives the liquid to flow towards the contact line to fulfill mass conservation, or by Marangoni convection (flow), induced by surface tension gradient at the liquid-gas interface.

The internal flow is driven by the inhomogeneous evaporation flux which is higher at the TPCL and leads to an enhanced mass transport from the drop to the gas-phase. If the contact line of the drop is pinned, the liquid must be replenished in order to compensate for the mass loss at the TPCL, and therefore a flow of liquid will be radially directed towards the TPCL. Figure 2-5 shows schematically the velocity field u which is sustained by the evaporation flux j_m.

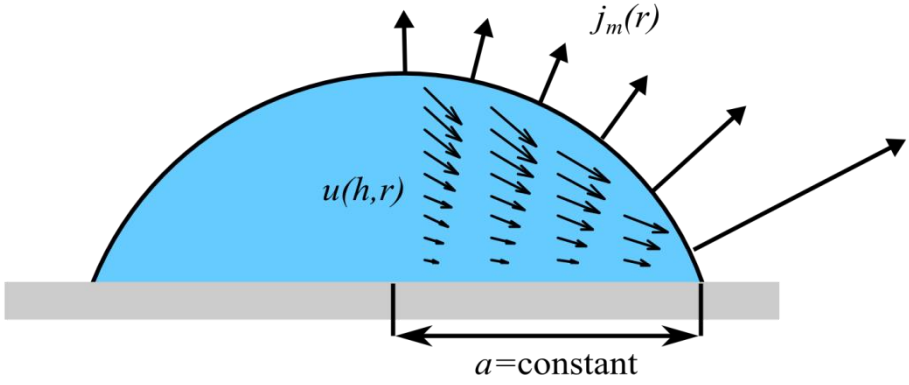

Figure 2-5: Scheme of the induced flow inside a sessile drop due to evaporation flux inhomogeneity.

Hu et al. solved continuity and Stokes equations for an evaporating drop by assuming a diffusion driven, isothermal, and CCR evaporation process, with no shear stresses on the liquid-air interface. The solution of the Stokes equation is given in the separated radial and axial dimensionless velocity:[53]

$$\tilde{u}_r = \frac{3}{8\tilde{r}(1-\tilde{t})}\left[(1-\tilde{r}^2)-(1-\tilde{r}^2)^{-\lambda(\theta)}\right]\left(\frac{\tilde{z}^2}{\tilde{h}^2}-2\frac{\tilde{z}}{\tilde{h}}\right) \tag{2.16}$$
$$+\left[\frac{\tilde{r}h_0^2\tilde{h}}{R^2}\left(\tilde{J}\lambda(\theta)(1-\tilde{r}^2)^{-\lambda(\theta)-1}+1\right)\left(\frac{\tilde{z}}{\tilde{h}}-\frac{3\tilde{z}^2}{2\tilde{h}^2}\right)\right]$$

And

$$\tilde{u}_z = \frac{3}{4}\frac{1}{1-\tilde{t}}\left[1+\lambda(\theta)(1-\tilde{r}^2)^{-\lambda(\theta)-1}\right]\left(\frac{\tilde{z}^3}{3\tilde{h}^2}-\frac{\tilde{z}^2}{\tilde{h}}\right) \tag{2.17}$$
$$+\frac{3}{2}\frac{1}{1-\tilde{t}}\left[(1-\tilde{r}^2)-(1-\tilde{r}^2)^{-\lambda(\theta)}\right]\left(\frac{\tilde{z}^2}{2\tilde{h}^2}-\frac{\tilde{z}^3}{3\tilde{h}^3}\right)\tilde{h}(0,\tilde{t})$$
$$-\left\{\frac{h_0^2}{R^2}\left(\tilde{J}\lambda(\theta)(1-\tilde{r}^2)^{-\lambda(\theta)-1}+1\right)\left(\tilde{z}^2-\frac{\tilde{z}^3}{\tilde{h}}\right)\right.$$
$$+\frac{\tilde{r}h_0^2}{R^2}\tilde{J}\lambda(\theta)(\lambda(\theta)+1)(1-\tilde{r}^2)^{-\lambda(\theta)-2}\left(\tilde{z}^2-\frac{\tilde{z}^3}{\tilde{h}}\right)$$
$$\left.-\frac{\tilde{r}h_0^2}{R^2}\left(\tilde{J}\lambda(\theta)(1-\tilde{r}^2)^{-\lambda(\theta)-1}+1\right)\left(\frac{\tilde{z}^3}{\tilde{h}^2}\right)\tilde{h}(0,\tilde{t})\right\}$$

using $\lambda(\theta) = 0.5 - \theta/\pi$ and $\tilde{J} = -j_m(0,t)/\rho\dot{h}(0,\tilde{t})$. The evaporation flux j_m is given by equation (2.14), the height of the drop is given by $h = h(r,t) = h(0,t)(1-\tilde{r}^2)$ and the change of the height in time is given by $\dot{h}(0,t) = -h_0/t_{evap}$. Dimensionless numbers are defined as follows:

$$\tilde{u}_r = \frac{u_r t_{evap}}{a};\ \tilde{u}_z = \frac{u_z t_{evap}}{h_0};\ \tilde{t} = \frac{t}{t_{evap}};\tilde{r} = \frac{r}{a};\tilde{z} = \frac{z}{h_0};\ \tilde{h} = \frac{h}{h_0} \tag{2.18}$$

This flow inside the drop is practically present in all evaporating drops with pinned contact line and is important for the prediction of particle deposition during drop evaporation. Figure 2-6 shows the calculated flow field for a water drop with a_0 = 1 mm, θ_0 = 90° and t_{evap} = 180 s using equations (2.16) and (2.17).

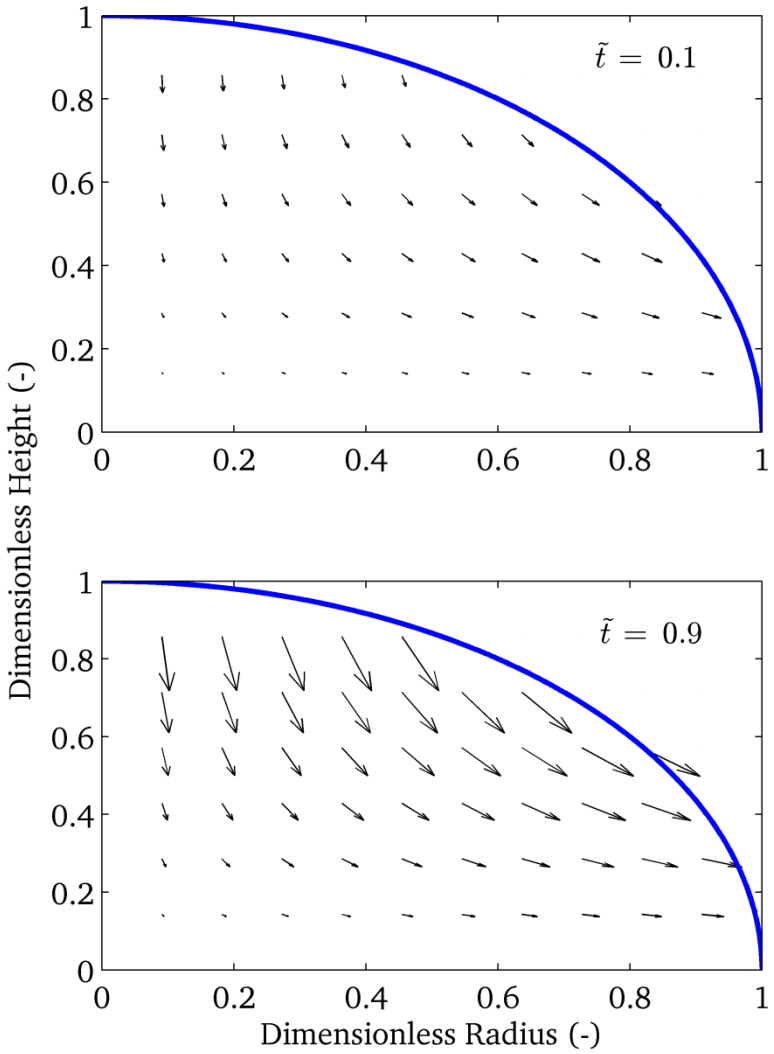

Figure 2-6: Calculated flow field inside a drop due to evaporation using equations (2.16) and (2.17) at different times. Top image $\tilde{t}$=0.1, bottom image $\tilde{t}$=0.9.

Also Marangoni convection can induce a flow inside an evaporating drop. Marangoni convection is the flow driven by a surface tension gradient and is named after Carlo Marangoni.[54] The surface tension of liquids depends on the temperature or, in the case of mixtures, on the concentration of the components. When a temperature or concentration gradient arises along a liquid interface causing a gradient in surface tension, Marangoni convection will take place. A well-known manifestation of Marangoni convection are the so called “tears of wine”. These “tears” can be observed climbing up the wine glass starting from the liquid. This motion is attributed to the surface tension gradient generated by the change of the mixture concentration as alcohol evaporates from the wine, which is mainly a water and ethanol mixture.

Equations (2.16) and (2.17) were extended in a further work from Hu and Larson in order to account for the Marangoni convection (scheme in Figure 2-7).[55] The radial velocity from equation (2.16) has to be extended with following terms to consider Marangoni effects:

$$\tilde{u}_r = \cdots + \frac{Ma\, h_0 \tilde{h}}{2a}\left(K_1 K_2 \tilde{r}^{K_2-1} + 2(1-K_1)\tilde{r}\right)\left(\frac{\tilde{z}}{\tilde{h}} - \frac{3\tilde{z}^2}{2\tilde{h}^2}\right) \tag{2.19}$$

Accordingly axial velocity from equation (2.17) has to be extended with:

$$\begin{aligned}\tilde{u}_z = \cdots &- \frac{Ma\, h_0 \tilde{h}}{4a}\left(K_1 {K_2}^2 \tilde{r}^{K_2-2} + 4(1-K_1)\right)\left(\tilde{z}^2 - \frac{\tilde{z}^3}{\tilde{h}}\right) \\ &+ \frac{Ma\, h_0 \tilde{h}}{2a}\left(K_1 K_2 \tilde{r}^{K_2} + 2(1-K_1){K_2}^2\right)\left(\frac{\tilde{z}^3}{\tilde{h}^2}\right)\tilde{h}(0,\tilde{t})\end{aligned} \tag{2.20}$$

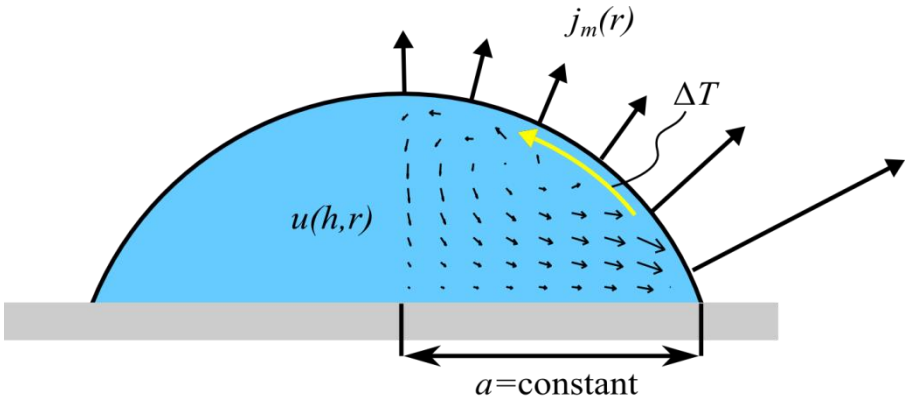

Figure 2-7: Scheme of the induced flow inside a sessile drop due to evaporation flux inhomogeneity and thermal Marangoni convection.

Ma is the dimensionless Marangoni-number given by the ratio between Marangoni force to viscous force, which for thermal driven evaporation can be given by:

$$Ma = -\frac{d\gamma}{dT}\frac{\Delta T_{Drop} t_{evap}}{\eta a} \tag{2.21}$$

Here, η is the dynamic viscosity of the liquid, and ΔT_{Drop} is the temperature difference between the top and edge of the drop. K_1 and K_2 are fitting parameters obtained by matching the computed temperature profile by a phenomenological expression.[55]

Figure 2-8 shows the calculated velocity field using the same parameters as Figure 2-6, but using equations (2.19) and (2.20) at $\tilde{t} = 0.1$ for Ma=+10 and Ma=-10.

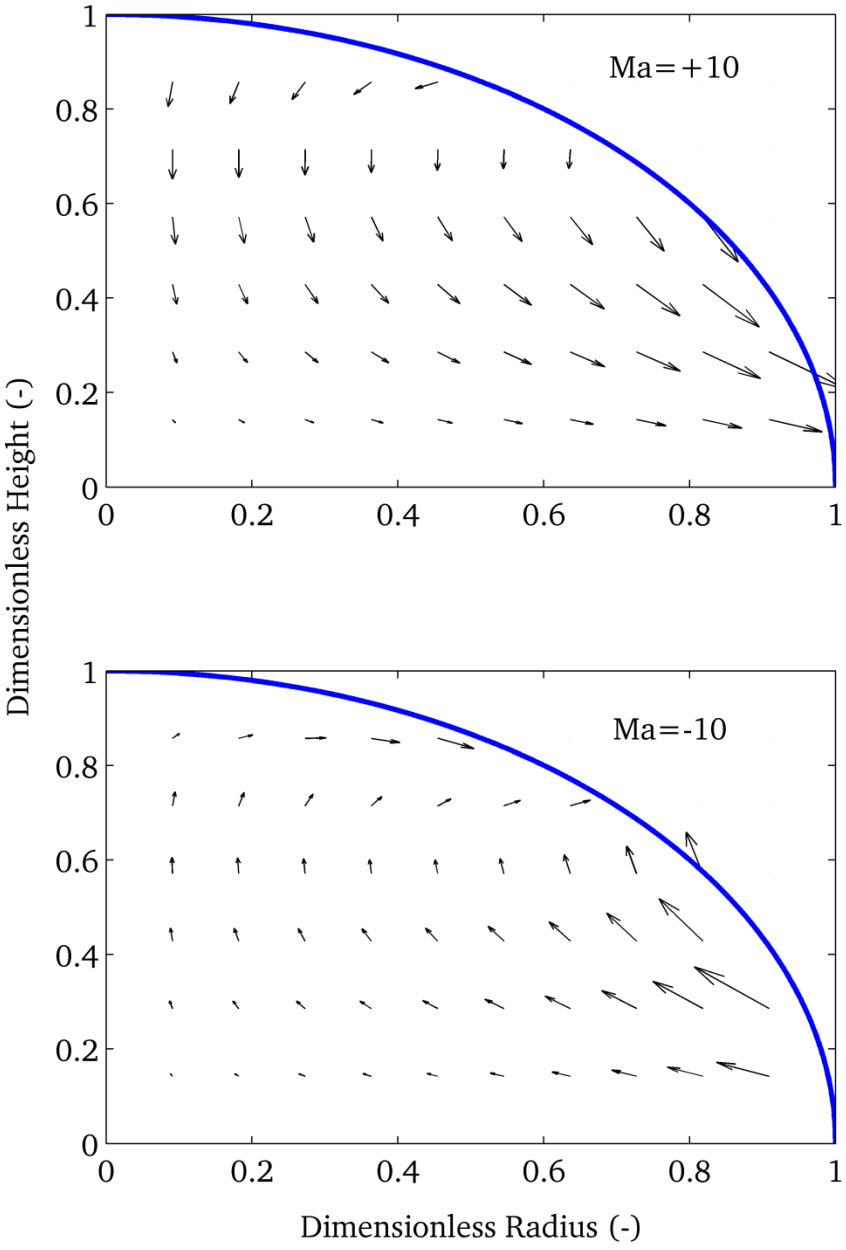

Figure 2-8: Calculated flow field inside a drop considering the evaporation flux and Marangoni convection using equations (2.19) and (2.20) for different Ma numbers. Top image Ma=+10, bottom image Ma=-10.

Although the flow inside the drop is commonly present during evaporation, its measurement cannot be performed with non-intrusive techniques. Measurements of the flow inside evaporating drops are usually performed by particle image velocimetry (PIV),[56] which requires the addition of tracer particles to the liquid. Further challenges faced by the PIV measurement inside drops are related to the small size of an evaporating drop, which requires

microscopic PIV, and to the restricted optical access due to the curved gas-liquid interface of the drop. [57-59]

2.3.2 Coffee-Stain Effect

It is not uncommon to spill a drop coffee on the table when breakfast is being prepared. In the rush to get to work, the drop may be left unnoticed until it has evaporated. What is left on the table is a coffee-stain made of non-volatile components with a peculiar characteristic: the border of the stain is darker than the center (Figure 2-9). The formation of the characteristic shape of the stain (i.e., "coffee-stain effect") is due to the accumulation of particles at the rim of the drop. Accumulation of particles is favored by the internal flow in the drop (see section 2.3.1). The "coffee-stain" effect became very popular with the work by Deegen et al. at the end of the 90's.[9]

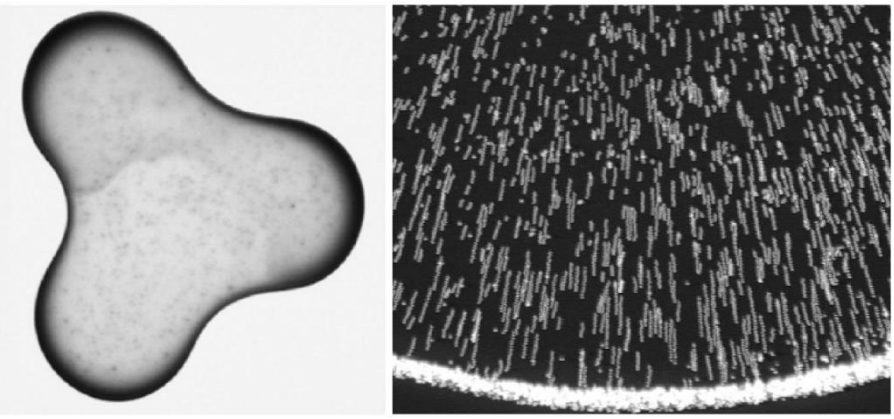

Figure 2-9: Pictures from the work by Deegan et al. showing a three-lobed coffee-stain (left) and a demonstration of the physical process involved in the formation of the stain. The right figure shows superimposed figures (addition of different frames of a movie into one single image) to emphasize the motion of the particles (right).[9]

The coffee-stain effect is of great interest for the self-assembly of nonvolatile solutes like polymers, colloids, and even biological material like DNA.[60] Also for the field of ink-jet printing the coffee-stain effect has a big relevance. Inkjet-printers generate drops of a solvent mixed with a non-volatile solute in order to print books, packaging materials, newspapers, etc. The same ink-jet printing system can also be used to produce DNA microarrays, used for automatic DNA sequencing.[61] In general, these microarrays are printed using a printing system very similar to a normal inkjet-printer, but instead of pigment the drops contain DNA

and fluorescent markers. How this DNA is deposited on the surface is very important for an automated imaging technology used to recognize fluorescence signals. Consequently, controlling the final geometry of the stain left after evaporation represents a big potential not only for fundamental science, but also for different industrial and scientific applications.

With microscopic techniques it is possible to recognize how particles are accumulating at the contact line during the drop evaporation. Marín et al. observed the existence of two different stages of the particle accumulation process at the contact line: ordered and disordered (Figure 2-10). The ordered accumulation of particles is characterized by a packed arrangement of the particles in a crystalline structure, while the non-ordered accumulation leads to a non-crystalline structure.[62] In their work, a critical transition velocity u_c was introduced, above which the ordering of particles switch from ordered to non-ordered arrangement. They showed experimentally evidences of this velocity: $u_c \sim LD_p/d_p^2$, where is L the typical distance between particles, d_p is the particle diameter and D_p is the particle diffusivity in the liquid.

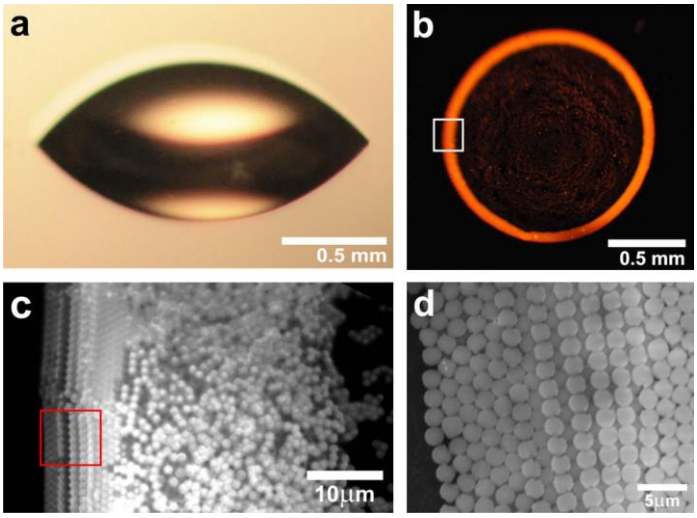

Figure 2-10: Order-disorder transition in the particle stain can be recognized on (c). Images from [62].

In the last decade many works have been published on the control of the coffee-stain effect. Pauchard et al. showed how the high salinity of an evaporation solution will induce cracks on the salt-deposit pattern.[63] Later, Park and Moon were able to use solvent mixtures, giving rise to Marangoni convection (see section 2.3.1), in order to control the coffee-stain effect. The presence of Marangoni convection allowed particles to flow back to the center of the drop during evaporation. This avoided the undesired accumulation of particles at the TPCL.[7]

Experimental investigations on inkjet-printed lines were performed by Soltman and Subramanian. They described the possibility of controlling the coffee-stain effect by controlling the substrates temperature inducing Marangoni convection with a temperature gradient.[64] Other recently studied methods of controlling the particle deposition is using electrowetting[65], anisotropically shaped particles[66], Marangoni-flow-assisted drop drying[67], and surfactants[68]. Surfactants are amphiphilic (containing hydrophilic and hydrophobic groups) and therefore lower the surface tension of a liquid with increasing concentration. During evaporation, a gradient in surfactant concentration is created inducing Marangoni flow (analogue to the thermal driven Marangoni). Electrowetting, Marangoni-flow-assisted drying and surfactants also induce an internal flow, but need respectively additional electronics, vapor control and additives to the liquid. As none of the mentioned methods are completely established, further research is needed in order to find new methods to control particle deposition and better distinguish weaknesses and strengths of each method.

2.3.3 Deformation of the Substrate due to Interfacial Forces

When a liquid drop is sitting on a substrate, interfacial forces between liquid, solid and gas will be balanced. Here, the surface tension of the liquid acts on the substrate. Its absolute value is determined by the liquid surface tension and the direction is given by the contact angle of the liquid on the surface. The horizontal component of this tension will be balanced by the surface energies of the liquid-solid interface and solid-gas interface. On soft substrates, the vertical component of the force must also be taken into account. In fact, the vertical component of the force deforms the substrate underneath the drop.[69, 70] The deformation caused by a macroscopic sessile drop is of the order of nm, and therefore negligible on solid substrates with Young's moduli larger than some hundreds of MPa.[69] But, in the case of a very thin membranes or of soft substrates (like elastomers, gels or biological tissue with Young's modulus below 10 MPa), the deformation of the substrate can be up to micrometers.[69] Figure 2-11 shows a schematic representation of possible deformations of the substrate due to surface tension. This effect is also referred in literature as "elasto-capillary".[71]

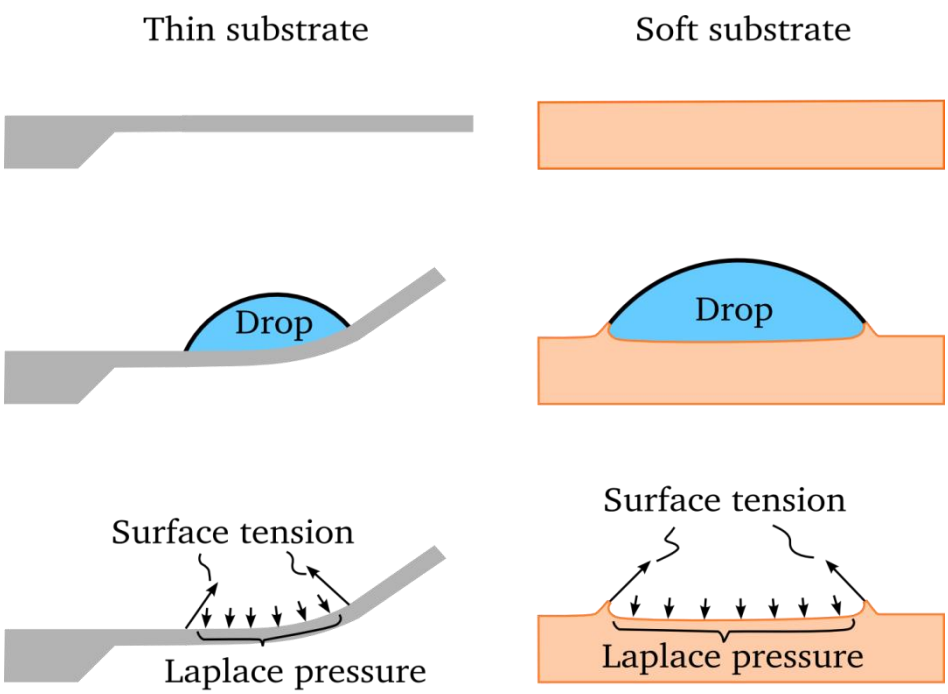

Figure 2-11: Representation of the deformation of a substrate due to surface tension caused by a sessile drop. Left: a sessile drop on a thin substrate, e.g. atomic force microscope cantilever. Right: deformation of a soft substrate, e.g. a soft elastomer.

For materials with a Young's modulus higher than some hundreds of MPa the deformation of the substrate is only relevant if the substrate is thin enough. An example of this kind is shown in the left part of Figure 2-11. The scheme represents a sessile liquid drop on an atomic force microscope (AFM) cantilever, which is made of silicon (E = 150 GPa) and has a thickness in the order of a few micrometers. The idea to measure the deformation caused by a liquid drop allowed to use cantilevers as sensors for monitoring microdrop evaporation.[72] At the bottom left part of Figure 2-11 the representation of the line load acting on the AFM cantilever is shown. The surface tension of the liquid acts upwards and the balancing Laplace (or capillary) pressure acts downward. Laplace pressure is caused by the curvature of the liquid interface of the drop and causes a pressure jump across the interface. Laplace's equation considers the hydrostatic pressure increase upon crossing the interface between two fluids: $\Delta P_{\mathrm{L}} = 2\gamma_l/K$, where K is the curvature of the interface. This pressure jump has relevant consequences also for drop evaporation. For instance, smaller drops will evaporate even in saturated ambient as the pressure inside the drop is increased, increasing also the vapor pressure difference between drop and ambient.[10]

For substrates with a Young's modulus below 10 MPa, deformation of the substrate can be observed independently of their thickness.[69, 70] The right part of Figure 2-11 shows schematically this deformation. The surface tension of the drop acts on the TPCL pulling up a ridge of material. The Laplace pressure acts underneath the drop causing an indentation. The overall deformation looks like a crater. The geometry of such a deformation was described first by Rusanov.[69, 70] His model assumes that the surface tension acts over an interface of thickness t_l, describing the displacement of the substrate $z_d(r)$ analytically for different regions. For the region underneath the drop ($r \leq a$), the deformation is given by:

$$z_d(r) = \frac{4(1-\nu^2)}{\pi E}\left\{\Delta P_\mathrm{L} E\left(\frac{r}{a}\right) + \frac{\gamma \sin\theta}{t_l}\left[aE\left(\frac{r}{a}\right) - (a+t_l)E\left(\frac{r}{a+t_l}\right)\right] + \frac{\pi(1-2\nu)}{4(1-\nu)}\gamma(\cos\theta - \cos\theta_0)\right\} \tag{2.22}$$

For the region where the surface tension acts ($a < r \leq a + t_l$), the deformation is given by:

$$z_d(r) = \frac{4(1-\nu^2)}{\pi E}\left\{\Delta P_\mathrm{L} G^e\left(\frac{a}{r}\right) + \frac{\gamma \sin\theta}{t_l}\left[rG^e\left(\frac{a}{r}\right) - (a+t_l)E\left(\frac{r}{a+t_l}\right)\right] + \frac{\pi(1-2\nu)}{4(1-\nu)}\gamma(\cos\theta - \cos\theta_0)(a+t_l-r)\right\} \tag{2.23}$$

And for $r > a + t_l$:

$$z_d(r) = \frac{4(1-\nu^2)}{\pi E}\left\{\Delta P_\mathrm{L} G^e\left(\frac{a}{r}\right) + \frac{\gamma \sin\theta}{t_l} r\left[G^e\left(\frac{a}{r}\right) - G^e\left(\frac{a+t_l}{r}\right)\right]\right\} \tag{2.24}$$

Here ν is the Poisson's ratio of the substrate, ΔP_L is the Laplace pressure, $G^e \equiv E(i) - (1 - i^2)K(i)$, and $E(i)$ and $K(i)$ are respectively the total normal elliptical Legendre integrals of the first and second kind.[24, 69] Figure 2-12 shows the calculated deformation profile of the substrate due to a sessile water drop with a = 1 mm, t_l = 10 nm, $\theta = \theta_0 = 90°$ and ν = 0.5 using the equations (2.22), (2.23) und (2.24). Two different Young's modulus, E, 0.5 MPa and 30 MPa were used to emphasize the difference between a soft and a stiff substrate.

Deformation of the substrate due to a sessile drop is therefore present in different drop-substrate systems. The investigation of its influence on drop evaporation and related processes is still lacking.

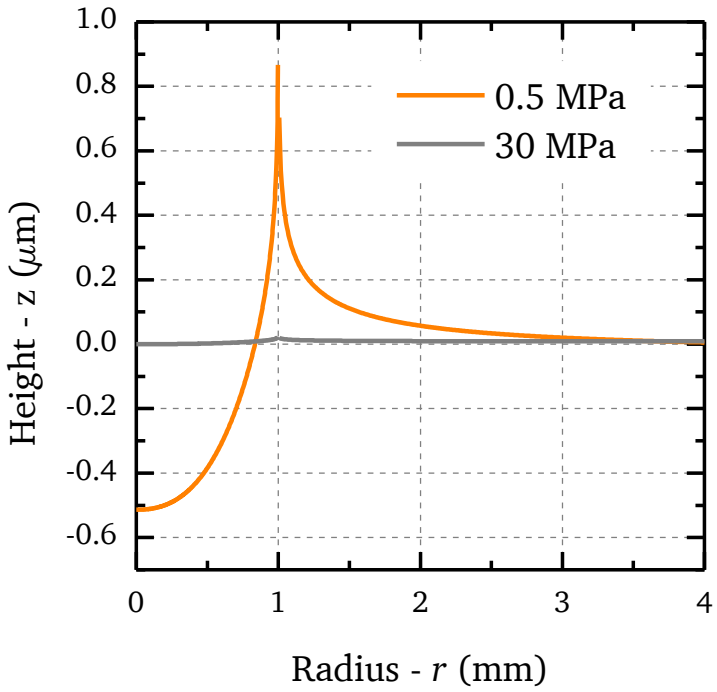

Figure 2-12: Calculated profile of the deformed substrate underneath a water drop using equations (2.22), (2.23) und (2.24). Two different Young's moduli were used, 0.5 MPa and 30 MPa.

3 Experimental and Numerical Methods

The main focus of this chapter is to describe how measurements and numerical simulations were performed. To achieve this, a precise description of the used set-ups, the working principles of measuring techniques, and numerical methods are presented.

3.1 Microscope Set-up for Sessile Drop Evaporation

Sessile drop evaporation experiments were performed using a set-up with two CCD cameras (Figure 3-1). The CCD cameras (BlueCOUGAR-S123, 1,360x1,024 pixel, Matrix Vision GmbH, Oppenweiler, Germany) were positioned orthogonal to each other allowing the imaging from both top and side view of the evaporating drop. This cameras were equipped with Navitar (Zoom 6000 System, Navitar, Rochester, USA) and Mitutoyo objectives (MPlanApo 2x, Mitutoyo, Kawasaki, Japan). Cold light source (KL 1600 LED, Schott, Mainz, Germany) with a diffusor illuminated the sessile drop from the back. The pixel resolution was variable and ranged from 1.026 up to 6.58 μm/pixel, allowing a maximal precision for length measurements of 0.5 μm. In general a frame rate of 0.5 Hz (one frame acquired every 2 s) was used for drop evaporation experiments. The camera allowed frame rates up to 30 Hz. The top view images were used to check the circular symmetry of the drops. Asymmetric drops were not analyzed.

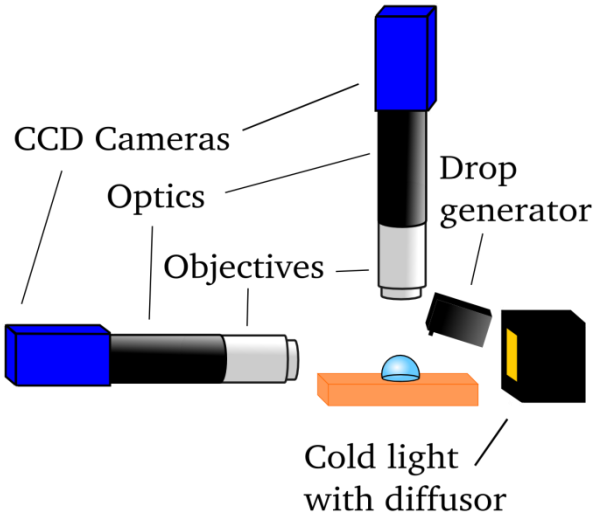

Figure 3-1: Scheme of the set-up for monitoring sessile drop evaporation.

Experiments from chapter 4 were performed in a custom made sealed chamber to prevent air drafts and contamination by dust particles. Temperature (accuracy ±0.3 °C) and relative humidity (accuracy ±1.8 % between 10 and 90 %) were controlled using a sensor built-in in the chamber (SHT75, Sensirion AG, Staefa, Switzerland). Experiments from chapter 5 were not performed in a chamber because liquid suspensions needed to be mixed just before drop generation (the temperature and humidity sensor were placed approx. 10 cm from the drop). For all experiments the temperature and the relative humidity were in the range of 24±2 °C and 37±3 %, respectively.

Water used in all experiments was ultra-pure (18.2 MΩcm, Sartorius Arium 611, Göttingen, Germany). Substrate samples were rinsed before experiments with ethanol, water, and dried in argon stream to remove any contaminations from the surfaces.

3.1.1 Drop Generation

Drops were generated either by an automatic drop generator (PipeJet P4.5, BioFluidix, Freiburg, Germany) or manually using a pipette (Acura manual 825, Socorex, Ecublens, Switzerland).

For experiments presented in chapters 4 and 6 drops of volume ranging from 0.12 μl to 0.60 μl were dispensed using the automatic drop generator, dispensing in a reproducible way drops with a volume of 0.012 μl. In order to produce drops with larger initial volume many drops were automatically generated on the same spot at a frequency of 5 Hz. The drops had an initial contact angle $\theta_0 = 102\pm5°$ and an initial contact radius $a_0 = 0.34\pm0.02$ mm, independent from the substrate.

For experiments in chapter 5 water-silica suspensions were prepared by diluting a silica suspension (SS04N, mean diameter of particles: 2.01±0.22 μm, Bangs Laboratories, Fisher, USA), from an initial concentration of 9.8 wt.% solid content to 0.0125 wt.% in ultra-pure water (18.2 MΩcm, Sartorius Arium 611, Göttingen, Germany). Just before deposition the suspension was stirred for 30 s with a vortex shaker (Vortex 3, IKA, Staufen, Germany) to ensure particles were homogeneously dispersed. Then a volume of 0.72±0.04 μl was dispensed on the substrates using the pipette. Here, drops had an initial contact angle $\theta_0 = 111\pm4°$ and an initial contact radius $a_0 = 0.565\pm0.032$ mm, independent from the substrate.

3.1.2 Image Analysis

Width, height, volume, contact angle and contact radius of the evaporating drop were calculated from the recorded videos using two self-written MATLAB (R2010a, MathWorks, Natick, USA) scripts (see Appendix). The first script transformed every frame from the videos into a black and white picture. A contrast threshold was used to differentiate between drop and illuminated background. The second script was used to extract the height, the contact radius and the curvature of the sessile drop after defining the ground line. From these values other relevant geometrical properties of the drop were derived, like volume and contact angle.

3.2 Contact Angle Measurements

Contact angle measurements were performed with two different devices. The first was a commercial drop and bubble shape tensiometer (PAT-1, Sinterface, Berlin, Germany), used to measure surface tension and static contact angles of substrates. The second device was an in-house built set-up to measure the contact angles for slow contact line velocities (~4μm/s). It consisted of a microbalance and two glass recipients connected by a silicone tube (see Figure 3-2).

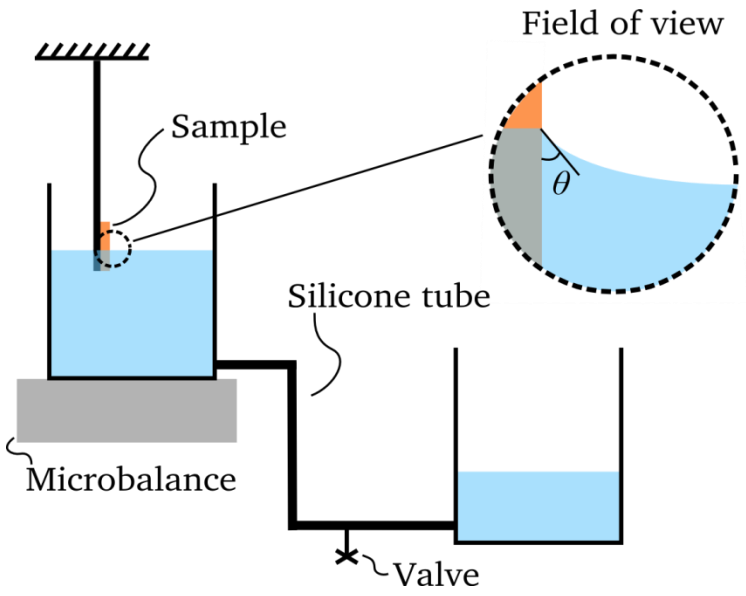

Figure 3-2: Scheme of the set-up for measuring receding contact angle at contact line velocities of ~4μm/s.

The substrate was submersed and fixed; the water could flow through the silicone tube from one recipient to the other driven by gravity. The speed of the liquid level was set by the height difference and a valve in the silicone tube, so that a controlled wetting/dewetting of the sample was achieved. Using the data of the microbalance and dimensions of the recipient the velocity of the liquid level was calculated. During the wetting/dewetting a CCD camera (BlueCOUGAR-S123, 1,360x1,024 pixel, Matrix Vision GmbH, Oppenweiler, Germany) recorded a video of the TPCL region as showed in the inset of Figure 3-2. Contact angle were then measured using freeware image analysis software (ImageJ, National Institutes of Health, Maryland, USA).

3.3 Set-up to Measure Substrate Liquid Load

In order to measure the liquid load hanging on a substrate while spraying droplets onto it, a set-up was developed by the bachelor student Angelika Sell using a microbalance (PCB 350 3, Kern, Balingen, Germany) and an airbrush-gun (AC-55, Conrad Electronic, Hirschau, Germany).[73] The airbrush-gun was fixed and directed towards a substrate hanging by a nylon string to the microbalance. A scheme of the set-up is shown in Figure 3-3. The microbalance recorded the mass change with time during the spraying process. After a certain increase in mass load, drops started to flow down the sample and trickled from the sample. The measured mass oscillated then around a mean value, which was characteristic for each surface.

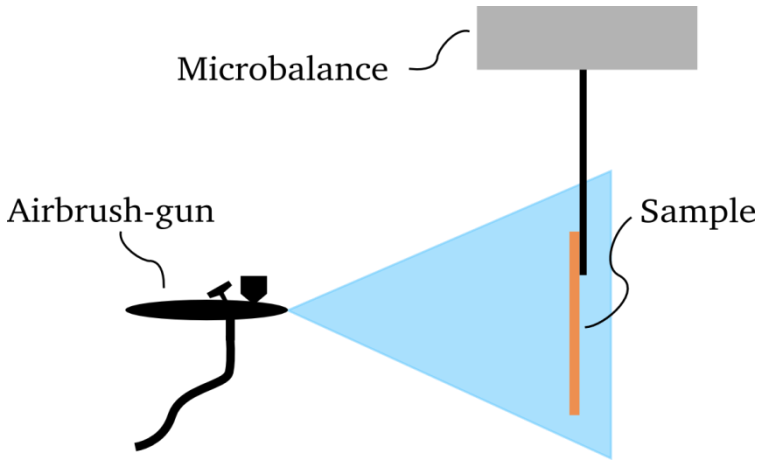

Figure 3-3: Scheme of the set-up for measuring the liquid load during substrate spraying.

3.4 Preparation of Elastic Substrates with different Young's Moduli

To prepare substrates with different elasticity (Young's modulus) polydimethylsiloxane elastomer (PDMS, Sylgard 184, Dow Corning, Wiesbaden, Germany) was used. This elastomer has already been used previously [24, 74] and is suitable for fabricating substrates with different elasticities, but with similar surface chemistry (i.e., wettability).

Silicon elastomers are composed of cross-linked polymer chains where the carbon atoms of the backbone are replaced by silicon atoms.[75] A single chain is called oligomer and is represented in the figures by strings. The oligomers, which are not cross-linked, will be able to flow under shear stress. When the chains are cross-linked a network (elastomer) will be formed and the material will not be able to flow under shear stress. Figure 3-4 shows a scheme of the formation of an elastomer from oligomers.

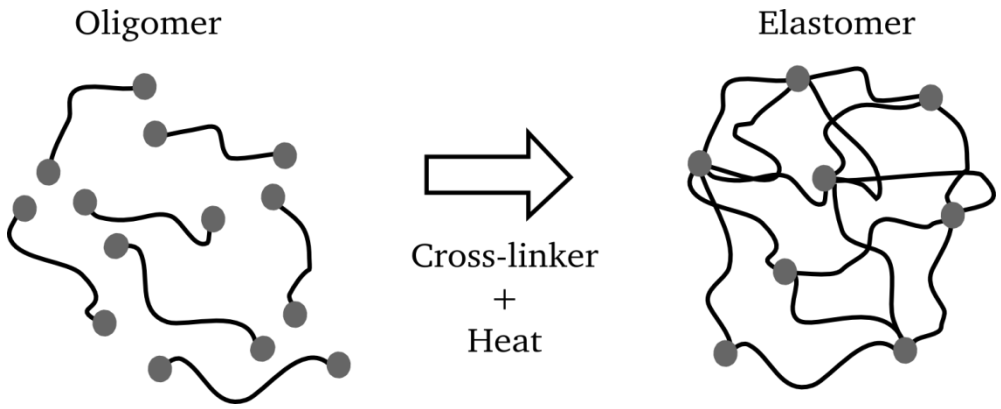

Figure 3-4: Scheme of the cross-linking process from oligomers to an elastomer. Molecular chains are represented by a string; linking points by circles. Representation based on [76].

The used PDMS, Sylgard 184 Silicone Elastomer kit from Dow Corning, is a commercial product, so the molecular weight of the oligomer it is not precisely known, nor if some additives are used. However, a chemical elemental analysis showed that the material is a siloxane. This type of PDMS system consists of an oligomer (base) and a cross-linker .[76] The cross-linking of the PDMS is done by heating it in an oven. According to the data sheet, a ratio of 10:1 (base:cross-linker) yields a Young's modulus of approx. 1.5 MPa. To modify the elasticity (Young's modulus) of the sample, different base to curing agent ratios (10:1, 20:1, 30:1, 40:1 and 50:1) were used yielding substrates with a Young's modulus from 1.5 MPa to 0.02MPa. Decreasing the cross-linker concentration in the mixture leads to a sparser oligomer

network [41] (Figure 3-5), leading to a higher mobility of the oligomers in the network, and consequently to a lower Young's modulus of the PDMS.

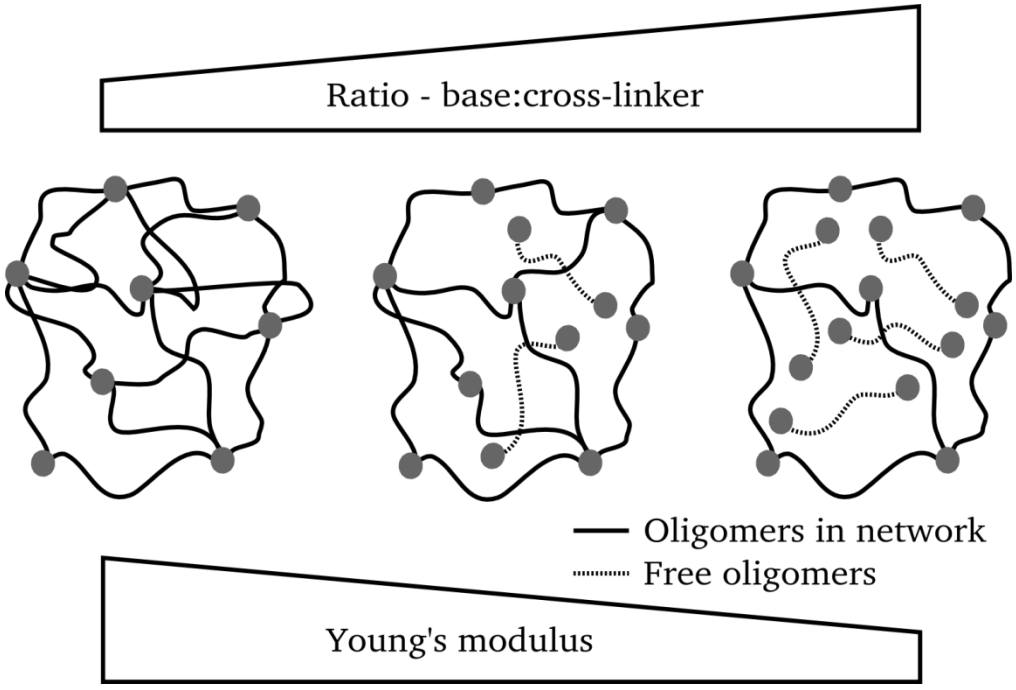

Figure 3-5: Representation of the PDMS elastomer networks formed for different base to cross-linker ratios. Oligomers bonded and not bonded to the elastomer network are represented respectively with solid and dashed lines.

The increase of the base to cross-linker ratio leads also to an increase of free oligomer chains inside the elastomer network. In order to produce similar surface chemistry and avoid an oligomer-layer on the PDMS surface, a washing procedure with tetrahydrofuran (THF, ROTISOLV, HPLC grade, Carl Roth) was developed. The sample preparation procedure consisted of 7 steps:

1) Mixing the different oligomer to cross-linking ratios (10:1, 20:1, 30:1, 40:1 and 50:1) for 5 minutes.
2) Degasing the mixture for 25 minutes in a vacuum chamber.
3) Fabricating the substrate (either by pouring into a mold or by spin coating).
4) Curing the samples overnight (12 hours) at 60 °C in an oven.
5) Immersing the samples in tetrahydrofuran (THF, ROTISOLV, HPLC grade, Carl Roth) for two days, replacing the solvent every day.

6) Drying the substrates in a closed, but not air-tight, recipient.

7) Rinsing the substrates with ethanol and water.

Thick substrates (used in chapter 4 and 5) were produced by simply pouring the mixture into molds (a polystyrene casting mold was used to facilitate the removal of the sample). For the spin coated samples (used in chapter 4) square glass slides (1 mm thickness, Carl Roth GmbH, Karlsruhe, Germany) were rinsed in acetone (technical grade) and sonicated (Elma, Singen, Germany) for 10 minutes with ethanol (ROTISOLV, HPLC grade, Carl Roth). Thin films of the mixture were then spin-coated (WS-400B-6NPP, Laurell, North Wales, USA) on the cleaned glass slides by applying a spin velocity of 1,000 rpm for 120 s.

The resulting film thickness, measured by a white-light confocal profilometer (μSurf Typ, Nanofocus AG, Oberhausen, Germany) was around 60 μm for the spin-coated and 1.5 mm for the mold-cast samples. The root mean square (RMS) surface roughness over an area of 5x5 μm^2 did not exceed 7 $\pm$3 nm for any of the measured surfaces. Roughness measurements were performed by Andreas Plog (TU Darmstadt, Experimental Interface Physics) with an atomic force microscope (MFP-3D, Asylum Research, Santa Barbara, USA) in non-contact mode. Measurements of receding and advancing contact angles (θ_r and θ_a) were performed by dipping (withdrawing) the PDMS substrates at a speed of 4 μm/s into (out of) a water pool as described in section 3.2 and are presented in Table 3-1.

Table 3-1: Elastic modulus, advancing and receding contact angle (θ_a/θ_r) for water on PDMS samples.

Sample	**PDMS 10:1**	**PDMS 20:1**	**PDMS 30:1**	**PDMS 50:1**
Young's modulus (MPa)	1.5	0.8	0.06	0.02
θ_a / θ_r (°)	113 / 78 $\pm$10	117 / 53 $\pm$10	119 / 41 $\pm$10	125 / 33 $\pm$10

3.5 Preparation of Substrates with different Thermal Properties

Glass and silicon substrates with 50x50 mm^2 area and 0.5 mm thickness were used to prepare the substrates investigated in chapter 6. Glass and silicon have a thermal conductivity, of 1.05 and 139.4 W/(m·K)[77] and a thermal diffusivity of 5.8×10^{-7} and 8.0×10^{-5} m^2/s.[78, 79] The wettability of the substrate was kept similar due to a coating of grafted layer of polystyrene,

produced by colleagues[1] according to the following procedure: The substrates were degreased in acetone and dichloromethane in an ultrasonic bath, and then put for 20 min in a 80-85 °C warm solution of 100 ml water, 8 ml concentrated ammonia and 8 ml hydrogen peroxide (35 %). The substrates were then blown dry with nitrogen, put for 30 min in a vacuum at 1 mbar, and put overnight in a solution of 25 ml toluene, 0.4 ml dry triethylamine and 0.2 ml starter ((3-(2-bromisobutyryl)propyl)dimethylchlorosilane). After that, the substrates were first rinsed with dichloromethane and further rinsed for 2 hours in a Soxhlet extractor before being used for polymer grafting.

The reaction took place in a modified Schlenk tube. At first 16.3 mg (0.11 mMol) of CuBr was added, then substrates were inserted and remained freely suspended. Under Argon atmosphere 12.5 ml degassed anisole was added, 12.5 ml degassed and freshly distilled styrene (11.3 mg, 0.11 mMol) and 24 μl (19.9 mg, 0.11 mMol) N,N,N',N',N"-pentamethyl-diethylenetriamine (PMDETA). After addition of 16.3 μl (21.7 mg, 0.11 mMol) 2-brombutirric acid ethyl ester (2-EIBBr) the solution was frozen/evacuated/thawed three times for removing the oxygen. The reaction mixture in the tube was then stirred for 3 days at 90 °C.

The wafers were rinsed with tetrahydrofuran and dichloromethane, and finally rinsed overnight in dichloromethane in a Soxhlet extractor in order to remove non-reacted free polymer. The contact angle of water drops on the freshly prepared glass and silicon substrates was 82° ±3°.

3.6 White-Light Confocal Profilometer

The white-light confocal profilometer (μSurf Typ, Nanofocus AG, Oberhausen, Germany) was used to acquire 3D topography images of the investigated substrates.

For understanding the measurement method of a white-light confocal profilometer, the principle of confocal microscopy will be explained first. In a confocal microscope the optical path is similar to a conventional microscope. But, instead of letting light from focused and unfocused regions reach the camera sensor, the confocal microscope uses a pin-hole to let only the light from the focused volume reach the sensor (Figure 3-6).[80] If objects are in the

[1] Marcus Schmelzeisen (Experimental Interface Physics, CSI, Technische Universität Darmstadt) and Gunnar Kircher (Max-Planck Institute for Polymer Research).

focal plane, their light intensity will be high; objects out of focus will have a low light intensity.

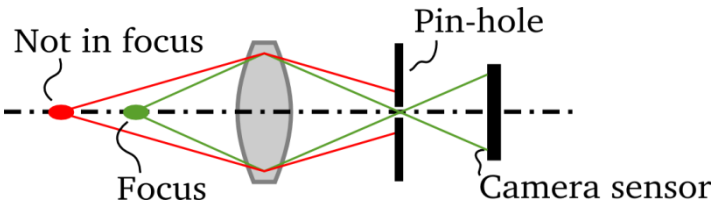

Figure 3-6: Scheme of the working principle of a confocal microscope.

In the white-light confocal microscope a rotating multi-pin-hole disk is used instead of a single pin-hole to scan the sample within the entire image field of the camera sensor. Here, like for the case of the pin-hole, only objects in focus have a high light intensity. A stack of images is created by scanning the surface at known piezo positions (z_{Piezo}), so that different regions of the sample are in focus at different images. After completing the image stack, the light intensity of every single pixel is analyzed throughout the stack images (see Figure 3-7). The respective z_{Piezo}, at which the maximal light intensity for a single pixel is found, contains the information of the sample height at this specific pixel. After analyzing all pixels, height data for the entire surface is generated. Using a 10x objective, 3D topography images with a respective lateral and vertical resolution of 3 μm and 10 nm were acquired.

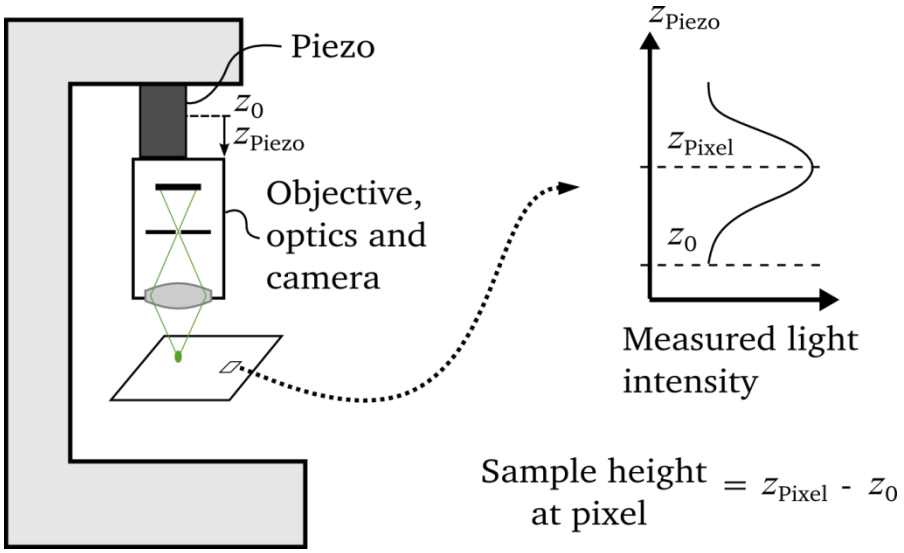

Figure 3-7: Scheme of the working principle a white-light confocal profilometer. Inset shows how sample height is determined for a specific pixel.

3.7 Inverted Microscope

Images of the particles inside the drop during the evaporation process showed in chapter 5 were acquired with a frame rate of 30 Hz using an inverted microscope (Eclipse TE 2000-S, Nikon, Japan, Tokyo) and a 10x objective (Plan Fluor, Nikon, Japan, Tokyo). An inverted microscope has its objectives and turret pointing up underneath the sample stage, so that the sample can be observed from the bottom.

3.8 Numerical Methods

In this section, details about the governing equations and boundary conditions used for the simulation of the deformation as well as the heat-transfer inside the substrate are presented.

3.8.1 Simulation of Substrate Deformation

Here the basics of the governing equations of elastic structures (equilibrium, kinematics, and elasticity) and the boundary conditions for the numerical simulation of the deformation of the substrate via interfacial or capillary forces is presented. The governing equations in this case represent field equations, which are used to describe the development of the field quantities displacement, deformation and stress (s_i , ε_{ij} and σ_{ij}) inside an elastic body.[81]

In the case of infinitesimal deformation and isotropic linear elasticity the field equation for equilibrium, kinematics and elasticity can be written respectively as:[81]

$$\sigma_{ij,j} + f_i = 0 \tag{3.1}$$

$$\varepsilon_{ij} = \frac{1}{2}\left(s_{i,j} + s_{j,i}\right) \tag{3.2}$$

$$\sigma_{ij,j} = c_{ijkl}\varepsilon_{kl} \tag{3.3}$$

with $c_{ijkl} = G\frac{(E-2G)}{3G-E}\delta_{ij}\delta_{kl} + G(\delta_{ik}\delta_{jl} + \delta_{il}\delta_{jk})$. The external volume force is represented by f_i, δ_{ij} is the Kronecker delta, G and E are respectively the shear and Young's modulus of the elastic material. In order to solve the equations above and calculate the resulting deformation, one needs to define the boundary conditions for the volume field. Normally, two different boundary conditions can be imposed at the surface of the volume: defined stress or defined displacement.

The deformation caused by a sessile drop on a soft PDMS substrate, which is supported by a rigid glass slide (Figure 3-8), was investigated. By considering the three-dimensional stress condition in the elastic body and the influence of the rigid glass on the deformation, the three equations of solid elastic equations (3.1), (3.2) and (3.3) were solved for the PDMS substrate using finite element methods (FEM) with COMSOL Multiphysics (Comsol, Stockholm, Sweden). The numerical solver is based on the principle of virtual work. In the range of calculated deformations, smaller than 10 μm, the substrate can be considered isotropic and linearly elastic.

The left part of Figure 3-8 shows a scheme of a sessile drop with contact radius a, contact angle θ, and radius of curvature K on a deformable substrate, and its respective boundary conditions. As explained in section 2.3.3, the surface tension of a sessile drop, γ, acts on the elastic substrate causing a deformation: a ridge is pulled up at the TPCL, while the Laplace pressure $\Delta p_L = 2\gamma/K$ under the drop pushes the contact area into the substrate.

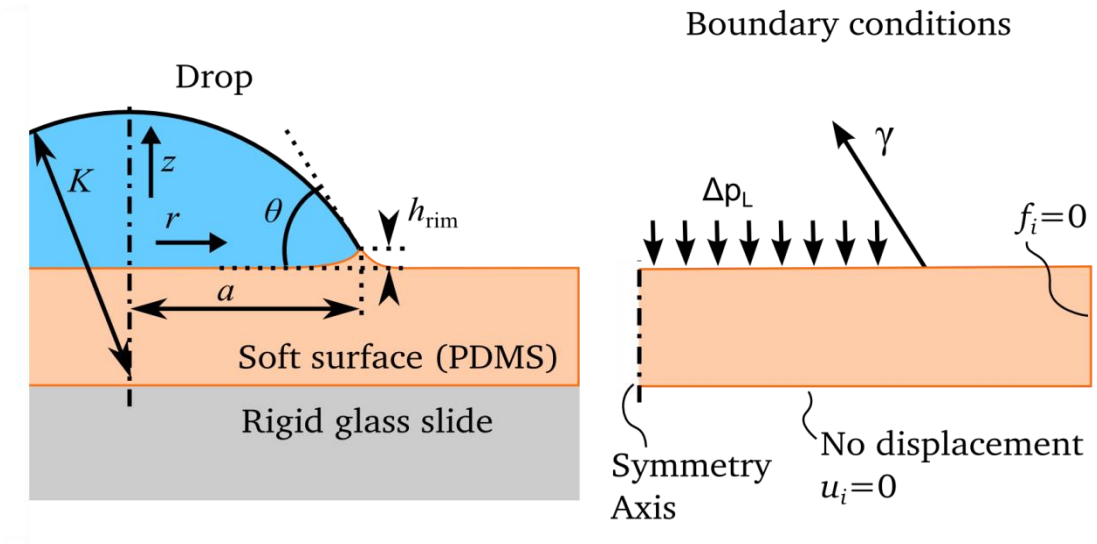

Figure 3-8: Scheme of a sessile drop on a soft substrate showing the contact radius a, contact angle θ, radius of curvature K, deformation height at the rim h_{rim}, and the directions of the z and r coordinates. At the right part the scheme show the boundary conditions applied to the soft substrate to simulate the deformation of the surface upon the influence of a sessile drop, indicating the surface tension γ and Laplace pressure Δp_L.

To account for the Laplace pressure the boundary pressure underneath the drop is assigned to be $\Delta p_L = 2\gamma/K$. The vertical and the horizontal component of the surface tension were taken

into account by setting a line stress at the TPCL ($r = a$) in the surface normal direction as $F_z = \gamma \sin(\theta)$ and in the radial direction as $F_r = \gamma \cos(\theta)$.

The nodes on the axis of symmetry were set to only move in the vertical direction mimicking the axial-symmetry of the system. The nodes at the bottom of the film followed the no displacement boundary condition ($u_i = 0$) to mimic the adhesion between the soft substrate and the rigid glass slide. The other boundaries of the film were free to deform upon mechanical stress ($f_i = 0$).

For the simulation a mesh consisting of about 16,000 triangular elements was used. This resulted in 65,000 degrees of freedom. Close to the TPCL the elements were about 5 times finer in order to improve the resolution of the deformation profile on the substrate. The results of the numerical simulation did not change when the quality of the mesh grid was further increased.

The deformation was simulated for the transition time from CCR to CCA evaporation, i.e. when the TPCL starts moving, for the different substrates. The thickness of the PDMS film was 60 μm and the lateral extension of the substrate was always more than three times the drop radius (300 μm). The receding contact angle from the experimental observations were used: 95°, 70°, 60° and 35° for the PDMS 10:1, 20:1, 30:1 and 50:1. From previous work[41] it was known that the surface energy of the used substrates is similar because the initial contact angles and contact radii of the drops are similar (deviation of 5 % and 5.8 % for the contact angle and contact radius, respectively). The Poisson's ratio of the substrate was set to $\upsilon = 0.5$, in accordance to the supplier's information. The comparison between calculated and measured (imaged by a white-light confocal profilometer described in section 3.6) deformation profile are presented in the section 4.3

3.8.2 Simulation of Substrate Heat-Transfer

This section describes the numerical methods used by collaboration partners[2] to describe the heat-transfer process inside substrate during sessile drop evaporation accounting for thermal properties of the substrate.

[2] Tatiana Gambaryan-Roisman and Peter Stephan from the Institute of Technical Thermodynamics, Technische Universität Darmstadt

Two governing equations were used to describe the simulated system of the evaporating drop and the heat transport in the substrate and drop. Transient diffusion of water vapor in the gas is described by the diffusion equation:

$$\frac{\partial c}{\partial t} = D\left[\frac{1}{r}\frac{\partial}{\partial r}\left(r\frac{\partial c}{\partial r}\right) + \frac{\partial^2 c}{\partial z^2}\right] \tag{3.4}$$

Here is c the vapor concentration in gas, D is the diffusion coefficient of vapor in gas, t is the time, r and z are respectively the radial and axial coordinates. The concentration of water vapor at the boundaries of the domain was set to be equal to the far-field concentration (c_∞):

$$c = c_\infty \quad \text{at} \quad z = h_{\text{sub}} + h_{\text{gas}} \quad \text{and} \quad \text{at} \quad r = r_{\text{sub}}, \quad h_{\text{sub}} < z < h_{\text{sub}} + h_{\text{gas}} \tag{3.5}$$

Here h is the height and the subscripts "sub" and "gas" mean substrate and gas respectively. Substrate was set to be impermeable to water vapor:

$$\frac{\partial c}{\partial z} = 0 \quad \text{at} \quad h = h_{\text{sub}}, \quad a < r < r_{\text{sub}} \tag{3.6}$$

The transient heat transport in the substrate and in the droplet is described by the heat conduction equation:

$$\frac{\partial T}{\partial t} = \alpha\left[\frac{1}{r}\frac{\partial}{\partial r}\left(r\frac{\partial T}{\partial r}\right) + \frac{\partial^2 T}{\partial z^2}\right] \tag{3.7}$$

T is the temperature and α is the thermal diffusivity. It was assumed that all the surfaces of the substrate, except for the substrate-drop interface, are thermally insulated because the supporting surface area was minimal:

$$\frac{\partial T}{\partial t} = 0 \quad \text{at} \quad z = 0 \quad \text{and} \quad \text{at} \quad z = h_{\text{sub}}, \quad a < r < r_{\text{sub}} \tag{3.8}$$

$$\frac{\partial T}{\partial r} = 0 \quad \text{at} \quad r = r_{\text{sub}}, \quad 0 < z < h_{\text{sub}} \tag{3.9}$$

Here, is a the contact radius. Moreover, following conditions were held at the substrate-liquid interface:

$$T|_{\text{sub}} = T|_{\text{l}}, \qquad k_{\text{sub}}\frac{\partial T}{\partial z}\Big|_{\text{sub}} = k_{\text{l}}\frac{\partial T}{\partial z}\Big|_{\text{l}} \quad \text{at} \quad h = h_{\text{sub}}, \quad 0 < r < a \tag{3.10}$$

Here, k is the thermal conductivity and the subscript "l" refers to the liquid. The heat flux in the droplet at the liquid-gas interface ($S_{\text{l-gas}}$) was assumed to be proportional to the evaporation flux, or to the local mass flux of the water vapor at the gas side:

$$k_{\mathrm{l}}(\nabla T \cdot \mathbf{n})_{\mathrm{l}} = h_{\mathrm{lv}} D(\nabla c \cdot \mathbf{n})_{\mathrm{gas}} \quad \text{at} \quad S_{\mathrm{l-gas}} \tag{3.11}$$

where h_{lv} is the evaporation enthalpy, and $\mathbf{n}$ the unit normal vector directed perpendicular to the liquid-gas phase. A local equilibrium at the liquid-gas interface was assumed so that the local partial pressure of the water vapor is equal to the saturation pressure p_{sat}. Small temperature variation was assumed, so that the temperature dependence of p_{sat} can be expressed by a linear relationship given by the Clausius-Clapeyron equation.[82]

The governing equations (3.4) and (3.7) together with the mentioned boundary conditions were solved using finite elements method (FEM) implemented in the Matlab PDE Toolbox. A mesh consisting of a total of 8,122 triangular elements was used and changes of the results upon the increase of elements were negligible.

4 Influence of Soft Substrate on the Sessile Drop Evaporation[3]

Technical applications like crop spraying[3], spray cooling[4], heat exchange processes, combustion, measurement of diffusion coefficients in polymer films[6] and inkjet-printing[7] rely on the physics of the evaporation of sessile drops. Controlling the evaporation of sessile drops is therefore of crucial importance. For a reproducible and reliable handling of small quantities of liquids, e.g. in microfluidic and lab-on-chip applications, evaporation plays a major role and needs to be well understood, predicted and controlled. Actually, biological sample analysis (lab-on-chip) and microfluidic devices are often made of soft polymers such as PDMS due to its good casting properties and chemical inertness. In order to simplify the cleaning process, many devices made of PDMS are "open", such that the liquid sample to be analyzed is exposed to the environment. Consequently, it is crucial to understand how elasticity of the substrate, influences the evaporation of drops in order to improve both the design and performance of such devices. A further example of drop evaporation on soft tissue is sweat evaporation from the skin, which is essential for the thermoregulation of humans.[83]

As described in section 2.3.3, capillary forces can deform the substrate in the vicinity (several tens of micrometers) of the TPCL.[84] Moreover, previous works showed that the elasticity of the substrate influenced, for example, the contact angle hysteresis[85], spreading of drops [86-89], condensation of water on PDMS substrates[74] and the dynamic wetting.[41] Recent experimental work confirmed the existence of the deformation of soft substrates in the order of micrometers due to interfacial and capillary forces exerted by micrometer to millimeter sized drops.[24, 25, 90, 91] How does the deformation of soft substrates influence the evaporation of sessile drops?

In this chapter it is shown that substrate deformation influences the evaporation of sessile water drops and that by controlling deformation the control of evaporation is achieved. Evaporation experiments were conducted on PDMS substrates (see in section 3.4) with similar surface chemistry, but different Young's modulus. It was possible to find a direct relation between the evaporation mode and substrate elasticity, which in turn affects the overall evaporation time.

[3] This chapter is based on the publication "M. C. Lopes, E. Bonaccurso, *Evaporation control of sessile water drops by soft viscoelastic surfaces*, Soft Matter, **8**, 7875-7881, (2012)".

4.1 Developing a Relation between CCR and CCA Evaporation Time

A relation between the evaporation time of a drop evaporating in CCR mode (t^{CCR}) and of a drop evaporating in CCA mode (t^{CCA}) was derived in order to predict the evaporation time of drops with different receding contact angles. Instead of focusing on the description of the evaporation rate assuming different volumes or different ambient conditions like in previous works[8, 10], a simple approach was adopted to predict the evaporation time of drops with equal initial volume and contact angle, but evaporating in different modes.

For the CCR evaporation mode the evaporation rate $\dot{V}^{\mathrm{CCR}}$ is proportional to the contact radius a of the sessile drop (section 2.2.2). Accordingly, when a drop evaporates in CCR mode (a is constant), its evaporation rate is constant throughout the entire process. As described in section 2.2.2, this constant evaporation rate has been observed before[92, 93] and one can describe the volume of a drop evaporating in the CCR mode, V^{CCR}, as function of the initial volume, V_0, and the evaporation time, t^{CCR}, using equation (2.8). For the CCA evaporation mode under similar initial conditions the volume decreases according to a power law with exponent 3/2 in time, as described before in equation (2.11).[10, 17]

Assuming identical environmental and geometrical initial conditions, two drops must show the same initial evaporation rate at $t = 0$, independently of their future evaporation mode:

$$\dot{V}^{\mathrm{CCR}}\big|_{t=0} = \dot{V}^{\mathrm{CCA}}\big|_{t=0} \tag{4.1}$$

Using equations (2.8) and (2.11) the evaporation rates for both the CCR and CCA modi can be calculated as:

$$\dot{V}^{\mathrm{CCR}} = -\frac{V_0}{t^{\mathrm{CCR}}} \tag{4.2}$$

$$\dot{V}^{\mathrm{CCA}} = -\frac{3}{2}\frac{V_0}{t^{\mathrm{CCA}}}\sqrt{1-\frac{t}{t^{\mathrm{CCA}}}} \tag{4.3}$$

With equations (4.1), (4.2) and (4.3) following relation between t^{CCA} and t^{CCR} follows:

$$t^{\mathrm{CCA}} = \frac{3}{2}t^{\mathrm{CCR}} \tag{4.4}$$

A drop evaporating in CCA mode needs about 1.5 times longer to evaporate than the same drop evaporating in CCR mode. Throughout this work this relation is used to predict the

theoretical limits of the evaporation and to make a comparison between drops evaporating in different modes, but with similar initial conditions.

The evaporation time (t_{evap}) can be predicted using equation (4.4) for a given drop in dependence of the initial evaporation rate ($\dot{V}_0 = \dot{V}\big|_{t=0}$) and the receding contact angle θ_{r}:

$$t_{\mathrm{evap}} = \frac{(V_0 - V_{\mathrm{CCA}})}{-\dot{V}_0} + \frac{3}{2}\left[\frac{V_0}{-\dot{V}_0} - \left(\frac{V_0 - V_{\mathrm{CCA}}}{-\dot{V}_0}\right)\right] \tag{4.5}$$

Here, V_0 is the initial volume and V_{CCA} is the volume of the drop when the CCA mode starts, which depends on the initial contact radius a_0 and receding contact angle θ_{r}:

$$V_{\mathrm{CCA}} = \frac{\pi a_0 \tan(\theta_{\mathrm{r}}/2)}{6}(3{a_0}^2 + [a_0 \tan(\theta_{\mathrm{r}}/2)]^2) \tag{4.6}$$

The initial evaporation rate was calculated using the equation from Schönfeld et al.:[51]

$$\dot{V}_0 = -2\pi D \cdot \Delta P \cdot \frac{a_0 M}{\rho R T} \cdot \frac{f}{\sin(\theta_0)} \tag{4.7}$$

Here, D is the diffusion coefficient of water vapor in air, ΔP is the difference between saturated and ambient vapor pressure, M is the molar mass from liquid, ρ is the liquid density, R is the universal gas constant, T is the temperature and $f = 0.00008957 + 0.6333\theta_0 + 0.116{\theta_0}^2 - 0.08878{\theta_0}^3 + 0.01033{\theta_0}^4$. Equation (4.5) was used to compare the experimental evaporation time of substrates with different Young's modulus.

4.2 Soft Substrate Decreases the Evaporation Time of a Sessile Drop

The curves in Figure 4-1 show the drop volume vs. time for drops with an initial volume $V_0 \approx 0.12\,\mu$l on PDMS substrates with Young's moduli ranging between 0.02 and 1.5 MPa, and with a thickness of 60 μm. The data is presented in a semi-log plot to emphasize different evaporation times on different substrates. Using equations (2.8), (2.11) and (4.5) the drop volume decrease was predicted for the CCR and CCA evaporation modes. The solid curve represents the evaporation in the CCA and the dashed curve in the CCR mode. Initial evaporation rate $\dot{V}_0$ was calculated using $D = 2.4$ x 10-5 m^2/s, $M = 0.018$ kg/mol, $R = 8.3145$ J/(mol K), $\rho = 997$ kg/m^3, $\theta_0 = 90°$, $T = 297$ K, $a_0 = 0.34$ mm and $\Delta P = 1585.8$ Pa, an initial evaporation rate $\dot{V}_0 = $ -5.907 x 10-13 m^3/s is found. Using this initial evaporation rate it was possible to calculate $t^{\mathrm{CCR}} = 203$ s for a $V_0 = 0.12\,\mu$l and using

equation (4.5) a value $t^{CCA} = 305$ s was found for the CCA mode. It was similar to the measured value on the PDMS substrate 10:1 that shows a close-to-ideal CCA mode. Drop evaporation experiments for each substrate were conducted at least 15 times; typical curves are shown for each experiment. Error bars are smaller than the used symbols (maximal 3 % of the volume) and are shown in Figure 4-1 and Figure 4-2 for the first and last data point of PDMS 10:1 curves.

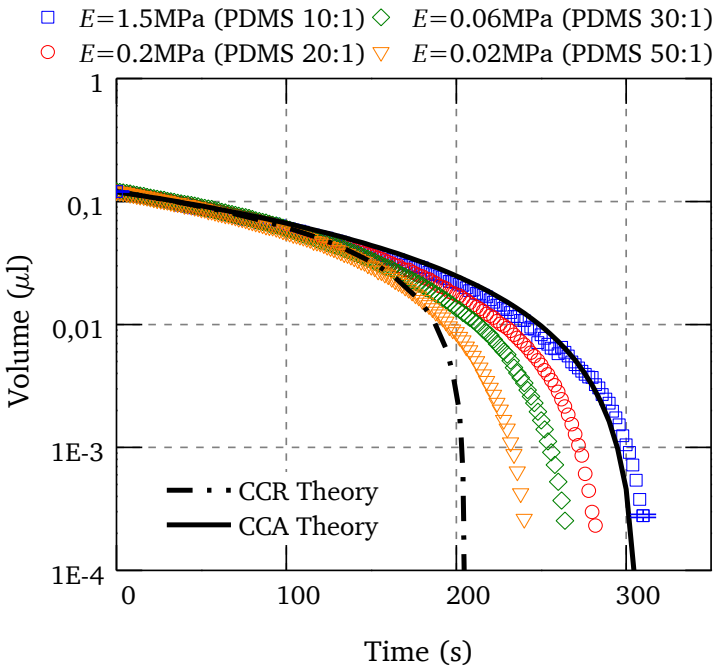

Figure 4-1: Volume change of sessile water drops during evaporation. The symbols represent the experimental data on different soft polydimethylsiloxane (PDMS) substrates. The solid and dashed lines represent the predicted volume change in CCR mode from equation (2.8) and in CCA mode from equation (2.11). Error bars are represented only for two data points (blue squares) for clarity and are similar for all curves

In the initial phase of evaporation, when drops evaporate in the CCR mode, the evaporation rate is similar for all substrates. This is consistent with the prediction that the evaporation rate is proportional to the contact radius of the drop.[1, 8, 51] In the experiments all drops have similar initial contact radii and therefore similar initial conditions. As evaporation goes on the influence of the substrate becomes evident: the evaporation rates start to differ, and differences between drop volumes increase. Interestingly, drops on softer substrates (lower Young's modulus) evaporate faster than on harder substrates (higher Young's modulus).

Experiments were repeated on thicker PDMS substrates with qualitatively similar results. The main difference between thin and thicker PDMS substrates was the smaller receding contact angle on the thick substrates (PDMS 10:1, 20:1, 30:1 and 50:1 have θ_r ~80°, 35°, 27° and 10°, respectively) leading to a slighter shorter evaporation time. Further investigation was focused on thin films, because deformation is restricted to a smaller region close to the TPCL. This made it easier to control the region where deformation arose and therefore to investigate its influence on evaporation.

How can elasticity (Young's modulus) of the substrate affect the evaporation time of otherwise identical drops? Figure 4-2 (left) presents a plot of the normalized contact radii, a', as a function of the evaporation time. The radii are normalized to the respective initial contact radii, a_0. The softer the substrate is, the longer drops evaporated in the CCR mode. As the evaporation rate is proportional to a, this directly lead to a shorter evaporation time on softer substrates.

The receding velocity of the TPCL is the slope of the curves in Figure 4-2 (left). During CCA evaporation the TPCL receding velocity was in the order of a few micrometers per second and was higher on softer substrates. Also, on the hardest substrate the evolution of the contact radius agreed with the contact radius expected in CCA evaporation. On the softest substrate the experimental curve was closest to the contact radius expected in CCR evaporation.

In Figure 4-2 (right) the normalized contact radii, a', are plotted as a function of the respective contact angles, θ. The expected CCR and CCA evaporation modes are indicated by the horizontal and vertical lines. The starting point of the evaporation was at the top right corner of the graph ($t = 0$), characterized by $\theta = 105°$ and $a' = 1$. All drops started evaporating in the CCR mode and switched to the CCA mode when $\theta = \theta_r$. From then on the contact radius of the drop decreased continuously. During the final stage of evaporation it was possible to observe changes in the drop geometry due to the high evaporation rate in relation to the remaining drop volume. This lead to a larger scattering of the experimental data for small contact radii.

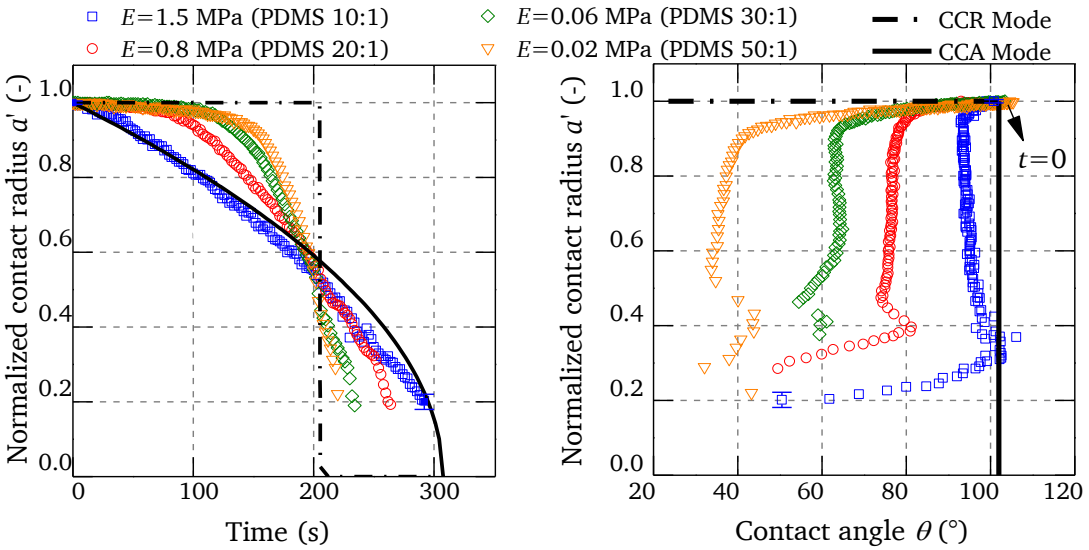

Figure 4-2: Left: normalized contact radii of sessile drops during evaporation. Right: geometry of a sessile drop during evaporation. The symbols (color online) show the experimental data on different soft PDMS substrates. The solid and dashed lines represent the radius of a drop evaporating in CCA and CCR mode, respectively. Error bars are shown for two data points only (blue squares) for clarity and are similar for all curves.

Figure 4-2 shows the main difference between drop evaporation on substrates with different elasticity. The different receding contact angles lead to different transition times from CCR to CCA evaporation. On the hardest substrate (PDMS 10:1) $\theta_r \approx 95°$ and after the transition the drop evaporated in a neaarly ideal CCA mode. The softest substrate showed the smallest θ_r leading to a longer duration of the CCR mode and to a shorter total evaporation time. So it is clear that evaporation time of a sessile drop was shortened by decreasing the Young's modulus of the substrate. But, what is driving the sessile drop to have a different receding contact angle θ_r ?

4.3 Control of Evaporation Mode by Substrate Deformation

In this section experimental and numerical work connecting the deformation of the substrate to the different θ_r on substrates with different Young's modulus is presented.

Figure 4-3 shows the deformation of different substrates. The dots represent experimental deformation profiles acquired by a white-light profilometer (section 3.6) outside of the drops,

while the solid lines are the FEM simulations (section 3.8). By this imaging technique it was not possible to track the deformation of the substrate underneath the drop. For each substrate three experimental profiles acquired for drops evaporating in the CCA mode with $\theta = \theta_r$ and $a \approx 0.3$ mm are shown. The simulations also show the deformation profile under the drop, which cannot be imaged by the profilometer.

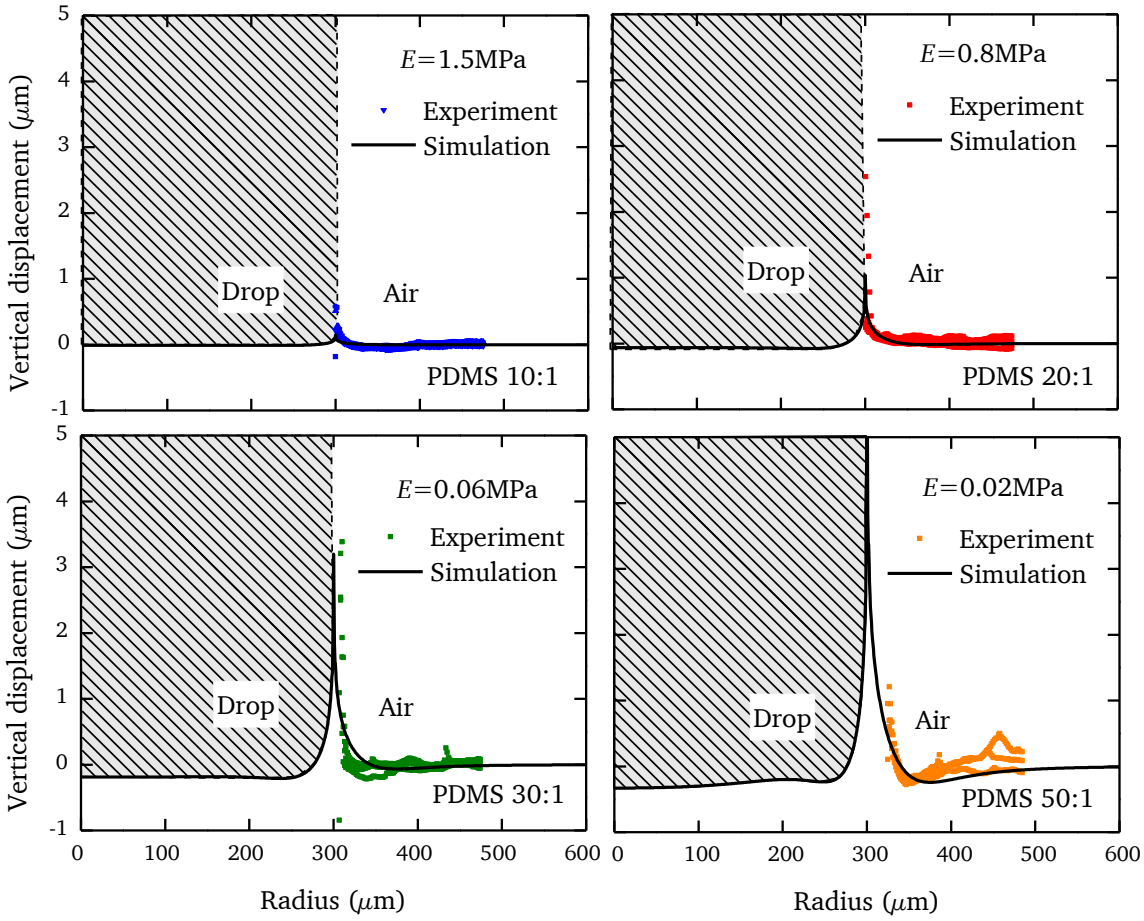

Figure 4-3: Profiles of deformed substrate due to drop interfacial forces. The dots show experimental data. The solid lines show the of the FEM simulations.

The simulations agreed very well with the experimental profiles and no free fitting parameters were used. Slight differences between experiment and simulation for the softst substrate (PDMS 50:1) were observed, which are still not understood. For thin substrates the deformation profile underneath the drop was very shallow due to the proximity of the rigid glass interface.[25]

Figure 4-4 shows experimental and theoretical evaporation times of sessile water drops with an initial volume of 0.12 μl in dependence of the receding contact angle. For the theoretical curve it was assumed CCR evaporation from the start and CCA evaporation as soon as θ_r was reached, which roughly corresponded to the experiments. Equation (4.5) was used to predict the evaporation time. The bars show the scattering of the experimental data. Equation (4.5) predicts well the experimental evaporation time of drops depending on θ_r. This confirmed that different evaporation times are related to different receding contact angles, which in turn are determined by the magnitude of substrate deformation, which in turn is controlled by its elasticity.

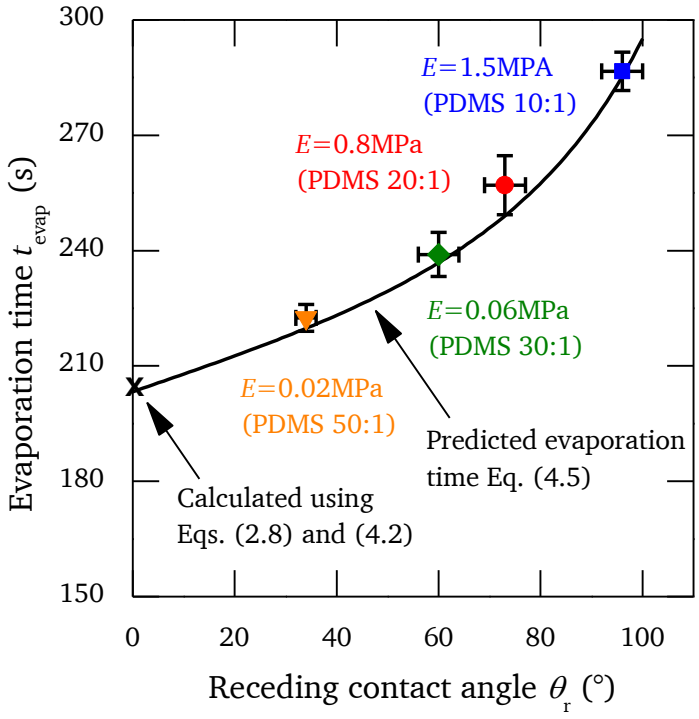

Figure 4-4: Evaporation time of sessile drops vs. receding contact angle. Evaporation time for θ_r=0° was calculated using equations (2.10) and (4.2). The solid line is the plot of equation (4.5).

By fabricating substrates or surface coatings with given elasticity (Young's modulus) it was possible to control the receding contact angles and to empirically predict the evaporation time of drops on them by equation (4.5). But, is it also possible to design or predict the receding contact angle of a soft substrate?

The left part of Figure 4-5 shows the measured receding contact angles versus the Young's moduli of the substrates. As expected, the receding contact angle decreased for decreasing elasticity of the substrate. Previous works on the influence of solid micro-deformations on contact angle equilibrium[86] showed that the deformation height of the substrate at the drop rim, h_{rim} see Figure 3-8, is proportional to the inverse of the elastic modulus and therefore proportional to the deformation energy ($h_{\max} \propto 1/E \propto \varepsilon_{\mathrm{defor}}$). The extra energy stored in the deformation of the soft substrates acts as a barrier for the depinning of the TPCL. The right part of Figure 4-5 shows the dependence of the measured receding contact angle of the drop on $h_{\max}$. Previous work on similar substrates[90] showed that the deformation height of the substrate at the drop rim, $h_{\max}$, can be related to surface tension, contact angle – in this case θ_{r} – and Young's modulus via $h_{\max} = \mathrm{C}\,\gamma \sin(\theta_{\mathrm{r}})/E$, where C is a parameter that includes dependences on drop size, film thickness, and material properties like Poisson's ratio υ. It is possible to rearrange the above relation to $\theta_{\mathrm{r}} = \arcsin(h_{\max} E/\mathrm{C}\,\gamma)$ and insert the values of the known parameters ($\gamma = 0.072$ N/m, Young's moduli and h_{rim} measured for the four different PDMS substrates. The best fit between measured and calculated receding angles was obtained for $\mathrm{C} \approx 0.33$ for all substrates. The receding angles in order of decreasing Young's modulus were: $\theta_{\mathrm{r}} = 96$, 75, 63, and 27° (Fig. 7, right - diamonds). Further investigations are however are needed to identify the components of C in the order to predict the receding contact angle directly from the mechanical properties of the substrate.

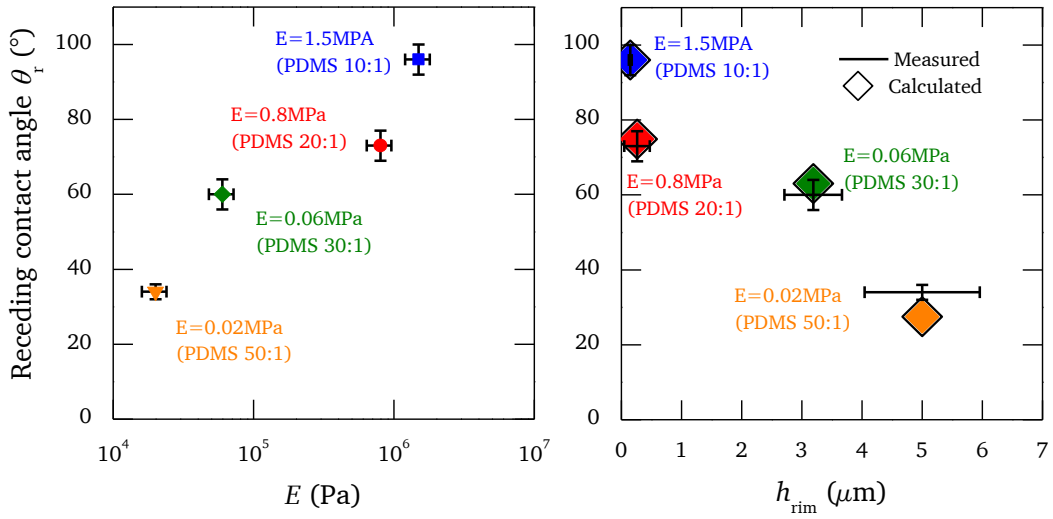

Figure 4-5: Left: receding contact angles vs. Young's moduli of four differently soft substrates. Right: measured (crosses) and calculated (diamonds) receding contact angles vs. rim height h_{rim}.

4.4 Conclusion

It is possible to control the evaporation mode and therefore the evaporation time of sessile drops by tuning the elasticity (Young's modulus) of the substrate: (i) drops deformed soft elastic substrates due to capillary forces, the deformation and the associated elastic energy stored in the deformation being larger on softer substrates; (ii) drop rims remained pinned for a longer time on more heavily deformed substrates during evaporation, since more energy is required for TPCL depinning; (iii) longer pinning determined a longer duration of the constant contact radius evaporation mode. In fact, two drops with similar initial volume, contact angle, and contact radius evaporated 33 % faster in the constant contact radius mode than in the constant contact angle mode.

5 Control of Deposition Patterns Using Soft Substrates[4]

As explained in section 2.3.2, one characteristic particle-deposition-related effect common to nearly all the coffee drinkers is the so called coffee-stain effect.[9] After the evaporation of a drop of coffee on a surface, a typical circular stain is observed with darker borders. This ring is formed by minute coffee powder grains accumulating at the rim of the drop during an interplay of processes associated with the evaporation of water[9]: pinning of the contact line, evaporative cooling and convective flow inside the drop due to Marangoni effects. As described in section 2.2.3, the evaporative flux of water is highest at the rim of pinned droplets, and inversely proportional to the contact angle of the drop.[14, 34, 53]

Chapter 4 shows how to control the evaporation of sessile drops of pure water using elastic substrates. Thus, it was possible to control the evaporation mode, and, therefore, the evaporation time of sessile drops by tuning the elasticity of the substrate. A similar work by Pu and Severtson[94] reinforced these observations and explanations. This chapter presents investigations on the influence of substrate elasticity on particle deposition patterns upon the evaporation of sessile drops of water-silica suspensions. Further, a simple model describing the receding velocity of the contact line during evaporation of pure liquids was developed. Finally, it will be shown that the deposition pattern can be sensitively controlled by substrate elasticity.

5.1 Predicting the Contact Line Velocity for Evaporating Drops on Soft Substrates

In this section a prediction for the receding velocity of the contact line for pure liquid drops evaporating on soft substrates is derived. The main forces acting on the contact line were balanced in order to describe its movement. The movement of the contact line on a deformable substrate (Figure 5-1) is driven by the capillary force and resisted by two forces or sources of dissipation: (I) deformation of the substrate at the contact line (viscoelastic dissipation) and (II) sliding of the contact line on the substrate (friction).[89] Balancing these contributions enabled the prediction of the contact line velocity of an evaporating drop in dependence of substrate elasticity.

[4] This chapter is based on the publication "M. C. Lopes, E. Bonaccurso, *Influence of the substrate elasticity on deposition patterns from evaporating droplets of water-silica suspensions*, Soft Matter, **9**, 7942-7950 (2013)".

The rate of change of work performed by the capillary force to move the contact line can be written as:[87]

$$\dot{W}_{\mathrm{cap}} = 2\pi a U \gamma (\cos\theta_{\mathrm{r}} - \cos\theta_0) \tag{5.1}$$

Here, $U = -\mathrm{d}a/\mathrm{d}t$ is the receding velocity of the contact line, γ the surface tension of the liquid, a the contact radius of the sessile drop, θ_{r} and θ_0 are, respectively, the receding and the equilibrium contact angles (see scheme in Figure 5-1).

The elastic substrate stores energy in form of deformation, which can be taken proportional to the height of the substrate ridge at the drop rim, h_{rim}, according to:[89]

$$\varepsilon_{\mathrm{def}} \propto 2\pi a h_{\mathrm{rim}} \gamma \tag{5.2}$$

$h_{\mathrm{rim}} \propto \gamma \sin\theta / E$,[24, 25, 95] with E being the Young's modulus of the substrate. This is valid as long as a is considerably larger than the distance ξ, within which the largest amount of the deformation energy is stored.

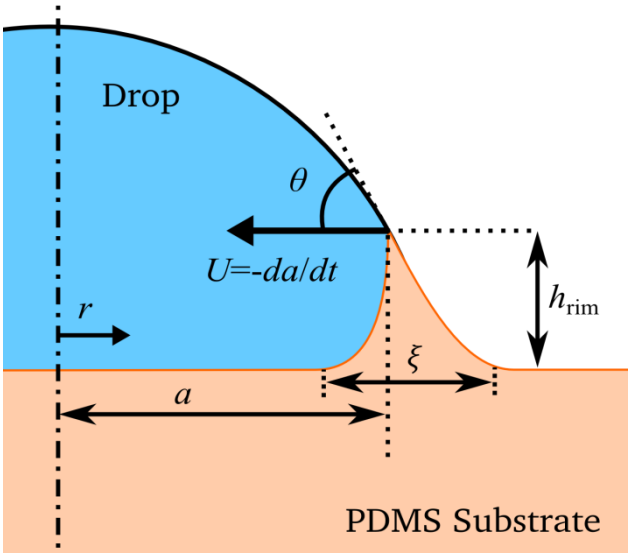

Figure 5-1: Scheme of the sessile drop sitting on a deformable substrate showing the contact radius a, contact angle θ, height of the substrate ridge at the drop rim h_{rim}, contact line velocity U, distance ξ, and the radial coordinate r. Deformation of substrate is not to scale.

During evaporation the contact line recedes and a decreases, and consequently the volume of the deformed substrate is reduced. Upon this the amount of energy stored in the deformation

decreases, i.e. elastic energy is released and can be partially used to drive the motion of the contact line. Another part of the released energy will be consumed by viscoelastic dissipation and will not be available for the movement of the drop. The rate of change of work related to the deformation, $\dot{W}_{\mathrm{def}}$, can be described by deriving the deformation energy with respect to time. The dissipated part is denoted by a constant Δ, like previously done in a work by Shanahan[87]:

$$\dot{W}_{\mathrm{def}} = -2\pi \dot{a} h_{\mathrm{rim}} \gamma (1-\Delta) = 2\pi U h_{\mathrm{rim}} \gamma (1-\Delta) \tag{5.3}$$

Dissipation will also occur at the moving contact line due to friction, as the contact line resists the movement, and it can be written as:[44, 96]

$$\dot{W}_{\mathrm{CL}} = -2\pi\, a\, \mu_{\mathrm{f}} U^2 \tag{5.4}$$

μ_{f} is a friction parameter that can vary between 0.05 and 0.1 Pa·s for substrates with $\theta_0 \approx 100°$, liquids with dynamic viscosity from 1 to 100 mPa·s, and spreading velocities U between 0.01 and 1 m/s.[96] Balancing driving and resisting contributions:

$$\Sigma \dot{W} = 0 \Rightarrow \dot{W}_{\mathrm{cap}} + \dot{W}_{\mathrm{def}} + \dot{W}_{\mathrm{CL}} = 0 \tag{5.5}$$

The viscous dissipation within the liquid is neglected. This simplification is reasonable, since the contact line velocity is of the order of few μm/s only. The unknown contact line velocity can be derived from the balance above using equations (5.1), (5.3) and (5.4):

$$U = \frac{\gamma}{\mu_f}\left(\cos\theta_{\mathrm{r}} - \cos\theta_0 + \frac{h_{\mathrm{rim}}}{a}(1-\Delta)\right) \tag{5.6}$$

Knowing that $h_{\mathrm{rim}} = \mathrm{C}\,\gamma \sin\theta_{\mathrm{r}}/E$, with C a proportionality constant described before in section 4.3, equation (5.6) can be written as:

$$U = \frac{\gamma}{\mu_f}\left(\cos\theta_{\mathrm{r}} - \cos\theta_0 + \frac{\mathrm{C}\gamma \sin\theta_r}{aE}(1-\Delta)\right) \tag{5.7}$$

Equation (5.7) was used to predict the contact line velocities of evaporating water drops during the movement of the contact line during the CCA evaporation mode on deformable substrates and to compare them to the experimental data.

5.2 Drop Evaporation Process of Water-Silica Suspension

Similar to the evaporation of pure water drops (Chapter 4), also the evaporation of drops of water-silica suspensions on soft substrate was influenced by the substrate elasticity. Figure 5-2

shows the volume of a sessile drop with initial volume ~0.72 μl with 0.0125 wt% silica particles evaporating on PDMS substrates with Young's moduli ranging from 0.02 to 1.5 MPs. This figure shows also the predicted volume of a pure water drop evaporating in CCA and CCR mode according to the equations described in section 4.1 and the initial values for volume, humidity and temperature described in the section 3.1. At least 15 drop evaporation experiments were conducted for each substrate. Data is presented in semi-log plot for clarity.

From Figure 5-2 it is possible to recognize that a water-silica suspension drop evaporates faster with decreasing the Young's modulus of the substrates. Evaporation time decreased from ~1,700 s for the hardest substrate (PDMS 10:1) down to ~1,000 s for the softest substrate (PDMS 50:1). This agrees with the predicted values for pure water drops evaporating in CCA and CCR modes, which are respectively ~1,900 s and ~1,000 s. The evaporation time of silica suspension drops can thus be fairly well predicted by using equations derived for pure water drops, as is expected for a vapor-air-diffusion limited process.

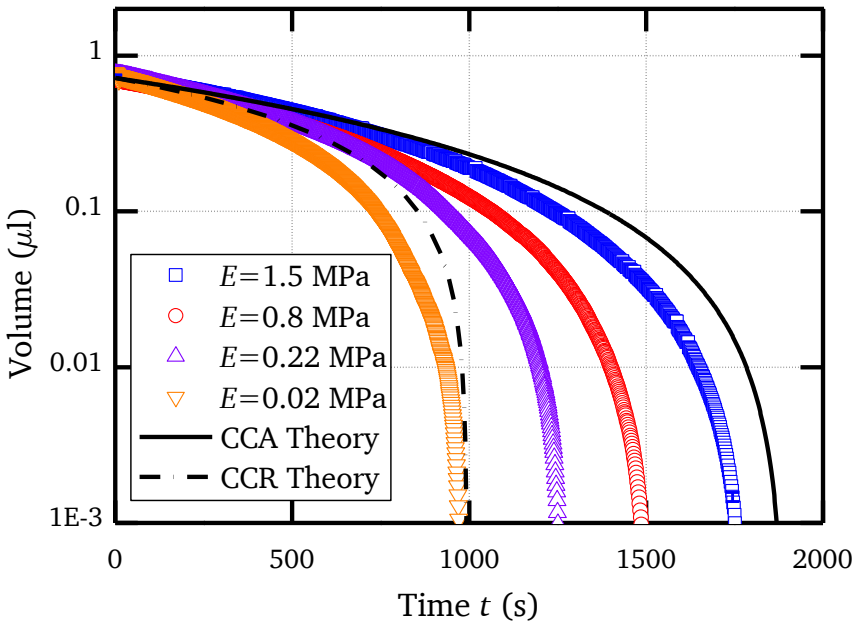

Figure 5-2: Volume of evaporating droplets of water-silica suspensions versus time. The symbols represent averaged experimental data curves on different polydimethylsiloxane (PDMS) substrates with different Young's modulus. Error bars are shown for two data points only (blue squares) and are similar for all curves. Error bars are smaller than the used symbols.

So the control of the evaporation time by substrate elasticity worked for suspensions as it did for pure liquids (Chapter 4). This can be observed in Figure 5-3 where the normalized contact

radius (with respect to the initial drop radius) is plotted versus the contact angle of evaporating droplets of silica-suspensions. This representation allows recognizing the evaporation mode; horizontal curves represent CCR evaporation and vertical curves represent CCA evaporation. All drops started with similar contact radius and contact angle after deposition (at $t = 0$). In Figure 5-3, just like for the case of pure water drops (Chapter 4), faster evaporation of drops on substrates with lower Young's modulus was caused by the prolonged pinning of the contact line, which was controlled by the substrate elasticity. This lead to a longer duration of the constant contact radius evaporation (CCR) mode and consequently to the observed shorter evaporation time for substrates with lower Young's Modulus.

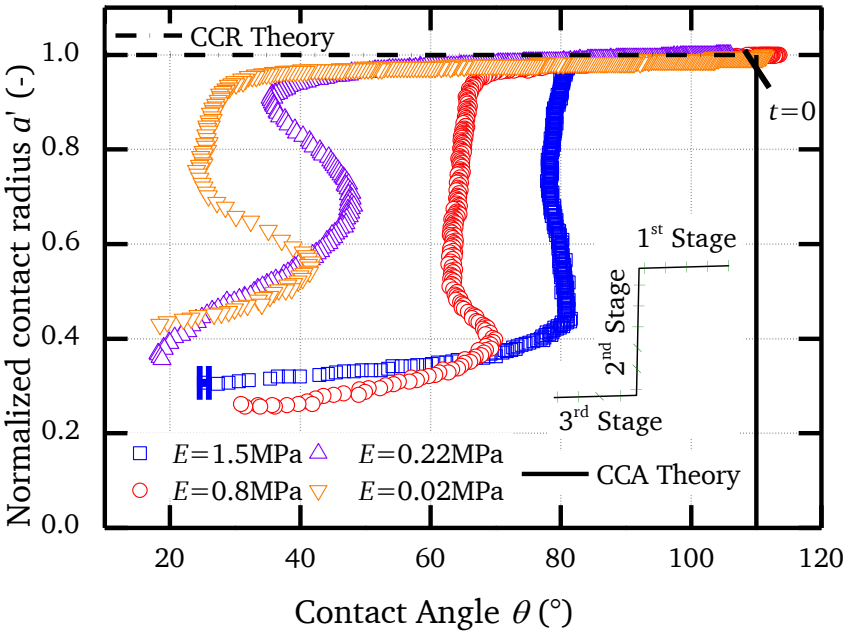

Figure 5-3: Normalized contact radius versus contact angle data of evaporating droplets of water-silica suspensions. The symbols show the experimental data on different PDMS substrates. Error bars are shown for the last data point only (blue squares) and are similar for all curves. Error bars are of the size of the symbols. A scheme is showing the 3 evaporation stages.

But, differently from pure water drops, three instead of two stages during the evaporation of silica-suspension drops were observed: (1) The first stage started when the drop was deposited on the substrate and ended when the CCR evaporation mode ended, i.e. when the receding contact angle was reached. (2) The second stage was characterized by the drop evaporating in the CCA mode. The velocity of the receding contact line was almost constant

during this stage on similar substrates. The observed increase of the contact angle during the second stage of evaporation can be explained by particle accumulation and by the viscoelasticity of the substrate. As soon as the contact line of the drop moved on the softer substrates (leaving partially particles behind), the receding contact angle of the suspension drop approached the receding contact angle for pure liquids. The viscoelastic nature of the substrate delayed the relaxation process leading to the observable increase of the contact angle in time. (3) The third and final stage of evaporation, which was nearly absent for pure water drops, was characterized by a renewed pinning of the contact line and nearly CCR evaporation, while the drop turned into a thin film and disappeared at last. Videos acquired with an inverse microscope showed particles accumulating at the drop rim during evaporation. The deposited particles were responsible for the second contact line pinning (known as self-pinning), in accordance with previous publications.[97, 98]

5.3 Contact Line Velocity is Controlled by the Substrate Elasticity

Evaporation experiments using pure water drops were performed on the same substrates used for the evaporation of water-silica suspensions in order to quantify the influence of the silica particles on the evaporation mode of the drop. Figure 5-4 shows the receding contact angles θ_r of water-silica suspensions and pure water drops depending on the Young's modulus of the substrate. The receding contact angle θ_r decreased with decreasing Young's modulus for pure water and for the water-silica suspension. For substrates with Young's modulus above or equal ~0.6 MPa there was no measurable difference on θ_r between suspension and pure water, indicating that particles had practically little influence on the first depinning of the drop. For substrates with low Young's modulus (E=0.22 MPa and E=0.02 MPa) the difference became measurable; the receding contact angles for the suspension were lower than for pure water. This lower receding contact angle for the water-silica suspension was an indicator of an extra pinning force applied on the contact line, which was already observed in previous work and occurred due to the accumulation of silica particles in this region[9, 97, 98]: more silica particles accumulate at the contact line of the drop due to the longer pinning time on soft substrates and the resultant flow towards the contact line inside the drop. Inverse microscope images just before the depinning of the contact line confirmed an increased number of particles on softer substrates.

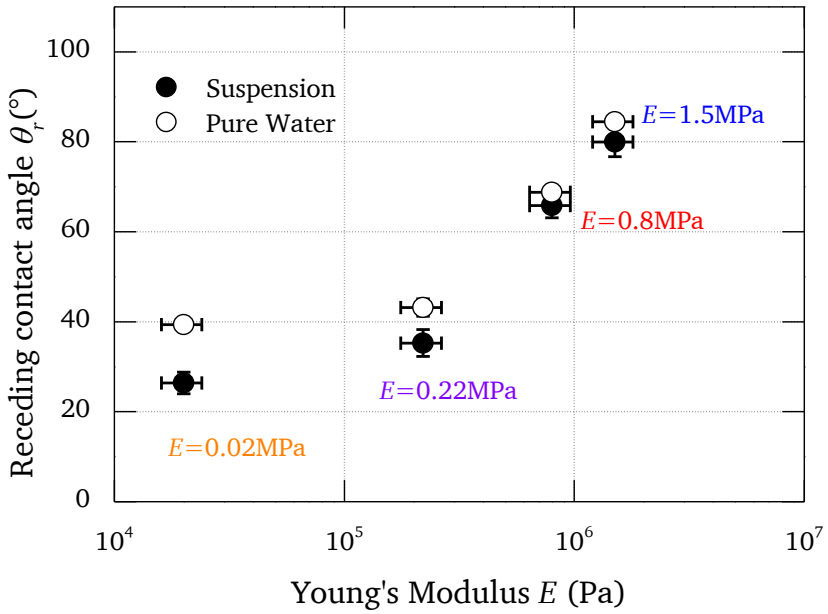

Figure 5-4: Receding contact angle versus Young's modulus of PDMS substrates. Open circles represent the measurements using pure water, filled circles for water-silica suspension.

The receding contact line velocity during the second evaporation stage of water-silica drops was nearly constant. This observation motivated the investigation of the contact line velocity (Figure 5-5). In this figure predicted, using equation (5.7), and measured contact line receding velocities of pure water and water-silica suspension drops evaporating on substrates with different Young's Modulus are plotted. The experimental error for determining Young's modulus was considered also in the error bar of the predicted velocities. As the model did not account for particles, the velocities were only calculated for pure water. Following parameters were used: equilibrium contact angle $\theta_0 = 110°$, dissipation constant $\Delta = 0.1$, as in the work by Shanahan[87], and C = 0.3 (as found in section 4.3). The friction parameter $\mu_f = 0.07$ Pa·s delivered the best fit for the contact line receding velocities on harder substrates (E=1.5 MPa and E=0.8 MPa) and is a reasonable value and is similar to values found in recent work[96] of 0.05 Pa·s for substrates with $\theta_0 \approx 100°$, dynamic viscosity of water and spreading speeds $U = 10$ cm/s. Calculated velocities deviated maximally by 5 % on harder substrates (E=1.5 MPa and E=0.8 MPa). Using the same friction parameter value, the contact line velocities were calculated on the other two substrates (E=0.22 MPa and E=0.02 MPa). Here, the calculated values underestimated the experimental values by approx. 10 %. This underestimation is explained by the fact that the friction parameter may also weakly depend on the Young's modulus of the substrate. Nonetheless, Figure 5-5 shows a very good

agreement of predicted and experimental contact line velocities. Considering the capillary energy, friction at the contact line, and deformation energy it was possible to model the decreasing contact line velocity of the drop rim with increasing Young's Modulus of the substrate. What about the contact line velocity of water-silica suspension drops?

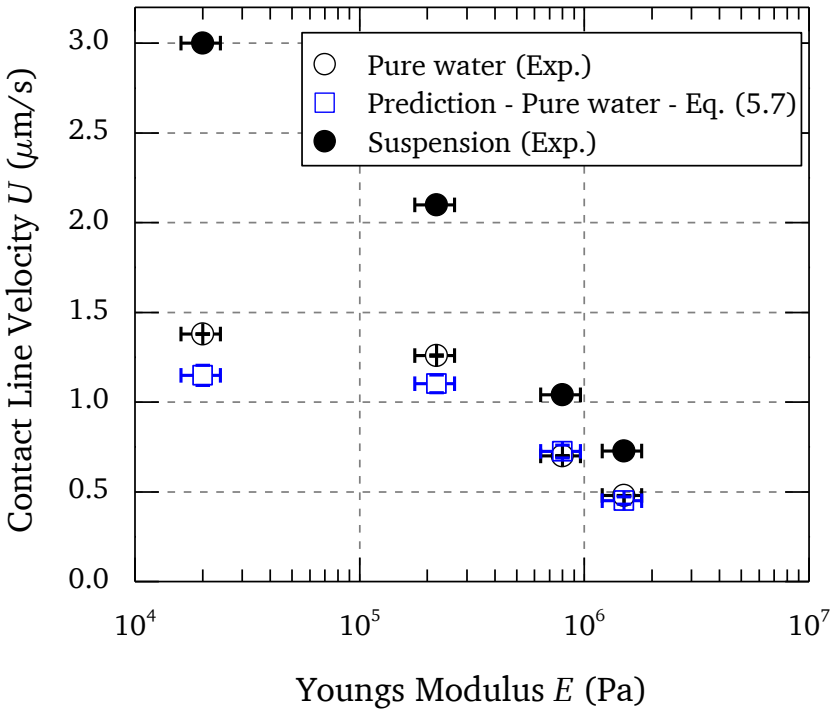

Figure 5-5: Measured contact line velocities of an evaporating drop of pure water (open circles) and water-silica suspension (filled circles) on substrates with different Young's Modulus. Predicted velocity for pure water calculated with equation (5.7) with C=0.33 and μ_f=0.07 is shown in dependency of the Young's Modulus (open squares).

The velocity U of water-silica suspension drops on harder substrates (E=1.5 MPa and E=0.8 MPa) was slightly higher (by ~0.35 μm/s) and on softer substrates (E=0.22 MPa and E=0.02 MPa) was substantially higher (by 0.8 and 2 μm/s) than the velocity of pure water drops on the same substrates (Figure 5-5). The larger velocity differences between suspension and pure water on the softer substrates must be related to the different receding contact angles between suspension and pure water drops. For example, the receding contact angle of water drops on the substrate with E=0.02 MPa was ~40° while that of suspension drops was ~26°. The smaller receding contact angle lead to an increase of the capillary force directed radially towards the center of the drop, which resulted in a higher contact line velocity upon

depinning of the drop rim. Nevertheless, the velocity U of suspension drops also increased with decreasing Young's modulus of the substrate just like observed and predicted for the case of pure water drops. Thus, it can be concluded that the velocity U for water-silica suspensions was also controlled by the Young's modulus of the substrate, just like for the experiments with pure water.

5.4 Deposition Pattern and its Relation to the Contact Line Velocity

Another interesting issue was how particles were deposited during evaporation and how substrate elasticity, which controlled the contact line velocity, influenced the deposition patterns.

Figure 5-6 presents images of the stains left after the evaporation of droplets of water-silica suspension on substrates with different Young's modulus; the black circles represent the initial radius of the drops (a_0=0.565mm). For matter of denomination the stain shall be divided in an inner and outer region. The inner region corresponds to the region where the drop was pinned for the second time, i.e. to the contact line during evaporation stage 3 (Figure 5-3). The outer region was the area between initial contact area and inner region.

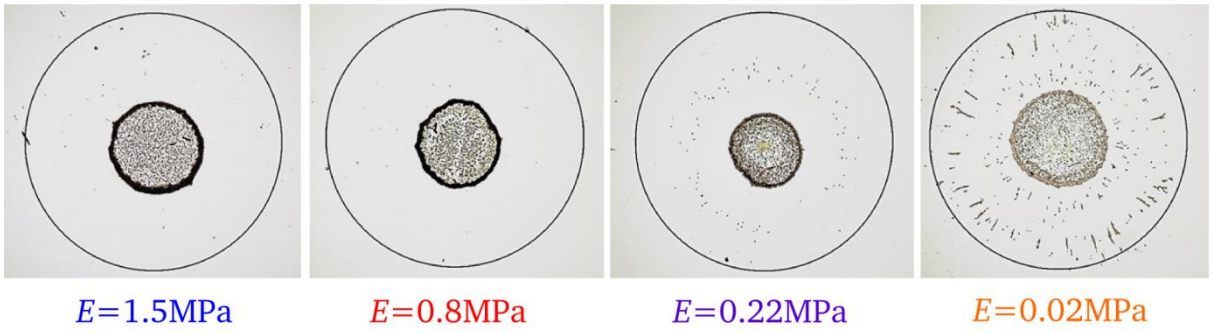

Figure 5-6: Typical stain left after the evaporation of water-silica suspension on substrates with different Young's modulus. The black circles represent the initial perimeter of the suspension drops (a_0=0.565mm). Young's Modulus of the substrates – top left: 1.5MPa, top right: 0.8MPa, bottom left: 0.22MPa and bottom right 0.02MPa.

There were nearly no particles in the outer region on the harder substrates (E=1.5 MPa and E=0.8 MPa) and particle deposition occurred mainly during the last stage of evaporation when the contact line was pinned, in agreement with previous work.[62] In contrast to the harder substrates, particles were found in the outer region on the softer substrates (E=0.22 MPa and E=0.02 MPa) and their area density increased with decreasing Young's Modulus (Figure 5-6). It was observed especially on the softest substrate (E=0.02 MPa) that particles were deposited in form of straight lines aligned towards the center of the stain.

At first the discussion shall be focused on the inner region of the stain. Particle deposits were characterized in detail after evaporation of the suspension on substrates with different Young's modulus (Figure 5-7). The mean height profiles were calculated by a self-written Matlab script from white-light confocal profilometer measurements (thick line) and were plotted versus the radial coordinate. The standard deviation of the mean height profiles is represented by the hashed area enclosed within thick and thin lines. Like in previous works on coffee-staining[9], a crater-like deposit in the inner region with more particles at the rim than in the center of the stain was observed. The maximum height of the deposit was located at a distance between 140 and 160 μm from the center of the stain. This distance did not depend on the substrate elasticity, in contrast to the maximum height of the stain, which decreased with decreasing Young's modulus of the substrate.

Moreover, the ratio between the maximum deposit height and the deposit height in the center of the stain, a parameter for characterizing the degree of coffee-staining, decreased from 5.6 to 2.9 with decreasing Young's modulus of the substrate. Substrate elasticity thus appears to be a material parameter that can control (enhance/reduce) the coffee-stain effect to some extent. To understand how the deposits were formed further investigations were performed using an inverse microscope.

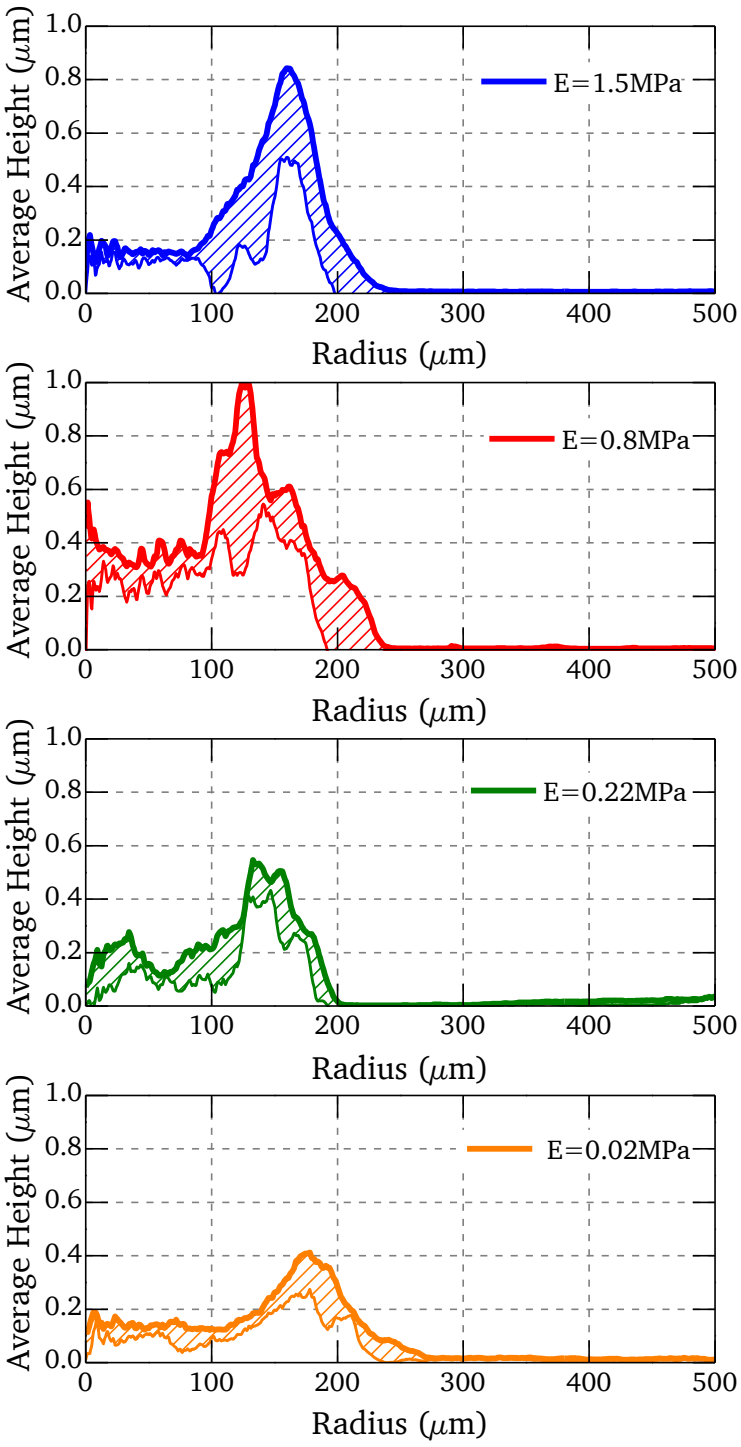

Figure 5-7: Average height profile of the silica deposits after the evaporation of water on substrates with different Young's modulus. Thick lines are mean values; thin lines represent the standard deviation subtracted from the mean value. The region in-between curves is hashed for clarity of representation. Decreasing the Young's modulus reduced the coffee-stain effect.

Videos acquired with the inverse microscope showed that the deposition in the inner region occurred in the last moments of drop evaporation ($t < 2$ s), leaving no time for re-adjustments in the distribution of the particles inside the drop. Thus, the stain pattern depended mainly on how particles were distributed just before the beginning of the third and final stage of evaporation and did nearly not change during the last seconds of evaporation. This is an observation in contrast to some other works on the evaporation of suspensions: when CCR evaporation mode dominates, a big mobility of the particles is usually observed at the end of evaporation when the liquid flow towards the contact line rapidly increased.[62, 99, 100] But, differently than observed previously, in the experiments with controllable evaporation mode particles accumulated at the contact line as the contact line receded (during CCA evaporation mode). Figure 5-8 shows this process of accumulation of particles during the second evaporation stage.

The first image shows the drop at the beginning of the second stage of evaporation. Particles were distributed fairly homogenously in the drop and only a few particles accumulated close to the contact line due to the internal flow caused by the enhanced evaporation flux at the contact line, as described by Deegan et al.[9] The subsequent images show how more and more particles were dragged by and accumulated at the drop rim due to the receding contact line. This is indicated also in the schematic representation in the right side of Figure 5-8. Note that the distribution of particles in the bulk of the drop remained homogeneous during this process. It is thus to conclude that the accumulation of particles due to the movement of the contact line was a main step in the formation of the stain profile during the evaporation. For explaining the different maximal deposit heights observed in the experiments it is necessary to consider the outer region of the stain, which was formed during the second stage of evaporation.

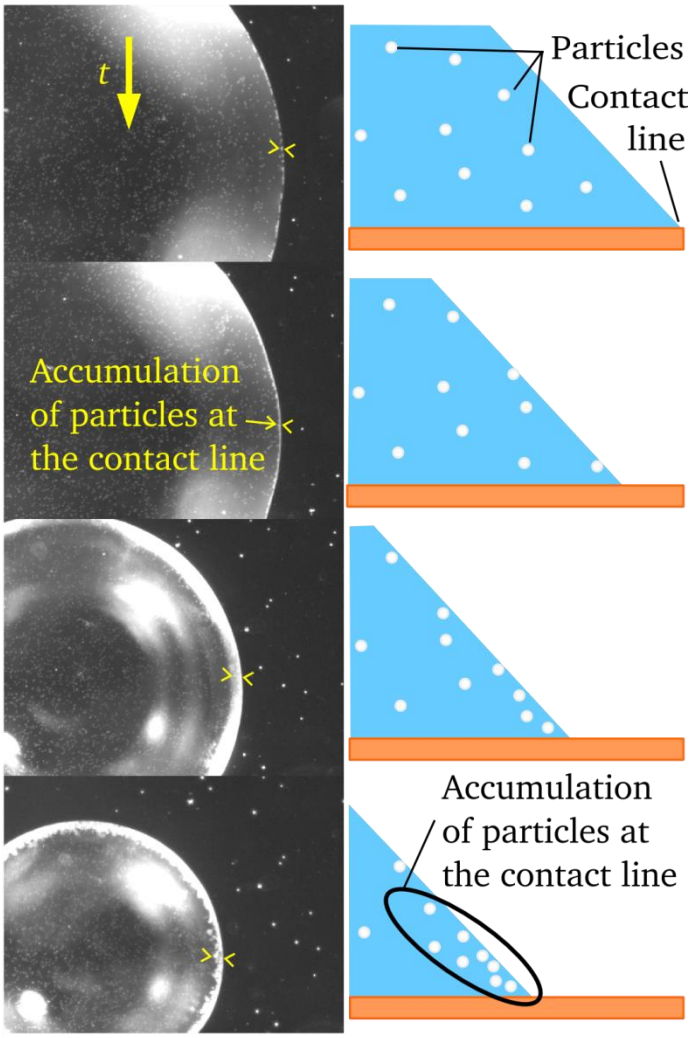

Figure 5-8: Left: image sequence showing the accumulation of particles at the contact line during stage 2 evaporation of a water-silica suspension drop on a harder PDMS substrate (E=1.5 MPa). Right: schematic representation of the left image showing the accumulation of particles.

As shown in Figure 5-6, the softer the substrate was, the more particles were deposited in the outer region. Figure 5-9 presents a sequence of images of the receding contact line during the evaporation of the water-silica suspensions on harder (E=1.5 MPa) and softer (E=0.02 MPa) substrates. On harder substrates no deposits were left behind during the passing of the contact line. This was also observed in previous publications for the system silica particles and silicon wafer, when the attraction between particles and substrate was weakened by electrostatics.[101] On the other hand, for softer substrates particles or agglomerates of particles were deposited during contact line retraction. Two parameters seemed responsible

for the deposition of the particles on the softer substrate: the contact angle of the droplet and the contact line velocity.

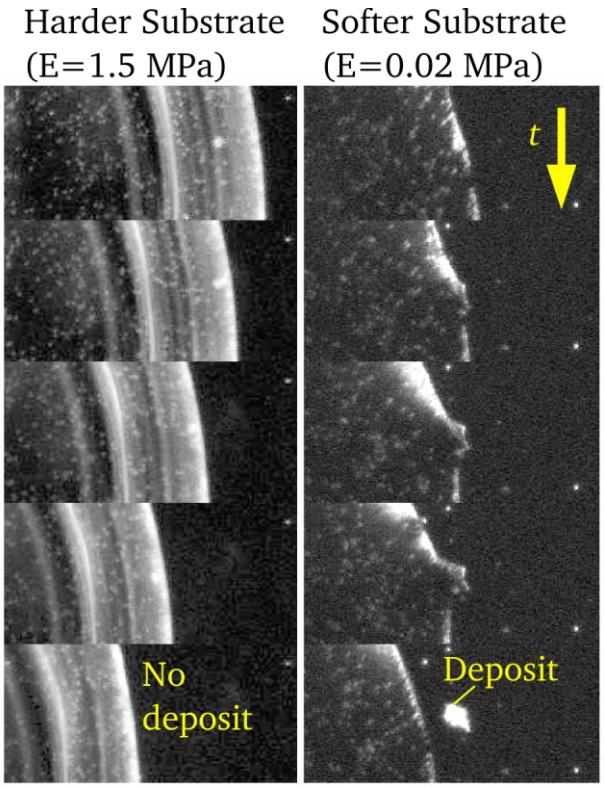

Figure 5-9: Sequence of images acquired with an inverse microscope showing the contact line of a water-silica suspension during the stage 2 evaporation (CCA mode) on harder (E=1.5 MPa) and softer (E=0.02 MPa) substrates, respectively. On the harder substrate the contact line dragged along the particles leaving no deposit behind; a deposit of particles was left behind on the softer substrate.

The evaporative flux of water (see section 2.2.3) is highest at the rim of pinned droplets, and inversely proportional to the contact angle of the drop.[14, 34, 53] So, the smaller contact angles on softer substrates increase the evaporative flux at the contact line, increasing also the fluid flow towards the drop rim and facilitating the deposition of particles.

The contact line velocity also controls the deposition process, as is known from dip-coating processes. During dip-coating, a substrate is extracted with a constant speed from a liquid bath containing suspended particles. A thin liquid film is formed on the substrate due to the interplay of viscosity of the liquid and interfacial forces. Contact line velocities range from

0.1 μm/s up to 100 mm/s[101, 102] and are comparable to the contact line velocities of the drop evaporation experiments, which were between 0.5 and 3 μm/s.

The velocity of the substrate during dip-coating, which corresponds to the contact line velocity, plays a major role on the thickness of the liquid film and so on the amount of particles deposited on the substrate. The higher the contact line velocity U is, the more particles are deposited on the substrate.[103] The Landau-Levich equation can predict the thickness of a liquid film when a substrate is withdrawn from a liquid bath: $h_\infty = 0.946\sqrt{\gamma/\rho g}\,\mathrm{Ca}^{2/3}$, with the capillary number $\mathrm{Ca} = \eta U/\gamma$.

The thickness h_∞ of the water film when a surface is withdrawn with velocities U in the range of experimental drop velocities is shown in Table 5-1. In this case, h_∞ was smaller than the diameter of the silica particles (2μm) up to a velocity $U \sim 1.5\,\mu$m/s. Thus, the receding contact line would collect all particles and leave no behind. For higher withdraw velocities h_∞ increased beyond the silica particle diameter. Thus, some particles could be dragged inside the film and the receding contact line would not be able to collect all particles. Consequently, some were left behind.

Table 5-1: Film thickness h_∞ predicted with the Landau-Levich equation for velocities in the range of the contact line velocities in the water-silica suspension drop evaporation experiments.

Contact line velocity U (μm/s)	**Film thickness h_∞ (μm)**
0.5	0.93
1	1.48
1.5	**1.94**
2	2.35
2.5	2.73
3	3.08

When the contact line velocity U was higher than 1.5 μm/s in the drop evaporation experiments, particles were deposited in the outer region. For smaller receding velocities the contact line collected all particles leaving no deposit behind. This was checked using particles with a larger diameter (5 μm instead of 2 μm) and indeed no deposits were observed on either of the outer regions of surfaces. For the softest substrate (E=0.02 MPa), e.g., it was found $U \approx 1.6\,\mu$m/s and $\theta_\mathrm{r} \approx 40°$. It is thus to conclude that contact line velocity controlled

the deposition of particles during stage 2 of evaporation. This way, the decrease of maximal deposit heights with decreasing Young's modulus of the substrates could be explained: On softer substrates the receding contact line velocity was higher, the Landau-Levich film was thicker, more particles could slip into this film and were eventually left behind as the contact line moved on. At the end, fewer particles were accumulated at the contact line of the drop as the third and final evaporation stage started.

5.5 Conclusion

The deposition pattern resulting from the evaporation of drops of water-silica suspensions could be modified to some extent by the elasticity of the substrate. In fact, the evaporation modes of drops of a suspension can be controlled by tuning the elasticity of the substrate, analogue to the case of water (Chapter 4). Considering capillary forces, viscoelastic dissipation, and contact line friction a model to calculate the contact line velocity of pure water drops during evaporation with constant contact angle was introduced. This model predicted an increase of the contact line velocity upon a decrease of the elasticity (Young's modulus) of the substrate, which was confirmed with experimental results. Contact angle and contact line velocity, analogue to the dip-coating process, controlled the thickness of the liquid film (Landau-Levich film) trailing behind the rim of the receding drop. Solid particles smaller than the thickness of the Landau-Levich film became trapped within the film as the contact line receded and were more likely to be deposited during the CCA evaporation mode. Particles larger than the thickness of the film moved together with the contact line and were accumulated until the contact line was pinned. The relation between contact line velocity and particle accumulation is a novelty introduced in drop evaporation research and could help to better control the coffee-stain effect. Substrate elasticity can thus be used to control the deposition of particles even when a drop is evaporating with a moving contact line.

6 Influence of the Substrate Thermal Properties on Sessile Drop Evaporation[5]

In the last few years, some scientific works were devoted to the development of mathematical and numerical models describing drop evaporation (see section 2.2). Hu and Larson focused their work on the analytical description of the internal flow in a drop, with and without Marangoni convection.[53, 55] Other researchers used numerical methods and experiments to investigate and describe different phenomena: contact line dynamics during the evaporation process[104, 105], substrate deformation due to interfacial forces[49] and contact angle hysteresis.[106] Recent works on drop evaporation improved the previous models accounting for the heat conduction in the substrate.[36, 38] Nevertheless, in these works it is assumed that the temperature fields in the substrate and in the droplet, as well as the vapor concentration field in the gas phase are quasi-stationary. To justify these assumptions, the authors showed that the characteristic time of heat conduction (or vapor diffusion), based on the characteristic size and the thermal diffusivity (or vapor diffusion coefficient) was much smaller than the total evaporation time.

However, the above assumption does not hold for the case where the heat transfer coefficient between the back side of the substrate (opposite to the droplet) and the ambient gas is very low, which is typical for free convection. In the limiting case, when substrates are well insulated from the surroundings, the temperature at long times decreased uniformly and linearly with time.[107] Moreover, the temperature field in the steady state was determined alone by the thermal conductivities of the involved phases. The influence of thermal effusivity on the droplet dynamics reported in [37] was a clear indication of the effect of transient heat conduction on the drop evaporation.

In this chapter, experimental results on investigations of the influence of thermal properties (thermal conductivity and diffusivity) of the substrate on drop evaporation is presented. For this purpose, substrates with different thermal properties (soda-lime glass and silicon substrates) but very similar wettability (by grafting a thin polymer layer) were fabricated, so that the evaporation mode was similar (see section 3.5). Thermal conductivity should influence the temperature profile of the substrate and control the heat transport from the substrate to the sessile drop. Thermal diffusivity of the substrate should play a larger role if a

[5] This chapter is based on the publication "M. C. Lopes, E. Bonaccurso, T. Gambaryan-Roisman, P. Stephan, *Influence of the substrate thermal properties on sessile droplet evaporation: Effect of transient heat transport*, Colloids and Surfaces A: Physicochemical and Engineering Aspects, **432**, 64-70, (2013)".

limited amount of heat is available in the substrate, e.g. if the substrate is very thin (comparable to the size of the drop) and is thermally insulated from the ambient. To access the temperature field inside the substrate and better understand the effects of specific thermal properties of the substrate material on the evaporation process, collaboration partners[6] developed a numerical model for transient heat conduction in the substrate and in the droplet, as well as the diffusion of water vapor in the gas phase (Section 3.8.2). The model enables the comparison of numerical calculations to the experimental data, and also to perform a parameter analysis regarding the thermal properties of the substrate.

6.1 Experimental Investigation of the Thermal Conductivity of the Substrate

Water drop evaporation experiments were performed on glass and silicon substrates covered with a grafted film of polystyrene (further details in section 3.5). The substrates were supported physically by minimizing the contact area at the edges, in order to minimize heat transport from the substrate to the support and the surroundings. Three series of experiments with three different initial drop volumes of 0.2, 0.4, and 0.6 μl on both substrates were performed. At least 10 experiments were performed on every substrate. The initial contact angle of water was similar for all drop sizes (82° ±3°). This was due to the similar polystyrene coating on silicon and glass, which maintained surface chemistry and wettability of the different surfaces practically identical.

Figure 6-1 presents the contact radius a of the evaporating drop versus the contact angle θ. CCR and CCA evaporation modes are indicated by the horizontal and vertical lines, respectively. All drops evaporated with a similar mode despite the different thermal properties of the substrate. For a short time after deposition, varying between 10 and 40 s, the drops evaporated in CCR mode. When the contact angle reached the receding contact angle, which for water on both substrates was approximately 80°, CCA evaporation started. Towards the end of the evaporation drops evaporated in a mixed mode: the contact angle started again to decrease markedly while the contact radius decreased only slightly. The used surfaces allowed very similar evaporation modes, and therefore relevant parameters for evaporation such as contact radius and contact angle of the drops remained similar during the entire evaporation

[6] Tatiana Gambaryan-Roisman and Peter Stephan from the Institute of Technical Thermodynamics, Technische Universität Darmstadt

process. Any observable differences in the evaporation time between drops of the same initial size can thus only be attributed to the different thermal properties of the substrates.

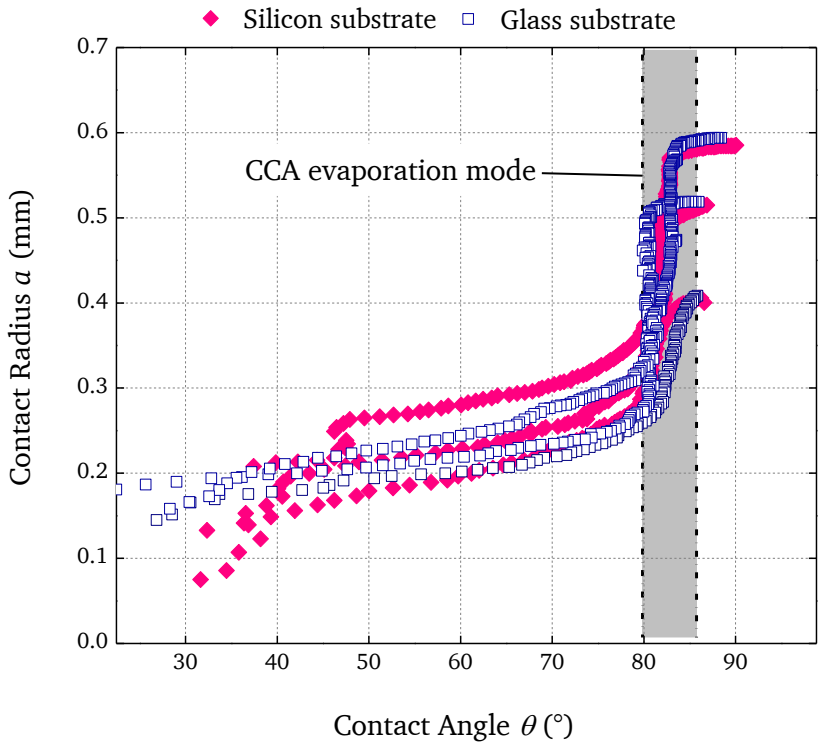

Figure 6-1: Contact radius versus contact angle curves for the three series of evaporation measurements.

Drop volume over time for the same experiments as in Figure 6-1 is shown in Figure 6-2. The grey areas represent the experimental standard deviation. As expected, the smallest drops evaporated in the shortest time and larger drops took longer to evaporate. Moreover, drops on silicon substrates evaporated much faster than those on glass substrates. In all cases, the total evaporation times differed by more than 10 %. Evaporation was faster on the substrate with higher thermal conductivity because thermal energy could be transported faster to the liquid, allowing a higher air-liquid interface temperature and as result increasing diffusive flux of water molecules into air.

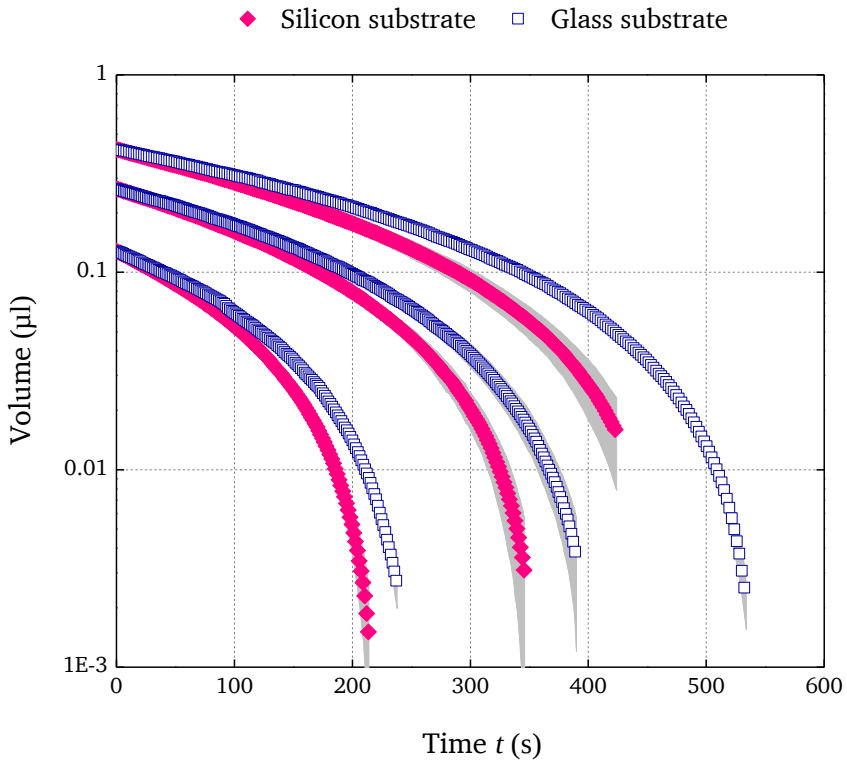

Figure 6-2: Drop volume versus evaporation time curves for three series of evaporation measurements with different initial water drop volumes on polystyrene coated glass and silicon substrates. (same experiments as in Figure 6-1).

In accordance to previous works,[35-37] the experiments showed the importance of the thermal conductivity for the evaporation of water drops. Furthermore, the ratio between evaporation times of drops on glass and on silicon ($t_{\mathrm{evap}}^{\mathrm{gs}}/t_{\mathrm{evap}}^{\mathrm{si}}$) increased from 1.13 to 1.17 with increasing initial drop volume. This means that with increasing initial volume the relative difference on evaporation time increased. The larger the initial drop, the stronger thermal conductivity will influence the evaporation time. Numerical investigations showed that this difference could be related to the different development of the temperature field inside the substrate.

The temperature calculated numerically in the glass substrate just below the drop was up to 2 °C colder than for the silicon substrate (see Figure 6-3). For both substrates it was assumed that the decrease of substrate temperature continued until total evaporation or until the substrate was cooled down to dew temperature and condensation heat stabilizes the temperature. Thus, the influence of the thermal conductivity was more pronounced for larger

initial volume of the evaporating drop due to the constant decrease of the temperature at the liquid-air interface, which was more pronounced in less heat conductive materials. On the silicon substrate, the temperature on the contact area of the drop decreased monotonously with time. For the case of the glass substrate an increase of the temperature on the contact area at the end of the evaporation process could be shown. This happened as the drop became very small and evaporation rate decreased leading to a lower cooling power. The substrate was then able to supply enough thermal energy to rise the temperature of the drop.

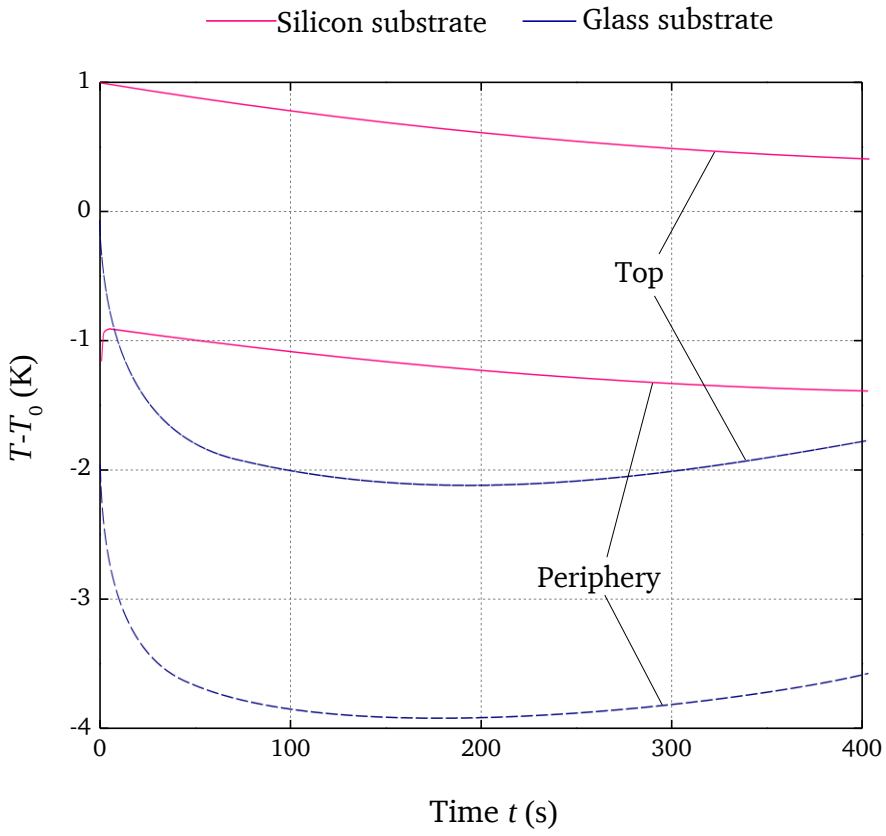

Figure 6-3: Temperature of the liquid-gas interface during the evaporation of a water drop on a silicon and a glass substrate at two locations: top and periphery of the drop.[108]

6.2 Comparison to Numerical Results and Investigation of the Thermal Diffusivity

Figure 6-4 presents the volume of experimental evaporating drops on both glass and silicon substrates together with the numerical prediction provided by the collaborators Gambaryan-Roisman and Stephan (details on boundary conditions can be found in section 3.8.2).[108]

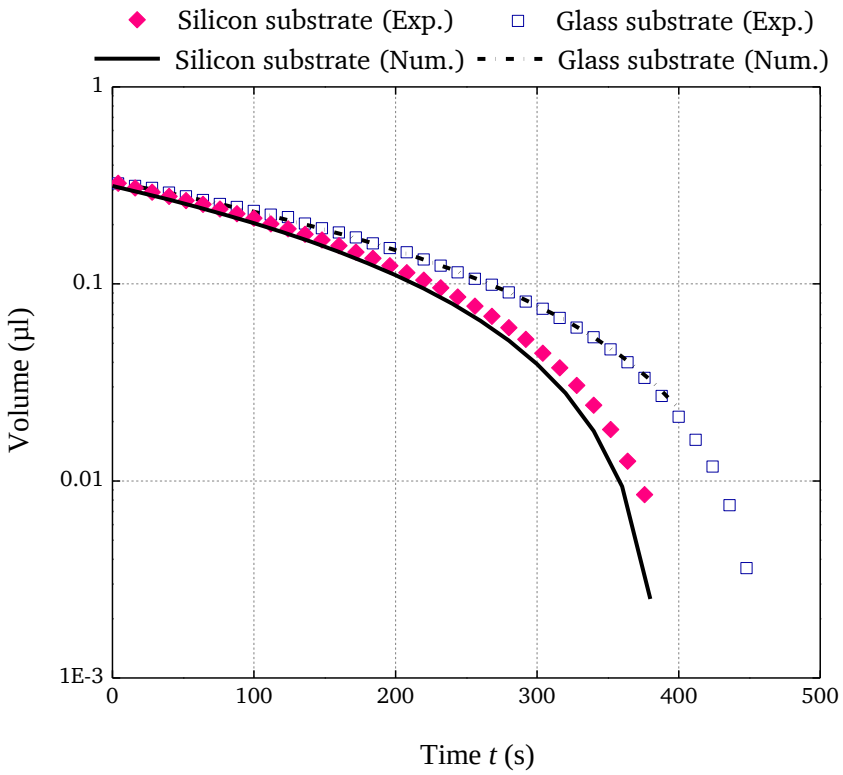

Figure 6-4: Volume of evaporating drops over time on substrates with different thermal properties but similar wettability. Experimental data on silicon and glass substrates are represented respectively by filled diamonds and open squares. Numerical predictions for silicon and glass substrates are represented respectively by solid line and dash-dotted line.

Simulation parameters were set to reproduce the experimental conditions (Table 6-1). Initial temperature is equal to 20 °C and it is assumed that the air at the domain boundaries is dry. Properties for the water at the specified temperature have been taken from the reference book.[109] Figure 6-4 shows the direct comparison of drop volume from the numerical simulation and from experiments. The initial time ($t = 0$) corresponded to the start of the CCA evaporation mode in experiments. Numerical simulations described well the evolution of the drop volume for both substrates. Moreover, simulations enabled the investigation of the temperature field inside the substrates during drop evaporation.

Table 6-1: Thermal parameters used to simulate the drop evaporation on silicon and glass substrates coated with a thin polystyrene film.

Substrate thickness h_{sub}	**Thermal conductivity k_{sub} (W/m·K)**		**Thermal diffusivity α_{sub} (m^2/s)**	
	Silicon	Glass	Silicon	Glass
$5x10^{-4}$ m	139.4	1.05	$8.0x10^{-5}$	$5.8x10^{-7}$

Figure 6-5 and Figure 6-6 show the radial temperature profile calculated by numerical simulations for the bottom surface of glass (Figure 6-5) and silicon (Figure 6-6) substrates during the course of evaporation.

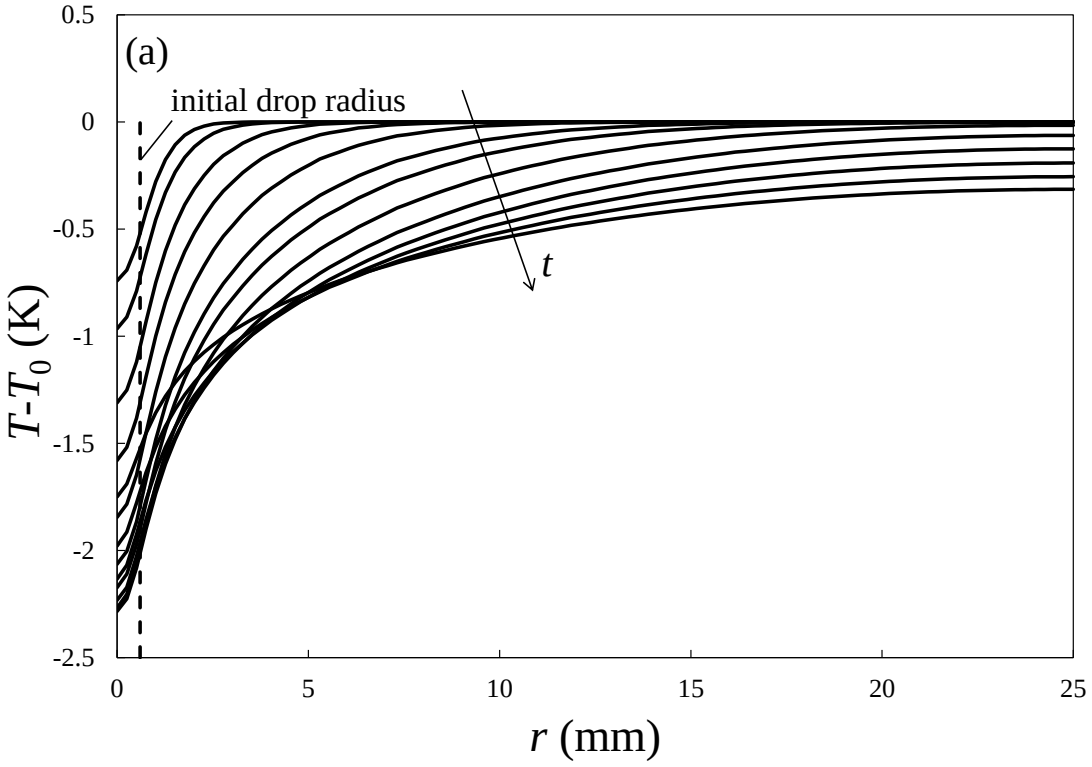

Figure 6-5: Temperature distribution from numerical simulations for different times (between 1 and 400 s) at the bottom of the glass substrate. [108]

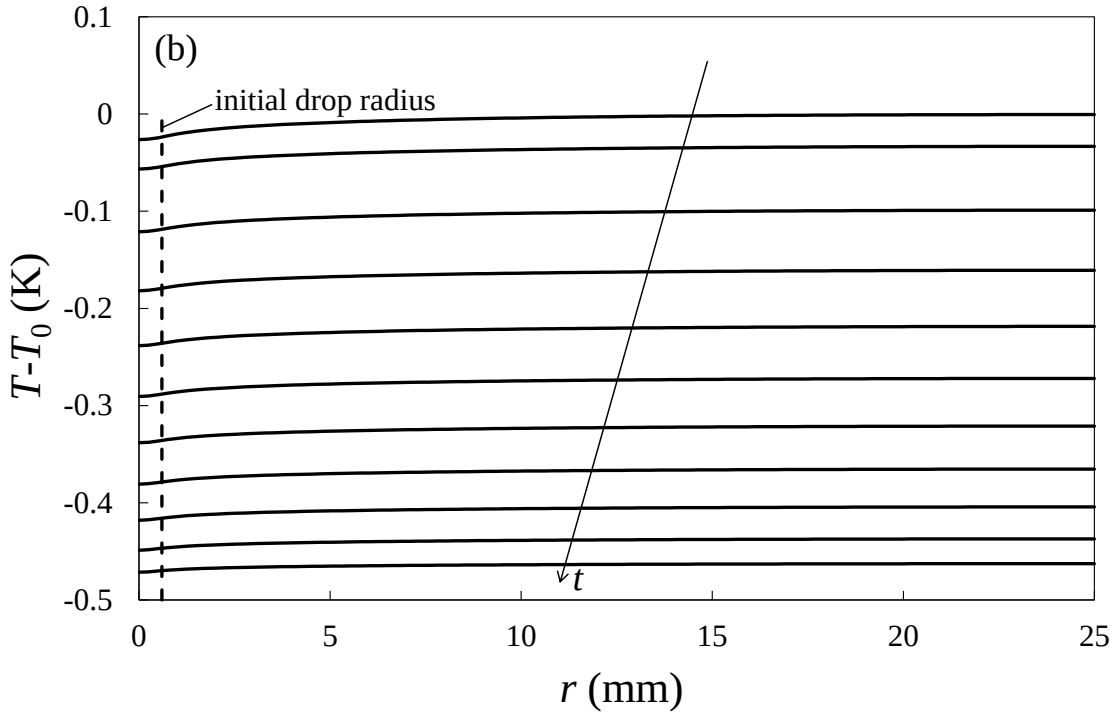

Figure 6-6: Temperature distribution from numerical simulations for different times (between 1 and 400 s) at the bottom of the silicon substrate.[108]

For the silicon substrate the temperature was radially homogenous due to the high thermal conductivity of the substrate. The radially homogenous temperature distribution indicates a quasi-steady thermal process. Collaborators found that the rate of temperature decrease was proportional to the evaporation rate and inversely proportional to the total heat capacity of the system.[108] In the case of the glass substrate, the temperature difference in radial direction was more pronounced and therefore, the longer the evaporation lasted, the colder the liquid-air interface would become.

A simulation of two additional imaginary materials (material A and B) was performed by collaborators in order to show the role of different thermal properties on drop evaporation (Figure 6-7). Material A has the same thermal conductivity as silicon and the same thermal effusivity as glass, and material B has the same thermal conductivity as glass and the same thermal effusivity as silicon. As shown in Figure 6-7, drop evaporation was slowest on material A and fastest on Material B and silicon.

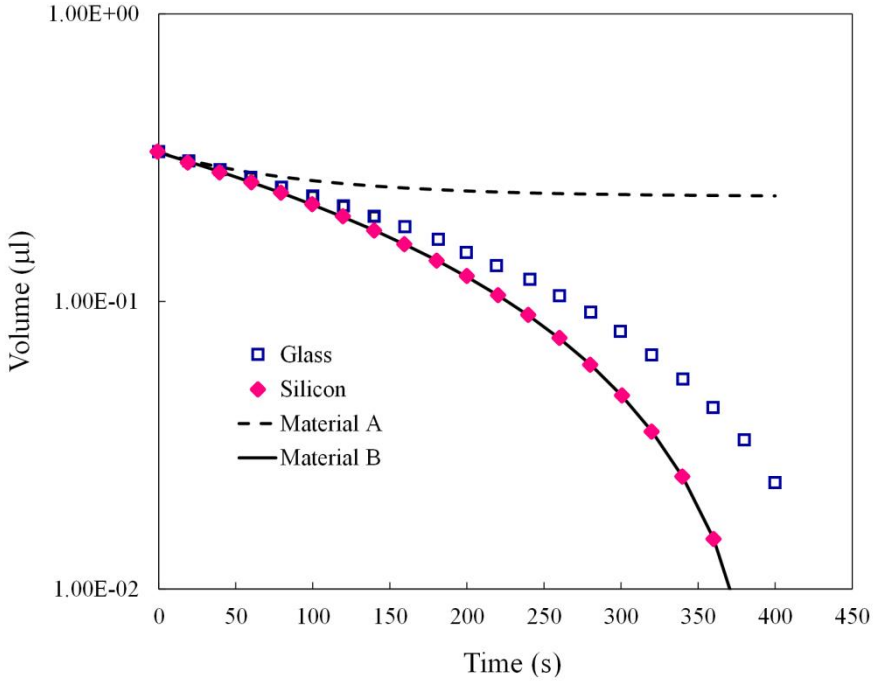

Figure 6-7: Numerical prediction of the volume of evaporating drops over time for different substrates. Numerical predictions for substrates of glass, silicon, material A and material B are represented respectively by open squares, solid diamonds, dashed and solid line. Material (A / B) has the same thermal conductivity as (silicon / glass) and same effusivity as (glass / silicon).[108]

Table 6-2: Thermal parameters used to simulate the drop evaporation for the imaginary materials A and B.

	Thermal conductivity k_{sub} (W/m·K)	**Thermal diffusivity α_{sub} (m^2/s)**	**Thermal effusivity e, ($W \cdot s^{1/2}/m^2 \cdot K$)**
Material A	139.4	1.02×10^{-2}	1.38×10^{3}
Material B	1.05	4.54×10^{-9}	1.56×10^{4}

The slow evaporation on material A can be explained by the relative high thermal diffusivity: a quasi-steady temperature distribution was reached very fast compared to other materials. Material A was cooled the fastest and the most, influencing the evaporation time dramatically. It is to expect that in this case vapor condensation on the substrate may play an important role. Numerical results showed for the case of material B a very similar drop evaporation development as for the silicon substrate. As both materials have similar effusivity, this confirms the experimental observations reported in the work by Sobac et al.[37]

6.3 Comment on the Relation of Wettability and Liquid Load

Evaporation time does not only depend on the thermal properties of the substrate, but also on the amount of liquid on it. The idea to investigate the relation of wettability and liquid load appeared with the question: why do plastic dishes not always dry completely in the dishwashing machines? One of the reasons for the different drying of plastic and glass (or metal) lies in the different thermal properties. As described in previous sections 6.1 and 6.2, thermal conductivity leads to different heat fluxes from substrate to drop, leading to different liquid-gas interfacial temperatures. The other reason could be the different liquid load on the substrates after the washing cycle. As described in section 2.1, wettability controls how water wets the substrate, i.e. if it forms a drop with a spherical cap shape and thus with a defined contact angle with the substrate (poor wettability, hydrophobic surface), or if it forms a thin continuous film on the substrate (good wettability, hydrophilic surface). In this case, wettability of the substrate influences the total amount of liquid trapped on the surface.

In order to investigate the liquid load of substrates in dependency of their wettability a special set-up was developed by the bachelor student Angelika Sell.[73] The weight of substrates (hold perpendicular to the ground) was measured while water was sprayed onto them (see section 3.3). Poly(methyl methacrylate) substrates (PMMA Folie Farblos, Evonik, Essen, Germany) with a dimension of 25x25x0.5 mm were treated differently to attain different surface wettability with water. Teflon (AF 1601 sol fc 100ml 6%, DU PONT, Wilmington, USA) was used to make a hydrophobic coating on the PMMA sample allowing water to reach a contact angle of $\theta_0^{H_2O} = 120°$. Plasma treatment (Zepto B, Diener electronic, Ebhausen, Germany) with air at 0.3 mbar and 100 W power for 80 s/ 60 s was used to obtain PMMA substrates with contact angles $\theta_0^{H_2O} = 60°/\ 10°$.

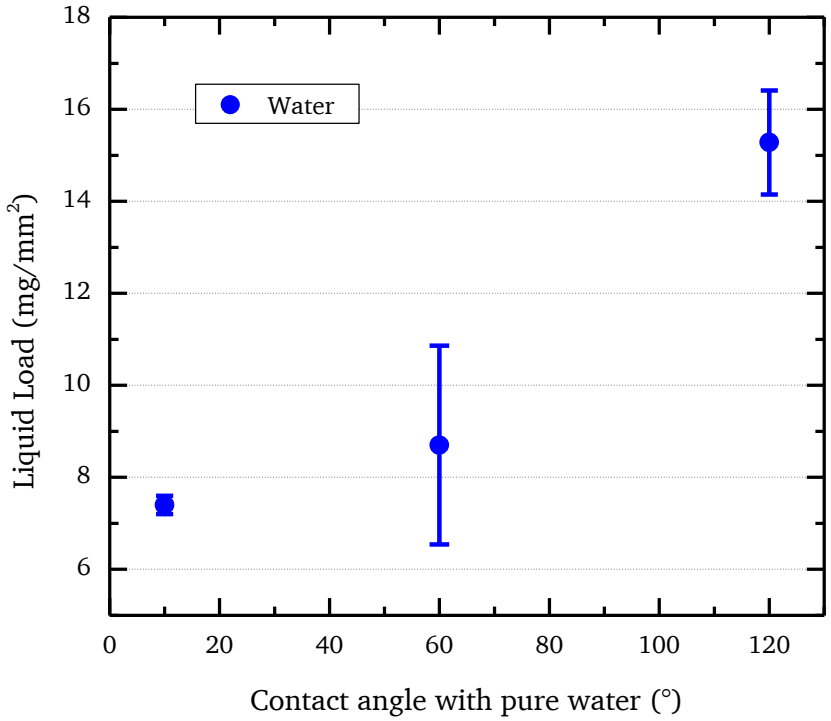

Figure 6-8: Water load measured with a microbalance on differently treated PMMA substrates after spraying the surface with water for at least 60 s. PMMA substrates had a contact angle $\theta_0^{H_2O}$ of 10°, 60° and 120°.

Figure 6-8 shows the measured liquid load of the samples in dependency of the contact angle with water $\theta_0^{H_2O}$. With increasing hydrophobicity (contact angle of water with the substrate increases from 10° to 120°), the amount of liquid load increased from around 7 mg/mm^2 to around 15 mg/mm^2. For the hydrophobic substrate many droplets were observed on the substrate, while for hydrophilic substrate a thin water film was formed.

Further measurements were performed using 1 vol.% solutions of a regular rinse agent (Priva, Netto, Maxhütte-Haidhof, Germany) and the trisiloxane surfactant S233 (Break-Thru 233, Evonik Industries, Essen, Germany) on the most hydrophobic PMMA substrate. Experimental results of the liquid load are presented. The addition of rinse agent or surfactant to the water caused a decrease of the accumulated liquid load on the substrate (Figure 6-9). The observed decrease of liquid load is related to the decreased surface tension of water, enhancing the formation of a liquid film. It is thus to conclude that with decreasing substrates hydrophobicity less water is accumulated on a sprayed surface, and the drying of the surface is faster.

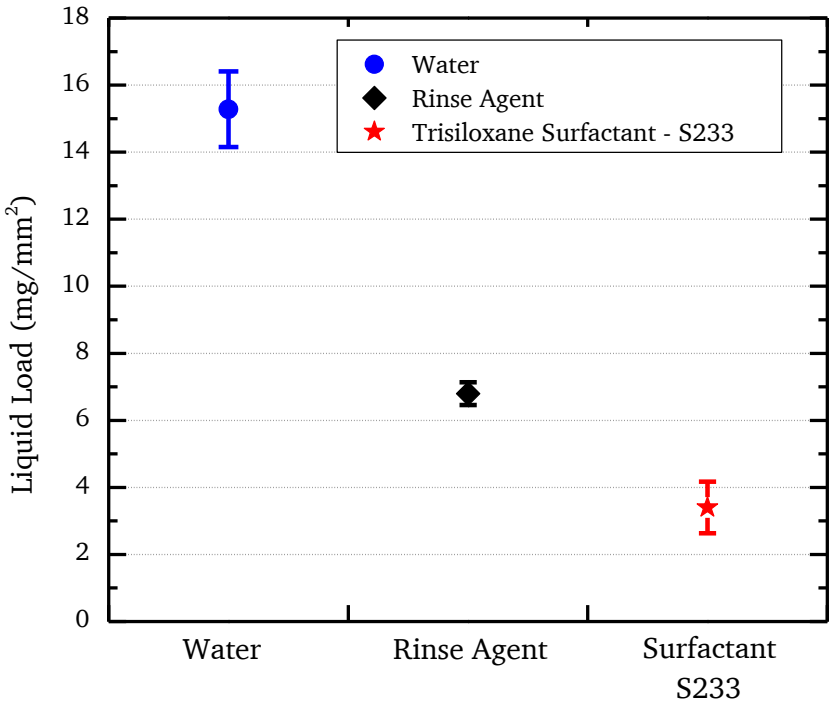

Figure 6-9: Liquid load measured with a microbalance on hydrophobic PMMA substrates ($\theta_0^{H_2O}$ =120°) after spraying the surface with different liquids for at least 60 s. Circles, diamonds and stars represent respectively the experimental data for pure water, a solution of rinse agent in water and a solution of S233 in water.

6.4 Conclusion

The effect of thermal properties (thermal conductivity and diffsuivity) of substrates was investigated on the overall evaporation time of water drops placed on them. Two different substrates (glass and silicon) were used, onto which a layer of polystyrene was grafted for ensuring the same wettability, while the thermal conductivity of both materials was different. Goal of the performed experiments was to investigate the influence of thermal conductivity and diffusivity on drop evaporation. From the presented experiments it is to conclude that the higher thermal conductivity of silicon accelerated drop evaporation by more than 10 %. A numerical model describing transient heat conduction in the droplet and in the substrate as well as diffusion in the gas was developed by collaborators. It was shown that the transient heat transport governed the evolution of local temperature distribution at the liquid-gas interface, and therefore the evaporation rate. As expected, thermal diffusivity must be taken into account to correctly describe the temperature development of the substrate. Beyond the

thermal properties of the substrate, the wettability of the substrate was investigated in order to understand its influence on the liquid load accumulated on a sprayed substrate, which consequentially affects also the overall drying time of a wet substrate. Hydrophilic substrates accumulated less liquid mass, as the liquid formed a thin film that drained easier from the substrate. Spraying surfactant solutions instead of pure water also decreased the accumulated liquid on the substrate, as the surfactant solution formed thin films also in hydrophobic substrates.

7 Summary and Conclusions

The new results presented in this work contribute to better understand the process of drop evaporation and how it is influenced by substrate's properties like elasticity (Young's modulus), thermal properties, and wettability. Deposit patterns from the evaporation of water-silica suspension drops was also investigated, and it was possible to explain how they are affected as well by substrate's properties.

Chapter 4 presents a novel method to control drop evaporation using soft substrates made of polydimethylsiloxane (PDMS) with tunable elasticity. As shown in previous work, a sessile liquid drop deformed a soft substrate by capillary forces.[24] Experiments presented in this work (section 4.2) using PDMS substrates with similar wettability, but different elasticity, showed that water drops on softer PDMS (Young's modulus of 0.02 MPa) evaporated faster than those on harder PDMS (Young's modulus of 1.5 MPa). The faster evaporation on softer substrates was related to a different dynamic evolution of the receding contact angle of the drop, which was a direct consequence of the substrate deformation close to the triple-phase contact line (section 4.3). A simple model to predict the change of the receding contact angle in dependence of the Young's modulus and maximal deformation height was developed. Experimental data agreed very well with calculated receding contact angles of water drops on PDMS substrates. Moreover, by fine-tuning the substrate elasticity (Young's modulus) of PDMS it is possible to control the transition between constant contact radius and constant contact angle evaporation modes. It was finally demonstrated that evaporation mode and, consequently, evaporation time of sessile drops can be controlled by appropriately choosing the elasticity of a substrate (Young's modulus).

Chapter 5 presents the investigation on the influence of soft PDMS substrates on particle deposition patterns during the evaporation of water-silica suspension drops. It is shown in section 5.3 that the velocity of the contact line during evaporation was controlled by elasticity (Young's modulus). As deposition of particles at the contact line is known to be controlled by the receding velocity of the contact line,[103] the deposition of particles during the constant contact angle evaporation mode was affected by tunable soft PDMS substrates. The particles were more homogeneously distributed on softer substrates due to the higher contact line velocities arising from the combination of smaller receding contact angle and stronger evaporation rate (section 5.4). Using tunable soft PDMS substrates, by changing the base to cross-linker ratio (section 3.4), to control particle deposition required neither modification of the liquid nor of the particles. The ratio between deposit height in the center and at the rim of

the pattern – which is an important characterizing parameter of a coffee stain – decreased with decreasing Young's modulus. Substrate elasticity could thus be tuned to control the evaporation patterns and to reduce coffee-staining. A model (section 5.1) for the contact line velocity that considers capillary forces, viscoelastic dissipation, and contact line friction was developed and reproduced well experimental findings.

The influence of the thermal properties (thermal conductivity and capacity) of the substrate on the evaporation of drops, and the influence of the surface wettability on the liquid load (chapter 6) can be daily appraised when using new energy saving dish-washers: plastic dishes remain wet after the drying cycle, although ceramic dishes or metal cutlery are dry. Drop evaporation experiments were carried out on substrates with different thermal properties, but same wettability (section 6.1). Drops evaporating on highly thermal conductive substrates (silicon) evaporated faster than those evaporating on less thermally conductive substrates (glass). Collaborators developed a numerical model to simulate drop evaporation experimentally and solved the temperature field in the substrates for the entire evaporation process. The numerical model accounted for transient heat conduction in the drop. Numerical calculations agreed very well with experimental data (section 6.2). Furthermore, the liquid load on poly(methyl methacrylate) (PMMA) substrates (representative for the plastic dishes) increased with increasing hydrophobicity. While on hydrophilic surfaces a thin liquid film was formed allowing the liquid to drain from the surface, on hydrophobic surfaces many drops remained attached to the surface. Thus, the residual heat of the dishes was enough to dry the hydrophilic (small residual load of water), but not sufficient to completely dry the hydrophobic (large load of residual water) dishes.

To conclude, the findings presented in this work represent a solid step forward in the fundamental science of drop evaporation. It is now clear that soft substrates are able to directly influence the dynamics of the triple-phase-contact-line (TPCL) influencing both evaporation mode and particle deposition. The softer the substrate was, the faster a drop evaporated and higher TPCL velocities were achieved. With increasing TPCL velocity the thickness of the liquid film (Landau-Levich film) trailing behind the drop rim increased. Particles smaller than this film were more likely to become entrapped within it and subsequently deposited during the CCA evaporation mode. Particles larger than the thickness of the film moved together with the contact line and were accumulated until the contact line was pinned. This influenced the deposit pattern. It is clear now that particle accumulation is a result not only of the flow driven by evaporation, but also of the movement of the TPCL. Thermal conductivity controlled the evaporation rate by affecting the temperature underneath

the drop. Substrates with higher thermal conductivity had higher temperatures underneath the drop because enough heat could be transported to the cooling drop. For substrates with low thermal diffusivity the temperature decreased steadily during the course of evaporation. Consequently, differently than mostly assumed, thermal properties need to be considered for a precise prediction of evaporation rate and time.

7.1 Outlook

The presented work answered different open questions of fundamental interest in the field of drop evaporation. Nonetheless, during this work many other new open issues were recognized, which should be addressed in future work to help understand and control evaporation related processes:

- Increasing the oligomer to cross-linker ratio of PDMS leads to softer substrates. In the extreme case, when no cross-linker is added at all, the substrate is liquid. What are the similarities and differences between the drop evaporation on soft and on liquid substrates? How much of the findings of evaporation on soft substrates can be transferred to the liquid case? These questions are also of major interest for drug delivery, e.g. aerosol delivery into the lung.
- The non-stationary stage during the evaporation can be better investigated for drops smaller than 10 nl. Measurements with a mass resolution of around 0.1 nl would be needed to better investigate the non-stationary stage of evaporation. Such mass resolution can be achieved with the in-house built set-up to measure the bending of an atomic force microscope cantilever caused by a sessile drop.[110] Further development of the set-up is necessary to acquire simultaneously the the mass, the contact radius, and the contact angle of the drop in order to investigate the non-stationary stage of drop evaporation.
- How particle deposition depends on the particle-substrate interaction during the evaporation of suspensions? What is the role of surface tension and contact angle on letting a particle trespass the liquid-air interface at the TPCL? A recent publication by Yunker et al.[111] showed an influence of particle shape on the deposition pattern formed by pinned evaporating drops. Does this influence also exist if the contact line moves during the evaporation?
- A systematic investigation on the evaporation-driven convection in the gas-phase is still lacking. How important is this phenomenon for a single evaporating drop in dependency of evaporation rate, density differences between liquid vapor and surrounding gas, as well as the presence of Marangoni convection? How does the existence of neighboring drops influence the convection in the gas-phase?
- As described in section 2.3.2, liquid mixtures are used to control Marangoni convection inside the drop and influence the coffee-stain effect. But, the Marangoni

convection lasts as long as the mixture has not reached the azeotropic concentration. What is the relation between initial drop volume and concentration of a mixture, in order to maintain the Marangoni-flow throughout the complete evaporation process?

The answers of above mentioned questions will allow to: better deliver drugs by understanding drop evaporation on liquid substrates, understand and control evaporation of nano-sized drops, increase the precision of generative production (3D-printing) by allowing generative printers to deposit particles with a higher precision by better understanding the deposition process, as well by avoiding the coffee-stain effect by using fine-tuned liquid mixtures.

Appendix

Matlab codes used to perform image analysis:

Evaluate_multiple_avi.m

```
%% Evaluate_multiple_avi.m%%
%%% Author:Marcus Camarinha Lopes
%%% Experimental Interface Physiscs - Center of Smart Interfaces

%This programm will transform an avi file (uncompressed) into
%logical sequence of BW pictures
%play them with: implay(BW_image)

%% Choosing Videos & Crop Preparation
[file_nameT,pathNameT]=uigetfile('*.avi',...
    'X:\eip\500_Group Members...\504_Lopes\500_Experiments',...
    'MultiSelect','on');

for n_video=1:length(file_nameT)
%Save names of multiple videos

%Output file name
file_nameT(n_video)

%Choose cropping area
obj = VideoReader([pathNameT file_nameT{n_video}]);
video=read(obj,332); videoGRAY=rgb2gray(video);
videoBW_imp_contrast=imadjust(videoGRAY);
[I2,rect] = imcrop(videoBW_imp_contrast);
rect_multi(n_video)={rect};
end

%% Convertion

for n_video=1:length(file_nameT)
%Output video number
n_video

%Load video
obj = VideoReader([pathNameT file_nameT{n_video}]);

% Define initial and final frame
frame_start=1;
frame_end=obj.NumberOfFrames;

%Create folder for images
rect=rect_multi{n_video};
changeTo=[file_nameT{n_video} 'BMPs'];
mkdir(pathNameT,changeTo);
h = waitbar(0,'Processing video...');


for frame=frame_start:frame_end
waitbar(frame / frame_end)
```

```
%Adjust contrast
videoBW_imp_contrast=imadjust(rgb2gray(imcrop(read(obj,frame),rect)));
%Create binary image
BW = im2bw(videoBW_imp_contrast, 0.14); %  0.25%0.14 - best! %imshow(BW)

% Identify biggest spot (presumed to be the drop)
L = bwlabeln(1-BW, 4); % Label White Spots
S = regionprops(L, 'Area'); % Measure Area of Spots
BW2 = ismember(L, find([S.Area] ==max( [S.Area]) )); % Find Largest Spot

BW2(end,:)=1;
%imshow( BW2 ) % Display Image

%Fill in holes in Droplet
BW3 = imfill( BW2, 'holes' ); % Fill In Holes in Image
changeto2=[pathNameT changeTo];
cd(changeto2);
%Save image
imwrite(~BW3,[num2str(frame) '.bmp'],'bmp')

cd(pathNameT)
end
close(h)
end
```

Calculate_multiple_Geometry.m

```
%% Calculate_multiple_Geometry.m%%
%%% Author:Marcus Camarinha Lopes
%%% Experimental Interface Physiscs - Center of Smart Interfaces

% This programm calculates the height and radius of a Black and white drop
% picture. Afterwards it calculates other geometrical parameters of the
drops
% and save it in a .mat file

%% Choosing Directory and Videos names to be analysed
%UI questions wich directory to be choosen
%[file_name,pathName]=uigetfile('*.avi',...
 %   'X:\eip\500_Group Members\504_Lopes\500_Experiments');
getName=uipickfiles('FilterSpec','*.avi');

%% Preparation for measurements
for n_experiment=1:max(size(getName))
   s = ['[pathstrX, nameX, extX] =... fileparts(getName{'
int2str(n_experiment) '})'];
   eval(s);
   pathstr{n_experiment}=pathstrX;
   name{n_experiment}=nameX;
   ext{n_experiment}=extX;
cd([pathstrX '\' nameX extX 'BMPs']);
%Choose frames to be analysed and set up fps of recorded movie
prompt={'frame_start','frame_end','fps','substrate','liquid',...
    'Resolution - Tube 1X Obj 2X 0.7-6.58436e-3 1#2-3.072983e-3 2#3-
1.866193898e-3 3#4-1.32840348e-3 4#-1.026228695e-3'};
nameW=name{n_experiment};
numlines=1;
```

```
%Automatically definition of initial and final frame
imagefiles = dir('*.bmp');

nfiles = length(imagefiles);    % Number of files found
frame_start=nfiles;
for ii=1:nfiles
   compare = imagefiles(ii).name;
   compare=compare(1:end-4);
   number_compare=str2num(compare);
   if frame_start>number_compare
      frame_start=number_compare;
   end
end

frame_end=frame_start+nfiles-1;
frame_start=int2str(frame_start);
frame_end=int2str(frame_end);

%Prompt specifications, framerate, Surface, Liquid and Pixel resolution
defaultanswer={frame_start,frame_end,'0.5','PDMS 50to1',...
    'pure Water','3.072983e-3'}; %2umSilica0.0125
answerTemp=inputdlg(prompt,nameW,numlines,defaultanswer);

frame_startA(n_experiment)=str2double(answerTemp(1));
frame_endA(n_experiment)=str2double(answerTemp(2));
fpsW(n_experiment)=str2double(answerTemp(3));
substrateW(n_experiment)=answerTemp(4);
liquidW(n_experiment)=answerTemp(5);
resolutionW(n_experiment)=str2double(answerTemp(6));

%%Find tilt

%Load image
pic=imread([num2str(frame_endA(n_experiment)-3) '.bmp']);%frame_end-5

%Crop
disp('Now Crop')
[I2 rectTemp] = imcrop(imread([num2str(frame_startA(n_experiment))
'.bmp']));
rect{n_experiment}=rectTemp;

BW=imcrop(pic,rectTemp); figure(1), imshow(BW)

%Finding Contact Points of triple phase contact line
[x_coordinates y_coordinates Pixel_vals] = impixel;

%Rotation of the picture
disp('Now Edges')
rot_line = polyfit(x_coordinates ,y_coordinates ,1 );
                        % Replicate Substrate 1st order fit
 rot_point = round( polyval( rot_line, length(BW) )); % Truncation Point
 rot_angleTemp = atan( rot_line(1) ); % Correction Angle
 rot_angle(n_experiment)=rot_angleTemp;
 BW4 = imrotate( ~BW, rot_angle(n_experiment)*180/pi,'crop' );
 BW4=~BW4;
 imshow(BW4)

%Finding bottom of drop
```

```
disp('Now Ground height')
[x_coordinates2 y_coordinates2 Pixel_vals2] = impixel;
 BW4 = BW4( 1:y_coordinates2,: ); % Truncation
 LBW4(n_experiment)=length(BW4);
 y_coordinates2w(n_experiment)=y_coordinates2;
end
%% Measurement
for n_experiment=1:max(size(getName))

cd([pathstr{n_experiment} '\' name{n_experiment} ext{n_experiment}
'BMPs']);

%Initializing height and radius vectors
height=zeros(frame_endA(n_experiment)-frame_startA(n_experiment)+1,1);
CR_side=zeros(frame_endA(n_experiment)-frame_startA(n_experiment)+1,1);
CR_circle_fit=zeros(frame_endA(n_experiment)-
frame_startA(n_experiment)+1,1);
r_krumung_circle_fit=zeros(frame_endA(n_experiment)-
frame_startA(n_experiment)+1,1);

%% Extract height and radius (side)
cc=jet(frame_endA(n_experiment)+1-frame_startA(n_experiment)+1);
profile=zeros(frame_endA(n_experiment)-
frame_startA(n_experiment)+1,LBW4(n_experiment));

h = waitbar(0,'Measuring...');

for frame=1:frame_endA(n_experiment)+1-frame_startA(n_experiment)
%framestart:frame_end+1-frame_start

    waitbar(frame/(frame_endA(n_experiment)+1-frame_startA(n_experiment)))

    BW_side=imcrop(imread([num2str(frame_startA(n_experiment)-1+frame)
'.bmp']),rect{n_experiment});
    BW4=imrotate( ~BW_side, rot_angle(n_experiment)*180/pi,'crop' );
    BW4 = ~BW4(1:y_coordinates2w(n_experiment),:);

profile(frame,:)=sum(~BW4);
nonzero=find(profile(frame,:));
height(frame)=max(profile(frame,:))*resolutionW(n_experiment);

if ~isempty(nonzero)
    profile2fit=[0 profile(frame,nonzero(1):nonzero(end)) 0];

    coordinateX=(1:1:length(profile2fit));

    abc = [coordinateX' profile2fit' ones(length(coordinateX),1)]...
        \ -(coordinateX'.^2+profile2fit'.^2);
    a_fit = abc(1); b_fit = abc(2); c_fit = abc(3);

% CIRCLE FIT - calculate the location of the center and the radius
    xcenter = -a_fit/2;
    ycenter = -b_fit/2;
    r_krumung_circle_fit(frame)  =  sqrt((xcenter^2+ycenter^2)-
c_fit)*resolutionW(n_experiment);

    else
```

```
    r_krumung_circle_fit(frame)=0;

end

CR_circle_fit(frame)= sqrt((r_krumung_circle_fit(frame))^2 ...
-(r_krumung_circle_fit(frame)-height(frame))^2); %mm

% CIRCLE CAP - calculate Contact Radius
CR_side(frame)=sum(~BW4(end,:))*resolutionW(n_experiment)/2; %mm

end
close(h)
%Calculate Contact angle and Volume - Assuming symmetrical drop
CA_side=2*atan(height./CR_side);
CA_cir_fit=2*atan(height./CR_circle_fit);

CA_d_side=CA_side*180/pi; CA_d_cir_fit=CA_cir_fit*180/pi;
Volume_side=pi*height.*(3*CR_side.^2+height.^2)./6;
Volume_cir_fit=pi*height.*(3*CR_circle_fit.^2+height.^2)./6;
timestamp=0:(1/fpsW(n_experiment)):(1/fpsW(n_experiment))*...
    (frame_endA(n_experiment)-frame_startA(n_experiment));
file_name=[name{n_experiment} ext{n_experiment}];
substrate=substrateW(n_experiment);
liquid=liquidW(n_experiment);
resolution=resolutionW(n_experiment);
fps=fpsW(n_experiment);

%% Save data
save_date=date;
save([name{n_experiment} ext{n_experiment} 'auswertung.mat'],...
    'height', 'CR_side','CR_circle_fit',...
    'r_krumung_circle_fit','profile',...
    'CA_side','CA_cir_fit','CA_d_side','CA_d_cir_fit',...
    'Volume_side','Volume_cir_fit','timestamp','fps',...
    'save_date','resolution','file_name','substrate','liquid')

end
```

List of Figures

List of Tables

Bibliography

[1] H.W. Morse, On evaporation from the surface of a solid sphere, Proceedings of the American Academy of Arts and Sciences, 45 (1910) 7.

[2] I. Langmuir, The Evaporation of Small Spheres, Physical Review, 12(5) (1918) 368.

[3] L. Xu, H. Zhu, H.E. Ozkan, W.E. Bagley, C.R. Krause, Droplet evaporation and spread on waxy and hairy leaves associated with type and concentration of adjuvants, Pest Manag Sci, 67(7) (2011) 842-851.

[4] C. Sodtke, P. Stephan, Spray cooling on micro structured surfaces, International Journal of Heat and Mass Transfer, 50(19-20) (2007) 4089-4097.

[5] T.L. Jiang, W.-T. Chiang, Effects of multiple droplet interaction on droplet vaporization in subcritical and supercritical pressure environments, Combust. Flame, 97(1) (1994) 17-34.

[6] C. Liu, M.C. Lopes, S.A. Pihan, D. Fell, M. Sokuler, H.-J. Butt, G.K. Auernhammer, E. Bonaccurso, Water diffusion in polymer nano-films measured with microcantilevers, Sensors and Actuators B: Chemical, 160(1) (2011) 32-38.

[7] J. Park, J. Moon, Control of Colloidal Particle Deposit Patterns within Picoliter Droplets Ejected by Ink-Jet Printing, Langmuir, 22(8) (2006) 3506-3513.

[8] R.G. Picknett, R. Bexon, EVAPORATION OF SESSILE OR PENDANT DROPS IN STILL AIR, J. Colloid Interface Sci., 61(2) (1977) 336-350.

[9] R.D. Deegan, O. Bakajin, T.F. Dupont, G. Huber, S.R. Nagel, T.A. Witten, Capillary flow as the cause of ring stains from dried liquid drops, Nature, 389(6653) (1997) 827-829.

[10] H.-J. Butt, D.S. Golovko, E. Bonaccurso, On the derivation of Young's equation for sessile drops: Nonequilibrium effects due to evaporation, J. Phys. Chem. B, 111(19) (2007) 5277-5283.

[11] G.F. Li, H.J. Butt, K. Graf, Microstructures by solvent drop evaporation on polymer surfaces: Dependence on molar mass, Langmuir, 22(26) (2006) 11395-11399.

[12] H. Hu, R.G. Larson, Marangoni effect reverses coffee-ring depositions, J. Phys. Chem. B, 110(14) (2006) 7090-7094.

[13] H. Hu, R.G. Larson, Evaporation of a sessile droplet on a substrate, J. Phys. Chem. B, 106(6) (2002) 1334-1344.

[14] J. Eggers, L.M. Pismen, Nonlocal description of evaporating drops, Physics of Fluids, 22(11) (2010) 112101.

[15] C. Liu, E. Bonaccurso, H.-J. Butt, Evaporation of sessile water/ethanol drops in a controlled environment, PCCP, 10(47) (2008) 7150-7157.

[16] K. Sefiane, L. Tadrist, M. Douglas, Experimental study of evaporating water-ethanol mixture sessile drop: influence of concentration, Int. J. Heat Mass Transfer, 46(23) (2003) 4527-4534.

[17] H.Y. Erbil, G. McHale, M.I. Newton, Drop evaporation on solid surfaces: Constant contact angle mode, Langmuir, 18(7) (2002) 2636-2641.

[18] G. McHale, S. Aqil, N.J. Shirtcliffe, M.I. Newton, H.Y. Erbil, Analysis of droplet evaporation on a superhydrophobic surface, Langmuir, 21(24) (2005) 11053-11060.

[19] C. Sodtke, V.S. Ajaev, P. Stephan, Dynamics of volatile liquid droplets on heated surfaces: theory versus experiment, J. Fluid Mech., 610 (2008) 343-362.

[20] D.S. Golovko, P. Bonanno, S. Lorenzoni, F. Stefani, R. Raiteri, E. Bonaccurso, Evaporative cooling of sessile water microdrops measured with atomic force microscope cantilevers, Journal of Micromechanics and Microengineering, 18(9) (2008).

[21] T. Still, P.J. Yunker, A.G. Yodh, Surfactant-Induced Marangoni Eddies Alter the Coffee-Rings of Evaporating Colloidal Drops, Langmuir, 28(11) (2012) 4984-4988.

[22] B. Derby, Inkjet Printing of Functional and Structural Materials: Fluid Property Requirements, Feature Stability, and Resolution, Annual Review of Materials Research, 40 (2010) 395-414.

[23] P.L. Kelly-Zion, J. Batra, C.J. Pursell, Correlation for the convective and diffusive evaporation of a sessile drop, Int. J. Heat Mass Transfer, 64(0) (2013) 278-285.

[24] R. Pericet-Camara, A. Best, H.-J. Butt, E. Bonaccurso, Effect of capillary pressure and surface tension on the deformation of elastic surfaces by sessile liquid microdrops: An experimental investigation, Langmuir, 24(19) (2008) 10565-10568.

[25] R. Pericet-Camara, G.K. Auernhammer, K. Koynov, S. Lorenzoni, R. Raiteri, E. Bonaccurso, Solid-supported thin elastomer films deformed by microdrops, Soft Matter, 5(19) (2009) 3611-3617.

[26] S.B. Fuller, E.J. Wilhelm, J.M. Jacobson, Ink-jet printed nanoparticle microelectromechanical systems, Journal of Microelectromechanical Systems, 11(1) (2002) 54-60.

[27] V. Mironov, T. Boland, T. Trusk, G. Forgacs, R.R. Markwald, Organ printing: computer-aided jet-based 3D tissue engineering, Trends Biotechnol., 21(4) (2003) 157-161.

[28] R. Noguera, M. Lejeune, T. Chartier, 3D fine scale ceramic components formed by ink-jet prototyping process, J. Eur. Ceram. Soc., 25(12) (2005) 2055-2059.

[29] M. Schena, D. Shalon, R.W. Davis, P.O. Brown, QUANTITATIVE MONITORING OF GENE-EXPRESSION PATTERNS WITH A COMPLEMENTARY-DNA MICROARRAY, Science, 270(5235) (1995) 467-470.

[30] V. Dugas, J. Broutin, E. Souteyrand, Droplet evaporation study applied to DNA chip manufacturing, Langmuir, 21(20) (2005) 9130-9136.

[31] C.J. Brinker, Y.F. Lu, A. Sellinger, H.Y. Fan, Evaporation-induced self-assembly: Nanostructures made easy, Adv. Mater., 11(7) (1999) 579-585.

[32] T. Kawase, H. Sirringhaus, R.H. Friend, T. Shimoda, Inkjet printed via-hole interconnections and resistors for all-polymer transistor circuits, Adv. Mater., 13(21) (2001) 1601-1605.

[33] S. Upcraft, R. Fletcher, The rapid prototyping technologies, Assem. Autom., 23(4) (2003) 318-330.

[34] W.D. Ristenpart, P.G. Kim, C. Domingues, J. Wan, H.A. Stone, Influence of substrate conductivity on circulation reversal in evaporating drops, Phys. Rev. Lett., 99(23) (2007) 234502.

[35] S. David, K. Sefiane, L. Tadrist, Experimental investigation of the effect of thermal properties of the substrate in the wetting and evaporation of sessile drops, Colloids and Surfaces a-Physicochemical and Engineering Aspects, 298(1-2) (2007) 108-114.

[36] G.J. Dunn, S.K. Wilson, B.R. Duffy, S. David, K. Sefiane, The strong influence of substrate conductivity on droplet evaporation, J. Fluid Mech., 623 (2009) 329-351.

[37] B. Sobac, D. Brutin, Thermal effects of the substrate on water droplet evaporation, Phys Rev E, 86(2) (2012) 021602.

[38] G.J. Dunn, S.K. Wilson, B.R. Duffy, S. David, K. Sefiane, A mathematical model for the evaporation of a thin sessile liquid droplet: Comparison between experiment and theory, Colloids and Surfaces A: Physicochemical and Engineering Aspects, 323(1–3) (2008) 50-55.

[39] A. Marmur, Solid-Surface Characterization by Wetting, Annual Review of Materials Research, 39(1) (2009) 473-489.

[40] T. Young, An Essay on the Cohesion of Fluids, Philosophical Transactions of the Royal Society of London, 95 (1805) 65-87.

[41] L. Chen, G.K. Auernhammer, E. Bonaccurso, Short time wetting dynamics on soft surfaces, Soft Matter, 7(19) (2011) 9084-9089.

[42] P. Papadopoulos, X. Deng, L. Mammen, D.-M. Drotlef, G. Battagliarin, C. Li, K. Müllen, K. Landfester, A. del Campo, H.-J. Butt, D. Vollmer, Wetting on the Microscale: Shape of a Liquid Drop on a Microstructured Surface at Different Length Scales, Langmuir, 28(22) (2012) 8392-8398.

[43] F. Taherian, V. Marcon, N.F.A. van der Vegt, F. Leroy, What Is the Contact Angle of Water on Graphene?, Langmuir, 29(5) (2013) 1457-1465.

[44] P.G. de Gennes, Wetting: statics and dynamics, Reviews of Modern Physics, 57(3) (1985) 827-863.

[45] P.-G.d. Gennes, F. Brochard-Wyart, D. Quéré, Capillarity and Wetting Phenomena, Springer, New York, 2004.

[46] A.-M. Cazabat, G. Guena, Evaporation of macroscopic sessile droplets, Soft Matter, 6(12) (2010) 2591-2612.

[47] H.Y. Erbil, Evaporation of pure liquid sessile and spherical suspended drops: A review, Adv. Colloid Interface Sci., 170(1–2) (2012) 67-86.

[48] K. Sefiane, S.K. Wilson, S. David, G.J. Dunn, B.R. Duffy, On the effect of the atmosphere on the evaporation of sessile droplets of water, Physics of Fluids, 21(6) (2009) -.

[49] M.C. Lopes, E. Bonaccurso, Evaporation control of sessile water drops by soft viscoelastic surfaces, Soft Matter, 8 (2012) 3875-3881.

[50] K. Sefiane, R. Bennacer, An expression for droplet evaporation incorporating thermal effects, J. Fluid Mech., 667 (2011) 260-271.

[51] F. Schonfeld, K. Graf, S. Hardt, H.J. Butt, Evaporation dynamics of sessile liquid drops in still air with constant contact radius, Int. J. Heat Mass Transfer, 51(13-14) (2008) 3696-3699.

[52] S. Semenov, V.M. Starov, M.G. Velarde, R.G. Rubio, Droplets evaporation: Problems and solutions, Eur. Phys. J.-Spec. Top., 197(1) (2011) 265-278.

[53] H. Hu, R.G. Larson, Analysis of the microfluid flow in an evaporating sessile droplet, Langmuir, 21(9) (2005) 3963-3971.

[54] S.H. Davis, THERMOCAPILLARY INSTABILITIES, Annu Rev Fluid Mech, 19 (1987) 403-435.

[55] H. Hu, R.G. Larson, Analysis of the effects of Marangoni stresses on the microflow in an evaporating sessile droplet, Langmuir, 21(9) (2005) 3972-3980.

[56] X. Xu, J. Luo, Marangoni flow in an evaporating water droplet, Appl. Phys. Lett., 91(12) (2007).

[57] I. Ueno, K. Kochiya, Effect of evaporation and solutocapillary-driven flow upon motion and resultant deposition of suspended particles in volatile droplet on solid substrate, Adv. Space Res., 41(12) (2008) 2089-2093.

[58] G. Minor, P. Oshkai, N. Djilali, Optical distortion correction for liquid droplet visualization using the ray tracing method: further considerations, Meas Sci Technol, 18(11) (2007) L23-L28.

[59] K.H. Kang, S.J. Leel, C.M. Lee, I.S. Kang, Quantitative visualization of flow inside an evaporating droplet using the ray tracing method, Meas Sci Technol, 15(6) (2004) 1104-1112.

[60] R.G. Larson, H. Hu, DRYING A SESSILE DROPLET: IMAGING AND ANALYSIS OF TRANSPORT AND DEPOSITION PATTERNS, in: Evaporative Self-Assembly of Ordered Complex Structures, pp. 1-57.

[61] M.C. Pirrung, How to make a DNA chip, Angewandte Chemie (International ed. in English), 41(8) (2002) 1276-1289.

[62] Á.G. Marín, H. Gelderblom, D. Lohse, J.H. Snoeijer, Order-to-Disorder Transition in Ring-Shaped Colloidal Stains, Phys. Rev. Lett., 107(8) (2011) 085502.

[63] L. Pauchard, F. Parisse, C. Allain, Influence of salt content on crack patterns formed through colloidal suspension desiccation, Phys Rev E, 59(3) (1999) 3737-3740.

[64] D. Soltman, V. Subramanian, Inkjet-printed line morphologies and temperature control of the coffee ring effect, Langmuir, 24(5) (2008) 2224-2231.

[65] H.B. Eral, D.M. Augustine, M.H.G. Duits, F. Mugele, Suppressing the coffee stain effect: how to control colloidal self-assembly in evaporating drops using electrowetting, Soft Matter, 7(10) (2011) 4954-4958.

[66] P.J. Yunker, T. Still, M.A. Lohr, A.G. Yodh, Suppression of the coffee-ring effect by shape-dependent capillary interactions, Nature, 476(7360) (2011) 308-311.

[67] M. Majumder, C.S. Rendall, J.A. Eukel, J.Y.L. Wang, N. Behabtu, C.L. Pint, T.-Y. Liu, A.W. Orbaek, F. Mirri, J. Nam, A.R. Barron, R.H. Hauge, H.K. Schmidt, M. Pasquali, Overcoming the "Coffee-Stain" Effect by Compositional Marangoni-Flow-Assisted Drop-Drying, The Journal of Physical Chemistry B, 116(22) (2012) 6536-6542.

[68] V.L. Morales, J.-Y. Parlange, M. Wu, F.J. Pérez-Reche, W. Zhang, W. Sang, T.S. Steenhuis, Surfactant-Mediated Control of Colloid Pattern Assembly and Attachment Strength in Evaporating Droplets, Langmuir, 29 (2013) 1831-1840.

[69] A.I. Rusanov, Theory of the wetting of elastically deformed bodies. I. Deformation with a finite contact angle, Colloid Journal of the USSR, 37(4) (1975).

[70] A.I. Rusanov, Theory of the wetting of elastically deformed bodies. II. Equilibrium conditions and work of deformation with a finite contact angle, Colloid Journal of the USSR, 37(4) (1975).

[71] J. Bico, B. Roman, L. Moulin, A. Boudaoud, Adhesion: Elastocapillary coalescence in wet hair, Nature, 432(7018) (2004) 690-690.

[72] T. Haschke, E. Bonaccurso, H.-J. Butt, D. Lautenschlager, F. Schoenfeld, W. Wiechert, Sessile-drop-induced bending of atomic force microscope cantilevers: a model system for monitoring microdrop evaporation, Journal of Micromechanics and Microengineering, 16(11) (2006) 2273-2280.

[73] A. Sell, Einfluss der Benetzungs- sowie thermischen Eigenschaften des Substrates auf die Verdunstung von Tropfen, Technische Universität Darmstadt, 2013.

[74] M. Sokuler, G.n.K. Auernhammer, M. Roth, C. Liu, E. Bonacurrso, H.-J.r. Butt, The Softer the Better: Fast Condensation on Soft Surfaces, Langmuir, 26(3) (2009) 1544-1547.

[75] D. Chauvel-Lebret, P. Auroy, M. Bonnaure-Mallet, Biocompatibility of Elastomers, in: Polymeric Biomaterials, Revised and Expanded, CRC Press, 2001.

[76] J. Nase, Debonding of viscoelastic materials : from a viscous liquid to a soft elastic solid, PhD, Universität des Saarlandes, Saarbrücken/Paris, 2009.

[77] DIN 1249-10:1990-08. Glass for use in building construction; chemical and physical properties, in, Beuth Verlag GmbH, 1990.

[78] H.R. Shanks, P.D. Maycock, P.H. Sidles, G.C. Danielson, Thermal Conductivity of Silicon from 300 to 1400°K, Physical Review, 130(5) (1963) 1743-1748.

[79] E. Yamasue, M. Susa, H. Fukuyama, K. Nagata, Thermal conductivities of silicon and germanium in solid and liquid states measured by non-stationary hot wire method with silica coated probe, J. Cryst. Growth, 234(1) (2002) 121-131.

[80] H.-J. Jordan, R. Brodmann, Highly accurate surface measurements by means of white light confocal microscopy, in: X. International Colloquium on Surfaces, Chemnitz, Germany, 2000.

[81] W. Becker, D. Gross, Mechanik elastischer Körper und Strukturen, Springer-Verlag, Berlin, 2002.

[82] E. Clapeyron, Mémoire sur la puissance motrice de la chaleur, J. École polytechnique 14 (1834) 153-190. R Clausius, Über die bewegende Kraft der Wärme und die Gesetze, die sich daraus für die Wärmelehre selbst ableiten lassen, Poggend. Ann. Phys. Chem., 1850.

[83] R.E. McDonald, R.I. Fleming, J.G. Beeley, D.L. Bovell, J.R. Lu, X. Zhao, A. Cooper, M.W. Kennedy, Latherin: A Surfactant Protein of Horse Sweat and Saliva, PLoS ONE, 4(5) (2009) e5726.

[84] E.R. Jerison, Y. Xu, L.A. Wilen, E.R. Dufresne, Deformation of an Elastic Substrate by a Three-Phase Contact Line, Phys. Rev. Lett., 106(18) (2011) 186103.

[85] C.W. Extrand, Y. Kumagai, Contact angles and hysteresis on soft surfaces, J. Colloid Interface Sci., 184(1) (1996) 191-200.

[86] M.E.R. Shanahan, THE INFLUENCE OF SOLID MICRO-DEFORMATION ON CONTACT-ANGLE EQUILIBRIUM, Journal of Physics D-Applied Physics, 20(7) (1987) 945-950.

[87] M.E.R. Shanahan, THE SPREADING DYNAMICS OF A LIQUID-DROP ON A VISCOELASTIC SOLID, J. Phys. D: Appl. Phys., 21(6) (1988) 981-985.

[88] M.E.R. Shanahan, A. Carre, VISCOELASTIC DISSIPATION IN WETTING AND ADHESION PHENOMENA, Langmuir, 11(4) (1995) 1396-1402.

[89] A. Carre, J.C. Gastel, M.E.R. Shanahan, Viscoelastic effects in the spreading of liquids, Nature, 379(6564) (1996) 432-434.

[90] R. Pericet-Camara, E. Bonaccurso, K. Graf, Microstructuring of polystyrene surfaces with nonsolvent sessile droplets, Chemphyschem, 9(12) (2008) 1738-1746.

[91] R.W. Style, R. Boltyanskiy, Y. Che, J.S. Wettlaufer, L.A. Wilen, E.R. Dufresne, Universal Deformation of Soft Substrates Near a Contact Line and the Direct Measurement of Solid Surface Stresses, Phys. Rev. Lett., 110(6) (2013) 066103.

[92] D.S. Golovko, H.-J.r. Butt, E. Bonaccurso, Transition in the Evaporation Kinetics of Water Microdrops on Hydrophilic Surfaces, Langmuir, 25(1) (2008) 75-78.

[93] G. Li, S. Moreno Flores, C. Vavilala, M. Schmittel, K. Graf, Evaporation Dynamics of Microdroplets on Self-Assembled Monolayers of Dialkyl Disulfides, Langmuir, 25(23) (2009) 13438-13447.

[94] G. Pu, S.J. Severtson, Water Evaporation on Highly Viscoelastic Polymer Surfaces, Langmuir, 28(26) (2012) 10007-10014.

[95] R. Pericet-Camara, A. Best, H.J. Butt, E. Bonaccurso, Effect of capillary pressure and surface tension on the deformation of elastic surfaces by sessile liquid microdrops: An experimental investigation, Langmuir, 24(19) (2008) 10565-10568.

[96] A. Carlson, G. Bellani, G. Amberg, Contact line dissipation in short-time dynamic wetting, EPL (Europhysics Letters), 97(4) (2012) 44004.

[97] B.M. Weon, J.H. Je, Self-Pinning by Colloids Confined at a Contact Line, Phys. Rev. Lett., 110(2) (2013) 028303.

[98] T.A.H. Nguyen, M.A. Hampton, A.V. Nguyen, Evaporation of Nanoparticle Droplets on Smooth Hydrophobic Surfaces: The Inner Coffee Ring Deposits, The Journal of Physical Chemistry C, 117(9) (2013) 4707-4716.

[99] R.D. Deegan, O. Bakajin, T.F. Dupont, G. Huber, S.R. Nagel, T.A. Witten, Contact line deposits in an evaporating drop, Physical Review E, 62(1) (2000) 756-765.

[100] E. Widjaja, M.T. Harris, Particle deposition study during sessile drop evaporation, AlChE J., 54(9) (2008) 2250-2260.

[101] T.D. Reynolds, S.K. Kalpathy, S. Kumar, L.F. Francis, Dip coating of charged colloidal suspensions onto substrates with patterned wettability: Coating regime maps, J. Colloid Interface Sci., 352(1) (2010) 202-210.

[102] M. Ghosh, F. Fan, K.J. Stebe, Spontaneous Pattern Formation by Dip Coating of Colloidal Suspensions on Homogeneous Surfaces, Langmuir, 23(4) (2007) 2180-2183.

[103] G. Berteloot, A. Daerr, F. Lequeux, L. Limat, Dip coating with colloids and evaporation, Chemical Engineering and Processing: Process Intensification, 68 69-73.

[104] V.S. Nikolayev, Dynamics of the triple contact line on a nonisothermal heater at partial wetting, Physics of Fluids, 22(8) (2010).

[105] B. Sobac, D. Brutin, Triple-Line Behavior and Wettability Controlled by Nanocoated Substrates: Influence on Sessile Drop Evaporation, Langmuir, 27(24) (2011) 14999-15007.

[106] S. Semenov, V.M. Starov, R.G. Rubio, H. Agogo, M.G. Velarde, Evaporation of sessile water droplets: Universal behaviour in presence of contact angle hysteresis, Colloids and Surfaces a-Physicochemical and Engineering Aspects, 391(1-3) (2011) 135-144.

[107] T. Gambaryan-Roisman, Marangoni-induced deformation of evaporating liquid films on composite substrates, Journal of Engineering Mathematics, 73(1) (2012) 39-52.

[108] M.C. Lopes, E. Bonaccurso, T. Gambaryan-Roisman, P. Stephan, Influence of the substrate thermal properties on sessile droplet evaporation: Effect of transient heat transport, Colloids and Surfaces A: Physicochemical and Engineering Aspects, 432(0) (2013) 64-70.

[109] V.-G. (ed.), VDI Heat Atlas, Springer, Berlin, 2010.

[110] C. Liu, E. Bonaccurso, Microcantilever sensors for monitoring the evaporation of microdrops of pure liquids and mixtures, Rev. Sci. Instrum., 81(1) (2010) 013702-013708.

[111] P.J. Yunker, M.A. Lohr, T. Still, A. Borodin, D.J. Durian, A.G. Yodh, Effects of Particle Shape on Growth Dynamics at Edges of Evaporating Drops of Colloidal Suspensions, Phys. Rev. Lett., 110(3) (2013) 035501.

Acknowledgements

I acknowledge the success of my thesis to a broad group of people including my family, research group, colleagues and friends. Everyone had an important share on my successful journey to accomplish this thesis.

Thank you Elmar Bonaccurso, for your supervising (super-)skills. Your suggestions, comments, and humorous-ironical sentences in our manuscript drafts taught me a lot and motivated me to correct them. I thank all members and former members of the Experimental Interface Physics group (Lars Heim, Longquan Chen, Dmytro Golovko, Marcus Schmelzeisen, Oscar Herrera, Xiang Wang, Andreas Plog, Julien Petit and Tassilo Kaule) for the collaboration and discussion. For the collaborative work I would also like to thank Tatiana Gambaryan-Roisman, Martin Still and Professor Peter Stephan from the institute of Technical Thermodynamics at TU Darmstadt. Thank you, Professor Cameron Tropea, for running the interdisciplinary institute Center of Smart Interfaces (CSI), which allowed me to get into contact with colleagues from different research areas. Thank you, all active postdoc- and PhD-students from the TU Darmstadt, for the very interesting talks and discussions during the CSI-seminars. My journey had neither technical nor administrative problems thanks to: Felix Seipp, Sebastian Keuth, Jana Müller, Monika Medina, Marcus Keiner and Angela Berger. You did a great job!

Thank you, Slawa Kupermann, Martin Gielok, Yu Wang and Angelika Sell for your patience and for teaching/learning so much under my supervision.

For the non-work-related experience during my thesis I have to thank: Marius Bayer, Karl Larry, Goran Arambasic, Matthias Borsdorf, Jakob Katz, Daniel König, Alex Krasni, Vitali Dejkun, Peter Rossa, Eduard Heffel, Alex Schwartz, Florian Böss, Martin Bang, Davide Gatti, Rossella Quaini, Thomas Fasold and Roswitha Hirche-Fasold.

It was an honor for me to meet and work with the people at the Max-Planck-Institute for polymer research, especially with Professor Hans-Jürgen Butt, Günter Auernhammer, Daniela Fell, Emmanouil “Manos” Anyfantakis and Andreas Best. Thanks to Roberto Raiteri and Henry Andrade for giving me the opportunity to experience a collaborative work in the University of Genoa, Italy. Thanks also to Steve Garoff, Ramankur Sharma, Amsul Khanal, Ying Zhang, Amy Stetten and Nora Swisher for hosting me at the Carnegie Mellon University in Pittsburgh for three months. I sincerely thank the German Academic Exchange Service for the financial support during my stay in the USA.

My brother Tiago always helped me with his intelligent words and his tremendous knowledge about myself, therefore I am very thankful. I thank also my parents Teresa and Carlos for everything they sacrificed to give me the education I now have. And finally, I would like to thank my girlfriend, Kathrin, for being such a great partner and friend. With you I shared, and will further share, many good and bad moments of my life.

At last but not least in memory of my deceased Grandfather, Dr. Jochris Manuel Camarinha:

"Você está com dor? Está com sede? Está com fome? Então, pare de chorar!"

Curriculum Vitae

Marcus Camarinha Lopes

Persönliche Daten

Geburtsdatum:	12.12.1985
Geburtsort:	Campinas – SP – Brasilien

Promotion

10/2010– 11/2013	Promotion an der Technischen Universität Darmstadt Center of Smart Interfaces – Experimental Interface Physics
07/2010– 09/2013	Gastwissenschaftler – Carnegie Mellon University – Pittsburgh – USA

Hochschulstudium

03/2010 – 09/2010	Master-Arbeit beim Deutschen Zentrum für Luft- und Raumfahrt (DLR), Stuttgart – Note: Sehr gut Auslegung einer Kühleinheit zur Abtrennung einer definierten Kerosinfraktion zur H_2-Erzeugung
10/2008 – 09/2010	Master of Science (M.Sc.) Maschinenbau - Mechanical and Process-Engineering Technische Universität Darmstadt – Note: Sehr gut
10/2005 – 10/2008	Bachelor of Science (B.Sc.) Maschinenbau - Mechanical and Process-Engineering Technische Universität Darmstadt – Note: Gut

Schulausbildung

10/2004 – 06/2005	Studienkolleg – Academic Bridging Courses, Technische Universität Darmstadt – Note: 1,6
1993 – 2003	Schulbesuch in Campinas, Brasilien Abschluss: Conclusão do Ensino Médio (Abitur)

Betreuung von Studenten

03/2013 – 08/2013	Bachelor-Arbeit von Angelika Sell: *Einfluss der Benetzungs- sowie thermischen Eigenschaften des Substrates auf die Verdunstung von Tropfen*
05/2011 – 08/2011	Bachelor-Arbeit von Slawa Kupermann: *Entwicklung eines Matlab-Berechnungstools für die Analyse von Tropfenverdunstungsmodellen*

Preise und Auszeichnungen:

06/2013	DAAD Stipendium für einen Kurzaufenthalt an der Carnegie Mellon University – Pittsburgh – USA
04/2013	Konferenzstipendium für den „1st International Workshop on Wetting and Evaporation“ – Marseille – Frankreich Auswahl durch European Space Agency (ESA) und Centre national d'études spatiales (CNES - French Space Agency)

Veröffentlichungen in Internationalen Zeitschriften:

Lopes, M. C.; Bonaccurso, E., *Influence of substrate elasticity on deposition patterns from evaporation droplets of water-silica suspensions*. Soft Matter, 2013, 9, 7942-7950.

Lopes M. C.; Bonaccurso E.; Gambaryan-Roismana T.; Stephan P., *Influence of the substrate thermal properties on sessile droplet evaporation: Effect of transient heat transport*. Colloid Surface A, 2013, 432, 64-70.

Lopes, M. C.; Bonaccurso, E., *Evaporation control of sessile water drops by soft viscoelastic surfaces*. Soft Matter, 2012, 8, 7875-7881.

Liu, C.; Lopes, M. C.; Pihan, S. A.; Fell, D.; Soluker, M.; Butt, H.-J.; Auernhammer, G. K.; Bonaccurso, E.; *Water diffusion in polymer nano-films measured with microcantilevers*. Sensors and Actuators B: Chemical, 2011, 160, (1), 32-38.

Vorträge bei internationalen Konferenzen:

The evaporation of sessile drops on soft surfaces: controlling the evaporation mode.
1st Int. Workshop on Wetting and evaporation: droplets of pure and complex fluids, Marseilles, France, 2013.

Controlling the evaporation of sessile drops by surface softness.
Smart and Green Interfaces 2013, Prague, Czech Republic, 2013.

Evaporation control of sessile water drops by soft viscoelastic surfaces.
9 th Zsigmondy-Colloquium Evonik Industries AG, Essen, Germany, 2013.

Posters bei internationalen Konferenzen:

Evaporation control of sessile water drops by soft viscoelastic surfaces.
Soft Matter Days, Bad Honnef, Germany, 2012.

Influence of the elasticity on sessile droplet evaporation.
8th Zsigmondy-Colloquium, Darmstadt, Germany, 2012.

Influence of the elasticity and thermal conductivity on drop evaporation.
18th Ostwald Colloquium Evonik Industries AG, Mainz, Germany, 2011.